Material Properties of Actin Filament Bundles

by

Alec P. Robertson

Submitted to the Department of Mechanical Engineering
in partial fulfillment of the requirements for the degree of

Doctor of Philosophy in Mechanical Engineering

at the

MASSACHUSETTS INSTITUTE OF TECHNOLOGY

February 2009

Author ....
Department of Mechanical Engineering
January 29th, 2009

Certified by..
Paul Matsudaira
Professor of Biology
Thesis Supervisor

Accepted by..
David Hardt
Chairman, Department Committee on Graduate Students

Material Properties of Actin Filament Bundles

by

Alec P. Robertson

Submitted to the Department of Mechanical Engineering
on January 29th, 2009, in partial fulfillment of the
requirements for the degree of
Doctor of Philosophy in Mechanical Engineering

Abstract

Actin is an ubiquitous structural protein fundamental to such biological processes as cell motility and muscle contraction. Our model system is the acrosomal process of the *Limulus* sperm which extends a 60 μm long actin bundle during reproduction. It is an example of a biological spring where the force of elongation derives from twist energy stored within the bundle during spermatogenesis. In addition to actin the acrosome comprises only one other protein: scruin, an actin-binding protein specific to *Limulus* that decorates and crosslinks actin filaments into a crystalline bundle. Our goal is to reconstitute the structure of the acrosome using these two proteins in order to further elucidate the role of scruin in actin bundle crosslinking.

A multi-scale approach is presented wherein the bending rigidity of scruin bundles and their constituent filaments are probed individually, then inter-related by simple mechanical models. Material properties of filaments and bundles are measured using a combination of optical tweezers, electron and fluorescence microscopy. We find that scruin bundles reconstituted from acrosome fragments display an ordered structure, with a bending rigidity orders of magnitude higher than their individual filaments. Actin bundles formed by depletion exhibit similar behavior, revealing an intrinsic regime of coupled actin bundle formation. Bundle elastic moduli are eight orders of magnitude stiffer than reconstituted networks and an order of magnitude softer than the native acrosome, highlighting scruin's ability to dictate a wide range of material properties depending on the formation conditions.

Thesis Supervisor: Paul Matsudaira
Title: Professor of Biology

Acknowledgments

It not possible to undertake a PhD without the help and support of a great many people. I extend my sincerest thanks to the following people who have made valuable contributions during the course of my studies.

My committee: Prof. Angela Belcher, Prof. Roger Kamm, Prof. Matt Lang and Prof. Paul Matsudaira for their guidance throughout the project.

The Matsudaira lab: Valeriya Baru and Yelena Freyzon for their help with all things biochemical; Danielle France Cook, Michael Murrell and Mariya Barch for their friendship; Bob Burger for handling the finances; and Al Davis for our computing facilities.

The Lang lab: Carlos Castro and Dave Appleyard were instrumental in setting up the optical trap experiments; Hyungsuk Lee and Jorge Ferrer helped me with actin; and Yongdae Shin showed me the PEG coverslip protocol.

Dr Paul Wiggins for many lengthy discussions about mechanics, and Prof. Zvonimir Dogic and Ed Barry for teaching me the actin persistence length protocols.

Dr Kazuyoshi Murata who mentored me in the use of our cryo-electron microscope, and Anna Bershteyn and Steve Dolan without whom it would not have been possible to use the scope in later days.

Leslie Regan from Mechanical Engineering for her help and guidance.

My friends and family, for keeping me sane along the way.

Contents

List of Figures

List of Tables

Chapter 1

Introduction

Biological springs and motors are mechanical systems that drive biological processes such as muscle contraction and cell motility. Biological motors are typically powered by the hydrolysis of ATP, a common energy source synthesized through respiration or photosynthesis. Our model system is the *Limulus* acrosomal process, which projects a 60 µm long crystalline rod during reproduction (see Figure 1-1). It is an example of a biological spring, where the force of elongation derives from a change in conformation of an actin spring stored in the base of the sperm cell. In its purified state the acrosome comprises only two proteins: actin, commonly found in muscle fibers; and scruin, an actin binding protein found only in *Limulus* sperm. Scruin decorates the outside of actin filaments and induces a small over-twist per actin subunit. Scruin-scruin interactions cross-link neighboring filaments into an hexagonally packed crystalline bundle, which is further twisted into a micrometer-scale coil in the base of the sperm cell. This research aims to study the role of scruin in actin bundle formation through reconstitution of the various conformations of the acrosome.

1.1 The *Limulus* Acrosomal Process

Seminal work on the *Limulus* acrosomal process is attributed to Andre, Tilney and DeRosier who elucidated much of its formation and structure, and characterized its three conformations: the coil, the true discharge (TD) and the false discharge (FD) [5, 110, 111]. They showed that during spermatogenesis the acrosome initiates at a seeding region in the anterior of the cell and forms a crystalline bundle of actin filaments, decorated and crosslinked by the scruin actin-binding protein (see Supplemental Figure A-3). The preferred end of the actin filaments is associated with a cell membrane and the bundle grows down through the nuclear channel to the base of the cell where it is bent and packed into the coil: a right-handed helix comprising 700 nm long straight arms each twisted by 60° and separated by kinked elbows [32]. The kinked packing mechanism represents an elegant tradeoff between bending and twisting energy, required to pack a 60 µm long rod into a 3 µm diameter coil [27].

In the presence of an egg (or free Ca^{2+}, but independent of ATP) the coil untwists into the true discharge: a long straight crystalline rod that penetrates the egg coating during fertilization [15, 16, 31, 33]. The TD is straight and tapered along its length, from around 85 filaments at the base to 15 at the tip, the elbows having been "melted" out during the untwisting [112]. Recent studies have shown that although Ca^{2+} is required for initiation of this reaction, the force of elongation derives from stored elastic energy in the coil [96, 98]. As such, the acrosomal reaction is characteristic of a biological spring rather than more common ATP driven (biological motor) reactions such as actin-myosin driven muscle contraction [18, 73].

When subject to external osmotic pressure the coil transforms into a third conformation: the false discharge, a long left-handed helix ejected from the cell's posterior. The original kinked-helix arrangement remains but each arm of the left-handed FD is now twisted by -30°, representing a change in twist of -90° compared to the coil. While the coil-TD transformation is irreversible, the FD retracts upon relief of the external osmotic pressure. Additionally it is possible to induce the TD reaction while the FD is extended, implying a continuum between the three conformations (FD $\leftrightarrow$ coil $\rightarrow$ TD) [105].

Isolated and demembranated TD and FD are readily purified and imaged under electron microscopy where they display a highly ordered crystalline structure (Figure 1-2). The TD is hexagonally packed and straight along its length which appears as a banded pattern when the electron beam is aligned with the bundle lattice axis. The FD is also hexagonally packed but its twist creates a processive banding pattern along the bundle, making it readily distinguishable from the true discharge.

1.2 Actin Monomers and Filaments

Actin is an ubiquitous and highly conserved structural protein. There are three mammalian isoforms: α-actin, which predominates in muscle cells; and β- and γ-actin, both found in non-muscle cells. (α-actin will be referred to as actin from here on.) Human skeletal muscle actin is identical in sequence to many other muscle actins including rabbit, chicken and cow [54]. All share the same 375 amino acid sequence and a molecular weight of 42 kD. The structure of monomeric rabbit skeletal

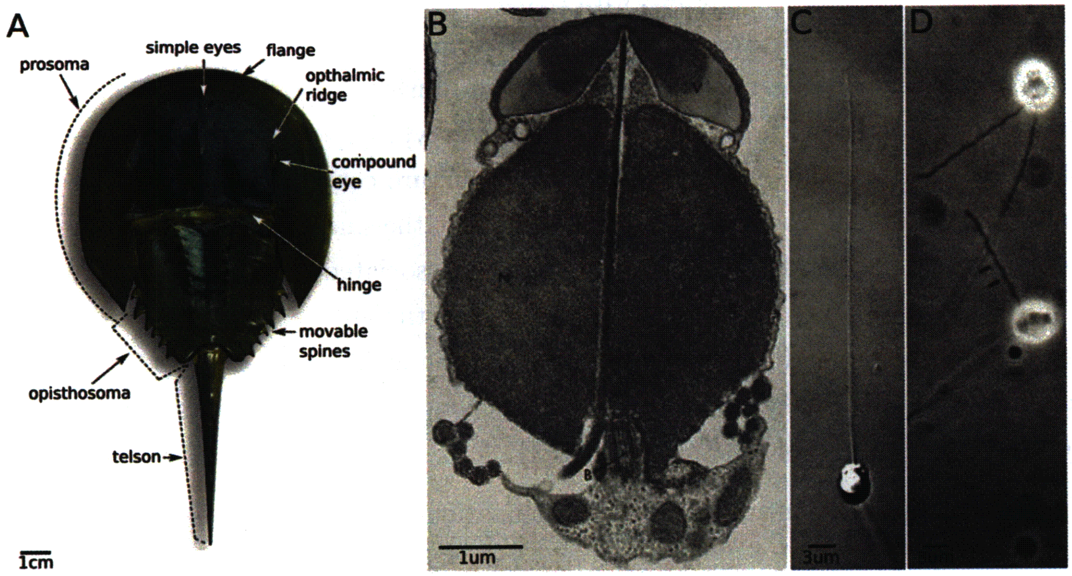

Figure 1-1: *Limulus* model system. Top view of *Limulus Polyphemus* (A) and its sperm cell (B). Here the anterior seeding region and straight nascent acrosome in the nuclear channel are clearly visible, so too is the coil shown in cross section at the base of the cell. The true (C) and false (D) discharge reactions are readily imaged under phase microscopy. The other bundle exiting the sperm posterior is the flagella. Images reproduced from Tilney [110], Shin [95] and the University of Delaware [1].

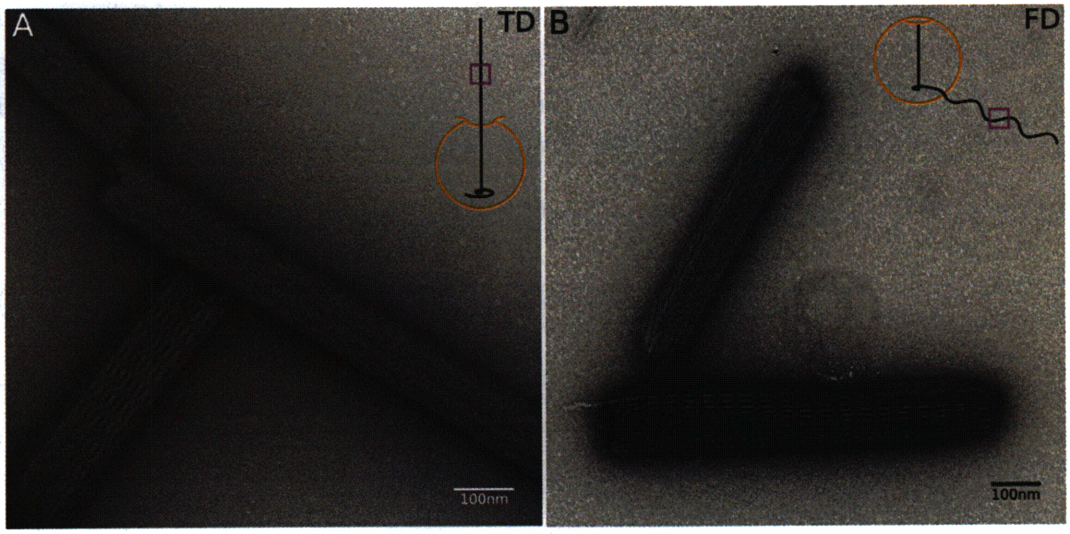

Figure 1-2: True and false discharge. Electron microscopy of isolated, demembranated and sonicated true discharge fragments (left). The characteristic banded pattern occurs when the hexagonally packed bundle is aligned with the electron beam. Purified false discharges (right) show a similar but processive banded pattern which arises from its twisted hexagonal structure.

muscle actin (g-actin) in a complex with DNase-I was originally determined by Kabsch (PDB id: 1ATN, see Figure 1-3) [55]. The complex was required to prevent actin polymerizing into its filamentous (f-actin) form during crystallization. The crystal unit cell size was 5.5×5.5×3.5 nm, though actin is typically approximated as a sphere of hydrodynamic radius 2.8 nm. The 1ATN structure comprises two domains, large and small, each with two subdomains: 1-2 reside in the small domain, 3-4 in the large domain. The nucleotide (ATP or ADP) and an associated divalent cation (Ca^{2+} or Mg^{2+}) bind the cleft between the two domains. In the absence of a nucleotide, actin rapidly denatures [30, 60]. *Limulus* acrosomal actin is 92% similar to 1ATN and due to the comparative ease of purification it is common to use rabbit skeletal muscle actin in its place for reconstitution assays [119].

Actin is typically purified using a polymerization-depolymerization cycle originally described by Spudich *et al* [99]. In this protocol, actin remains in its monomeric form in the presence of Ca^{2+} and can be stored at 4 °C for up to one week. Addition of Mg^{2+} displaces Ca^{2+} from the bound ATP promoting nucleation and the formation of unstable oligomers. Both Mg^{2+} and increased ionic strength are required to initiate polymerization into f-actin filaments (typically 20-100 mM KCl and 2 mM $MgCl_2$ are used). There is an initial lag phase involving rapid cation exchange from Ca^{2+} to Mg^{2+} for each monomer, followed by the formation of unstable oligomers of 3-5 monomers in length [109, 113, 117]. Some oligomers remain stable long enough to initiate rapid polymerization into f-actin, with g-actin recruited to both ends of the filament. The ATP nucleotide is hydrolyzed into ADP in the filament core while the outer bound monomers remain ATP-bound (actin filaments in the TD are ADP-bound) [19, 61, 96].

The rate of polymerization can be described by the differential equation

$$\frac{dn}{dt} = k_{\text{on}} c_a - k_{\text{off}}, \tag{1.1}$$

where c_a is the concentration of g-actin in solution (μM), k_{on} is the association constant ($\frac{1}{\mu\text{Ms}}$), k_{off} is the dissociation constant ($\frac{1}{\text{s}}$), n is the number of monomers added, and t is time (s). Because monomers bind to both the barbed (preferred) and pointed (non-preferred) ends, the growth of each end can be described by the same differential equation but with different rate constants (see Table 1.1) [43, 44, 64, 82–84]. Measurements of kinetic rate constants as a function of solution viscosity showed the kinetics to be diffusion limited [37]. Elongation rates were found to be comparable for Mg^{2+}- and Ca^{2+}-bound f-actin, though Mg^{2+}-actin showed a shorter lag period prior to the onset of polymerization (consistent with its role in promoting nucleation)

Table 1.1: Actin kinetic rate constants from Pollard [83].

nucleotide	rate constant	units	barbed end	pointed end
ATP	k_{on}	$\frac{1}{\mu\text{Ms}}$	11.6	1.4
	k_{off}	$\frac{1}{s}$	1.3	0.8
ADP	k_{on}	$\frac{1}{\mu\text{Ms}}$	3.8	0.2
	k_{off}	$\frac{1}{s}$	7.2	0.3

[20–22].

Based on the 1ATN structure and published concurrently, the structure of f-actin was first published by Holmes (Figure 1-4) [50]. His model described a right-handed double helix of actin monomers with a rise of 2.75 nm, a rotational offset of -166.15°, and a cross-sectional area of 25 nm^4. The unit cell was 35.75 nm long and comprised 26 monomers (13 per helix). Since then it has been refined slightly and the structure of two adjoining monomers also determined [63, 123].

As polymerization approaches steady state, the free monomer concentration approaches the critical concentration ($c_c = \text{k}_{\text{on}}/\text{k}_{\text{off}}$) and an equilibrium is reached between the bulk and the filaments. Monomers disassociating from the filament ends return to the bulk which increases the free monomer concentration and promotes repolymerization. The difference in critical concentration between the barbed (112 nM) and pointed (571 nM) ends can lead to treadmilling, wherein monomers depolymerize from the pointed end and re-attach to the barbed end, propelling the filament forward. Depolymerization can be prevented by adding phalloidin (6 Å in diameter, 1320 Da for the Alexa-488 conjugated molecule, Invitrogen), a small toxin that binds at the intersection of three adjacent monomers in a 1:1 stoichiometry with actin [29, 76]. Phalloidin does not affect the polymerization rate but prevents monomers from disassociating from either end of the filament [40].

1.3 Actin Bundles and Networks

The formation of actin bundles and networks is critical to many biological processes such as: cell motility, where branched networks of actin filaments crosslinked by actin-binding proteins extend the lamellipodium; muscle movement, where myosin ratchets along actin filaments causing contraction and expansion; and the acrosome, where the scruin actin-binding protein tightly crosslinks actin filaments into a crystalline bundle.

1.3.1 Actin Binding Proteins

Actin binding proteins can be organized into several families based on their homology [8, 36, 68]. One family, characterized by a tandem pair of actin binding domains, includes fimbrin, α-actinin and filamin. Fimbrin and α-actinin crosslink actin into bundles while filamin forms actin networks. Fascin, which forms crosslinked networks in filopodia, constitutes a second family. Although not homologous to any of these proteins, scruin has most in common with the former due to its tandem pair of actin binding domains [90].

Fimbrin, α-actinin and fascin

The structure of fimbrin-actin bundles was studied by electron microscopy of human T-fimbrin crosslinked β-actin filaments grown on lipid layers [118]. Actin was polymerized at 500 nM in the presence of 2 two-fold excess of fimbrin to form regular two dimensional ribbons. A fimbrin crossbridge formed every 37.5 nm (slightly longer than the Holmes f-actin unit cell length) and the interfilament spacing was 12 nm. For fimbrin-free actin filaments on the same lipid layers, the interfilament spacing was 8 nm. For α-actinin crosslinked filaments under comparable conditions, the interfilament spacing increased to 39 nm [107]. X-ray scattering of α-actinin bundles formed in free solution revealed a slightly tighter packing of 33 nm, consistent with the length of the α-actinin dimer [81].

Fascin bundles, reconstituted by adding egg extract to f-actin filaments were highly ordered and hexagonally packed at low fascin-actin ratios [100]. Packing order increased over time but decreased at higher ratios, with no bundles forming at very low fascin concentrations. In contrast, when purified fascin was co-polymerized with g-actin, improved structure was observed at high fascin concentrations [49]. Additionally, the diameter of the fascin actin bundles was found to be regulated by the fascin to actin ratio [26].

These experiments highlight the ability of various actin-binding proteins to regulate the size and spacing of actin filament bundles, depending on the relative concentrations of actin and actin-binding protein.

Scruin

In contrast to ubiquitous actin, scruin specific to *Limulus* sperm and has no homology to any known actin binding protein. Two isoforms have been isolated: α-scruin which decorates and crosslinks actin in the acrosome; and β-scruin which is 67% similar to

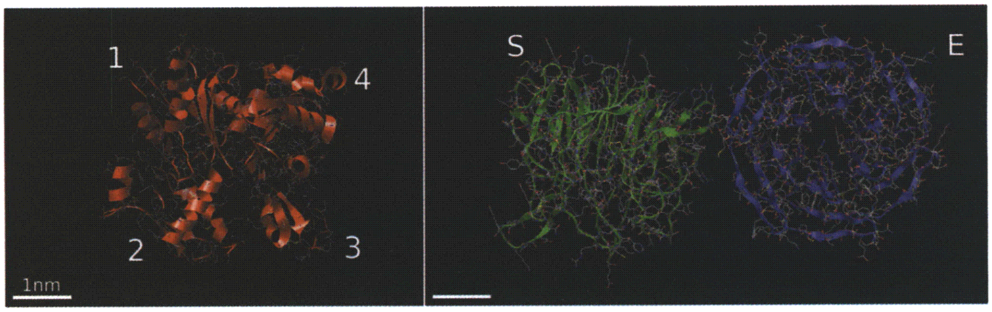

Figure 1-3: Molecular structure of actin (left, from Kabsch *et al* [55]) and scruin (right, from Topf [114]). The actin large domain (subdomains 1-2) is separated from the small domain (subdomains 3-4) by the cleft. The scruin structure was predicted from threading models of TD reconstructions. In its purified state, the spherical (S) and elongated (E) domains are bridged by calmodulin (not shown). Scale bar: 1 nm.

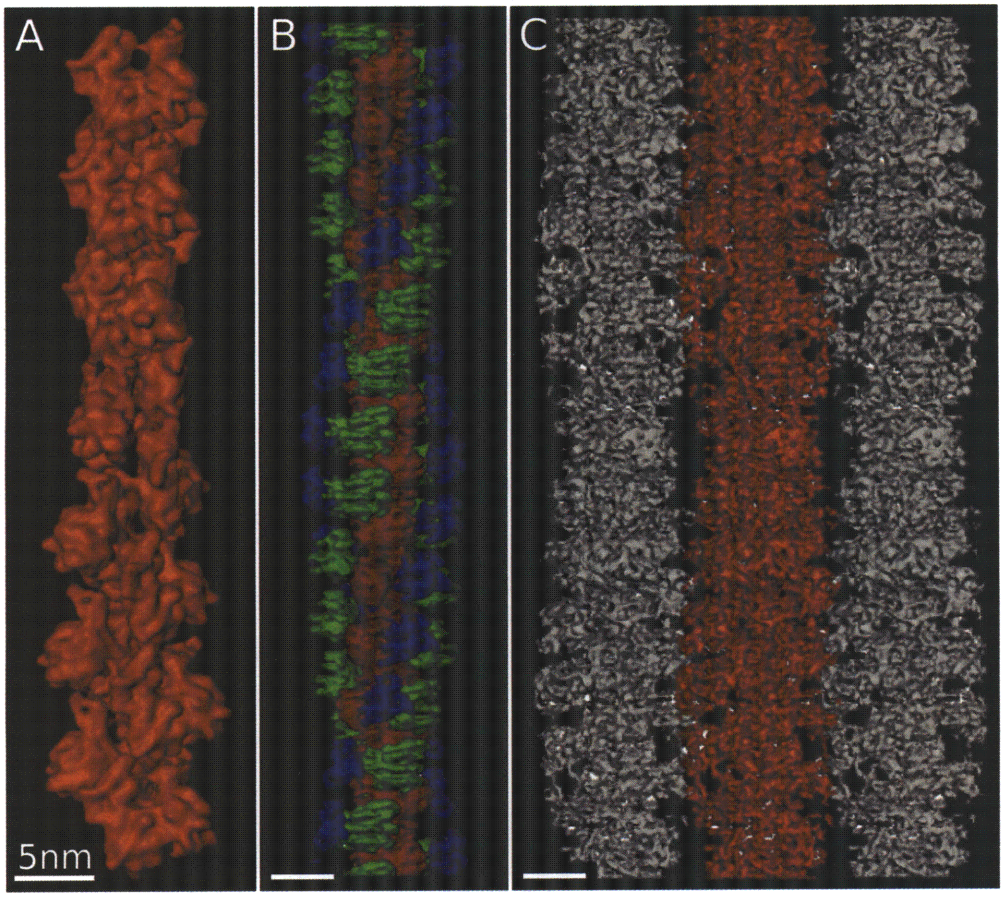

Figure 1-4: Molecular structure of f-actin (A); reconstruction of a single actin scruin filament from an averaged true discharge (B); and arrangement of adjacent actin scruin filaments in the averaged true discharge (C). Images from Schmid *et al* [92]. Scale bar: 5 nm.

α-scruin and is localized to the anterior acrosomal vesicle. (α-scruin will be referred to as scruin from here on.) [119, 120]. When purified from the true discharge, scruin is a 120 kD protein with two domains: one spheroidal (S, N-terminal), the other elongated (E, C-terminal); bridged by calmodulin (an 18 kDCa^{2+}-binding protein). The radius of gyration was determined by x-ray scattering to be 4.63 nm in EGTA (a Ca^{2+} chelator) and 4.83 nm in Ca^{2+} [116]. This conformation change is implicated in the untwisting of the coil (0.23° overtwist per monomer, no Ca^{2+}) into the TD (zero twist, Ca^{2+}).

Although the crystal structure of scruin has yet to be determined, cryo-electron tomography of the true discharge has been used to thread the scruin sequence into an approximate structure (without calmodulin, see Figure 1-3). This structure proposes a β-propeller motif for both domains, consistent with a biochemical analysis of actin binding sites in scruin [102, 114]. The threading model was based on extensive work undertaken in acrosome reconstructions wherein purified TD were embedded in vitreous ice and imaged at various tilt angles by cryo-electron microscopy [17, 80, 87–89, 91, 93]. Tomograms were reconstructed from the tilt planes using filtered back projection producing a cartesian density map for each acrosome. Analysis of multiple maps revealed a 13 turn, 28 monomer (14 actin, 14 scruin) unit cell with 14.4-14.7 nm interfilament spacing. An averaged single filament map was accurate to 9.5 Å, sufficient resolution to fit the Holmes f-actin models (Figure 1-4) [92]. Compared to the Holmes model, acrosomal actin showed twist variations of -10° to +24°, implying significant filament flexibility [28, 39]. With the actin filament core docked into the filament map, scruin must account for the remaining density. This revealed that scruin fully decorates the outside of the f-actin filament (in a 1:1 stoichiometry with actin) and that a single scruin monomer bridges across the double helix to contact two adjacent actin monomers. The scruin E-domain binds to actin subdomain 3 on one helix while the S-domain branches over to actin subdomain 1 on the opposite helix [90]. Crosslinking of individual actin scruin filaments into the bundle was found to be due to interactions between adjacent scruin S-domains. Furthermore, these scruin-scruin crosslinks occurred independently of Ca^{2+} or excess calmodulin [86].

Bulk rheology of actin networks reconstituted at low scruin concentrations revealed a shear modulus of 0.1-300 Pa, dependent on the initial actin-scruin ratio. Confocal microscopy of these networks revealed bundles of scruin crosslinked actin whose diameter increased with increased scruin.

1.3.2 Paracrystals and Depletion Agents

Actin can be also be directly packed into bundles via depletion agent or divalent cations, allowing bundle properties to be studied independently of any actin-binding proteins.

Actin polymerization at higher Mg^{2+} concentrations (typically 25-100 mM) results in the formation of regular actin paracrystals [42, 69, 75, 78]. The observed interfilament spacings of 6-8 nm are less than the actin filament major axis diameter (9 nm) indicating significant interlocking between filaments. Other divalent cations (as well as trivalent Gadolinium ions) gave rise to similar structures, believed to be due to a combination of charge screening and cation crosslinking [3, 4, 35, 101, 106, 122].

Depletion agents such as dextran and PEG (polyethylene glycol) are often used to induce bundling of actin filaments. For high concentrations and low molecular weights, these cause a local increase in monomer concentration (evident by an increase in kinetics). At higher molecular weights and lower concentrations, they affect filaments rather than monomers (causing filament bundling but little change in kinetics) [67]. The bundling effect is due to osmotic pressure (originally described by Asakura and Oosawa [7]) which induces a phase separation between the depletion agent containing bulk and the actin filaments [45, 51, 103]. Experiments with 6 kD PEG at various concentrations (1-8%) resulted in crosslinked actin bundles with no evidence of PEG incorporation [108]. Crosslinking, due to weaker divalent cation interactions and disulfide bond formation, was irreversible in Mg^{2+} or Ca^{2+} [48].

1.4 Mechanics of Actin Filaments

Studies of actin filament material properties have focused on its mechanical response under bending, tension and torsion. Bending and torsion studies measure filament rigidity β_f

$$\beta_f = E_f I_f, \tag{1.2}$$

while tension experiments measure filament stiffness k_f (where $k_f = E_f A_f$). Here A_f is the filament area, I_f is the filament moment of area, and E_f is the elastic modulus, an intrinsic material property consistent between the three modalities. To accurately estimate E_f a filament radius r_f must be assumed, however, due to the forth power dependence of moment of area on radius

$$I_f = \frac{\pi r_f^4}{4}, \tag{1.3}$$

small changes in assumed filament radius can have a significant effect on the final elastic modulus. The actin filament geometry from structural studies reveals a minor-axis radius of 2.7 nm and a major-axis radius of 4.5 nm, though f-actin is typically modeled as an isotropic rod of average radius 2.4-4.0 nm [10, 14, 52, 70]. A common estimate derived from the 25 nm^4 Holmes model cross-sectional area gives a radius of 2.8 nm [50, 59]. For consistency of comparison, all elastic modulus estimates quoted herein have been restated in terms of this 2.8 nm radius. Bending rigidity has also been quoted interchangeably with persistence length ℓ according to

$$\beta = \ell K_b T, \tag{1.4}$$

where K_b is Boltzmann's constant and T is temperature.

Tension

Actin filaments were suspended between two glass needles and subject to tension using a piezo stage while the extension of the filament was measured on a photodiode [59]. The linear stiffness k_f of a 1 μm long phalloidin actin filament was 65.3 ± 6.3 pN/nm with tropomyosin and 43.7 ± 4.6 pN/nm without tropomyosin. The corresponding elastic modulus for filaments without tropomyosin was 1774 ± 187 MPa, which agrees well with the 1786 MPa predicted by theoretical models [10]. The elastic modulus of phalloidin-free actin tropomyosin filaments under tension was measured in an optical trap and found to be an order of magnitude lower at 99-159 MPa, however this is not consistent with the bulk of the literature [2].

Bending

Analysis of thermal fluctuations is a robust technique for the estimation of the persistence length and hence the bending rigidity (from Equation 1.4) of single actin filaments. One or more of the following measures is commonly used: end to end distance as a function of arc length; cosine correlation as a function of arc length; or variance of modal amplitudes. The latter two methods require a freely fluctuating actin filament whose motion is restricted to a two-dimensional plane (by direct confinement or depletion agent). Timelapse images of individual filaments are skeletonized and the filament shape expressed in terms of its arc length s and tangent angles θ. The cosine correlation between θ and s can be directly fit by a negative exponential with persistence length as the primary parameter. Alternatively, the mode shapes for each skeletonized filament can be calculated and the amplitude variance

σ_j^2 for each mode j over all frames together with the wavenumber $k_j = \frac{j\pi}{L}$ used to estimate the per-mode persistence length ℓ_j

$$\ell_j = \frac{1}{k_j^2 \sigma_j^2}, \tag{1.5}$$

(see Supplemental Section A.1 for the complete derivation).

For phalloidin actin filaments the average persistence length ℓ_f generally falls the range 14.7-19.0 µm [13, 34, 47, 53, 62, 79, 124]. Modeling of persistence length is reasonably consistent, predicting 14.2-16.0 µm for ATP-actin [10, 23, 24]. Lower persistence lengths of 1.8-7.4 µm have been reported (using thermal fluctuations or direct manipulation by an optical trap) however these are inconsistent with the bulk of the literature [38, 56, 57, 85].

Phalloidin-free filaments are half as stiff, showing a persistence length of 9-9.8 µm; while phalloidin-free cofilactin filaments are an order of magnitude softer at 2.2 µm (a conformation change in actin subunit 2 is implicated in this increased flexibility) [53, 70, 77]. Troponin also decreases the persistence length, from 18 to 12 µm, while tropomyosin increases it from 18 to 20 µm [53]. Persistence length is independent of bound cation, with the same persistence length of 14.7 µm observed for Mg^{2+}- and Ca^{2+}-bound filaments [124].

For comparison with tension and torsion studies, a persistence length measurement of 18.0 ± 1.0 µm corresponds to a bending rigidity β_f of

$$\beta_f = 7.3 \pm 0.4 \times 10^{-26}\ \mathrm{Nm}^2, \tag{1.6}$$

and an elastic modulus E_f of

$$E_f = 1519 \pm 84\mathrm{MPa}, \tag{1.7}$$

close to the 1774 MPa observed for actin filaments in tension [53].

Torsion

Analysis of the angular vibrations of actin filaments was used to determine the torsional rigidity of Ca^{2+}-bound phalloidin actin filaments. This technique is the angular analog to the linear persistence length method. Two independent experiments measured a torsional rigidity τ_f of 8.0 ± 1.2 and 8.5 ± 1.3 $\times 10^{-26}$ Nm^2 [115, 124]. Torsion models predict a lower rigidity of 3.7 $\times 10^{-26}$ Nm^2, closer to the 2.6 $\times 10^{-26}$ Nm^2 for

Table 1.2: Elastic modulus of phalloidin actin filaments in tension, bending and torsion. Estimates are stated in terms of the cross-sectional area derived radius (2.8 nm).

	E_f (MPa)
tension	1774 ± 187
bending	1519 ± 84
torsion	2486 ± 373

Mg^{2+}-bound filaments [10, 124].

The elastic modulus is determined from the torsional rigidity by

$$\tau_f = G_f J_f, \tag{1.8}$$

where the polar moment of area $J_f = \frac{1}{2}\pi r_f^4$ and the shear modulus G_f is

$$G_f = \frac{E_f}{2\,(1+\nu_f)}, \tag{1.9}$$

here Poisson's ratio ν_f is assumed to be 0.5 [54].

For a torsional rigidity of $8.0 \pm 1.2 \times 10^{-26}$ Nm^2 and an assumed filament radius of 2.8 nm the elastic modulus is 2486 ± 373 MPa, higher than both tension (1774 MPa) and bending (1519 MPa).

Isotropic Rod Model

For the constant radius isotropic rod model of actin filaments to be valid, the elastic modulus must be consistent between tension, torsion and bending (see Table 1.2). Tension and bending estimates are generally in agreement (within 20%), however torsion is 40-60% higher. Choice of radius cannot account for this difference as both bending and torsion scale as radius to the forth power, while tension scales as radius squared. Instead, the difference may be due to anisotropy of the filament arising from its helical structure.

1.5 Mechanics of Actin Bundles

The mechanical properties of filament bundles can be classified into one of two regimes – coupled or uncoupled – depending on the nature of the crosslinking [9, 25]. In the uncoupled regime the filaments are not crosslinked, there is no resistance to shear between filaments, and the bundle mechanical properties scale linearly with the number of filaments. In coupled bundles, rigid crosslinking between filaments prevents shear and the rigidity scales as the square of the number of filaments. The bending rigidity for the uncoupled regime β_u is given by

$$\beta_u = E\sum_{j=1}^{N} I \tag{1.10}$$

$$\propto N, \tag{1.11}$$

where N is the number of filaments, E is the filament elastic modulus, and I is the filament moment of area. For a fully crosslinked bundle, each filament bends about the bundle neutral axis and the coupled bending rigidity is described by the parallel axis theorem

$$\beta_c = E\sum_{j=1}^{N} \left(I + Ax_j^2\right) \tag{1.12}$$

$$\propto N^2, \tag{1.13}$$

where A is the filament area and x_j is the distance from the j^{th} filament center to the neutral axis. For bundles with tens of filaments, coupled bending rigidity is orders of magnitude higher than uncoupled.

1.5.1 Acrosome Material Properties

Bending measurements were performed on the phalloidin-free true discharge using two different methods: steady state hydrodynamic flow and direct manipulation by magnetic tweezers [94, 95, 97]. Sperm were extracted from *Limulus*, washed and immobilized on a coverslip in a flowcell chamber. Steady state hydrodynamic flow was induced through the flowcell and the bending of the true discharge measured by video microscopy. The path of tracer beads in solution provided an estimate of the flow rate. A tapered rod model based on the geometry of the true discharge was applied to estimate the elastic modulus

$$E_{td} = 2500 \pm 720 \text{ MPa}, \tag{1.14}$$

while a constant radius R_{td} of 46 nm provided a similar estimate

$$E_{td} = 2380 \pm 810 \text{ MPa}. \tag{1.15}$$

Given the moment of area

$$I_{td} = \frac{\pi R_{td}^4}{4}, \tag{1.16}$$

the bending rigidity β_{td} was

$$\begin{aligned} \beta_{td} &= E_{td} I_{td} & (1.17) \\ &= 84 \pm 28 \times 10^{-22} \text{ Nm}^2, & (1.18) \end{aligned}$$

four orders of magnitude stiffer than a single filament ($7.3 \pm 0.4 \times 10^{-26}$ Nm^2 from Equation 1.6).

For the magnetic trap experiments, sperm were biotinylated prior to immobilization and streptavidin coated beads attached to the TD end. The force displacement characteristics of the magnetic trap were calibrated and used to determine the bundle stiffness. Applying the tapered rod model

$$E_{td} = 1340 \pm 340 \text{ MPa}, \tag{1.19}$$

half that of the hydrodynamic flow measurements. A constant radius model was not presented, however the bending rigidity can still be estimated using the product of the tapered rod elastic modulus (Equation 1.19) and the constant radius moment of area (Equation 1.16)

$$\beta_{td} = 47 \pm 12 \times 10^{-22} \text{ Nm}^2. \tag{1.20}$$

Hydrodynamic flow was also used to bend the phalloidin-free false discharge, resulting in a bending rigidity β_{fd} of

$$\beta_{fd} = 23 \pm 3 \times 10^{-22} \text{ Nm}^2, \tag{1.21}$$

one quarter the stiffness of the true discharge. Assuming a constant radius R_{fd} of

Table 1.3: Mechanical properties of the true and false discharge.

	experiment	β ($\times 10^{-22}$ Nm^2)	E (MPa)
TD	magnetic trap	47 ± 12	1340 ± 340
TD	hydrodynamic flow	84 ± 28	2500 ± 720
FD	hydrodynamic flow	23 ± 3	1519 ± 84

62 nm the elastic modulus E_{fd} becomes

$$E_{fd} = 198 \pm 22 \text{ MPa}, \tag{1.22}$$

one order of magnitude lower (due to its larger radius) than the TD [105].

These results are summarized in Table 1.3 – the significant differences between the mechanical properties of the TD and FD are believed to be a direct result of the conformation change of scruin in Ca^{2+} over EGTA.

1.6 Research Goals

This thesis presents a comprehensive study of the mechanical properties of crosslinked actin bundles inspired by the *Limulus* acrosomal process. In Chapter 2 actin filaments, which form the core of all bundles, are examined and their persistence length and structure determined. Depletion agents are used to induce actin-only bundle formation allowing the probing of bundle properties absent any actin-binding proteins. Scruin decorated actin filaments are studied in Chapter 3 and their persistence length in both Ca^{2+} and EGTA determined. True and false discharge fragments together with actin and scruin are used to reconstitute the acrosomes two main conformations – the true and the false discharge – and their structure is studied by high resolution electron microscopy.

Bending rigidities of reconstituted bundles are directly measured by optical tweezers. This represents a novel new technique that allows for the comparison of bundles formed by depletion agent or crosslinking protein. It also allows, as presented in Chapter 4, for the mechanical properties of bundles to be described in terms of the material properties of their individual filaments. This reveals interesting new insights into the nature of actin bundle formation and the role of scruin as a crosslinking protein.

Chapter 2

Actin

This chapter presents techniques developed to: purify monomeric actin; polymerize monomers into filaments; characterize filament persistence length; induce bundle formation by depletion agent; measure the kinetics of bundle formation; and measure bundle bending rigidity by optical tweezers. Some of these protocols (purification, polymerization and persistence length) are well established in the literature and serve as experimental controls. Others (kinetics and mechanics of bundle formation) represent new techniques to elucidate the material properties of actin filaments and bundles.

2.1 Actin Monomers and Filaments

Monomeric actin was prepared from rabbit skeletal muscle using protocols originally developed by Spudich (see also Supplemental Section B.1.2) [99]. First, frozen rabbit muscle was ground into pulp then washed in an extraction buffer (100 mM NaH_2PO_4 pH 6.5, 300 mM KCl, 50 mM Na_2HPO_4, 3 mM NaN_3, 1 mM $MgCl_2$, 10 mM EDTA, 50 µM PMSF, 2.5 mM ATP) to dissociate myosin from actin. The remaining pulp was repeatedly washed and filtered through cheesecloth before treatment with acetone to produce a dry stable powder which can be stored at -20°C for up to several years. Next, the powder was washed in a second extraction buffer (2.5 mM Tris pH 8, 0.1 mM ATP) then spun down and filtered to remove contaminants. The filtrate was polymerized overnight into a viscous solution of filamentous actin by adding a mild polymerization buffer (10 mM NaCl, 0.7 mM $MgCl_2$). Filaments were spun down at high speed (3 hours at 50,000 rpm) and resuspended in fresh g-buffer (5 mM Tris pH 8, 0.2 mM $CaCl_2$, 0.2 mM ATP, 0.5 mM DTT, 0.1 mM NaN_3) and injected into a dialysis bag for depolymerization. With fresh buffer exchanges every day, depolymerization was allowed to proceed for several days. Finally the dialyzed solution was spun down at high speed (2 hours at 50,000 rpm) and the top 100 µl kept for experiments. The pellet was resuspended in the remaining supernatant, immediately re-polymerized and stored as filamentous actin for up to several months. Repeated polymerization and depolymerization cycles could then be performed to exchange between monomeric and filamentous actin (bypassing the initial acetone extraction steps). Monomeric actin stored in g-buffer at 4°C was used within one week.

Dynamic light scattering (DLS) was used to estimate the hydrodynamic radius of g-actin and to provide a measure of the proportion of monomers in solution. For the hydrodynamic radius experiments, a purely monomeric species was desirable so fresh g-actin was first spun through a 100 kD spin filter (Millipore) to remove any oligomers. The resultant hydrodynamic radius was 3.0 ± 0.2 nm (1 sample, 600 measurements, shown in Figure 2-1 together with the 1ATN crystal structure). To determine the monomer percentage, the supernatant was tested immediately after centrifugation (without prior filtration) and the species histogram computed. Typically, the solution was measured to be 98% monomeric, indication of a successful purification.

For the reconstitution experiments, g-actin was polymerized into f-actin by adding 1 µl of 10× f-buffer (50 mM KCl, 2 mM $MgCl_2$) to 9 µl of g-actin (50 nM to 10 µM). Filaments were imaged in a JEOL 2200 FS electron microscope at 200 kV with 2% uranyl acetate negative stain. The average filament radius r_f measured from these images (4 filaments, 120 measurements, see Figure 2-2) was

$$r_f = 3.2 \pm 0.7 \text{ nm}. \tag{2.1}$$

This average radius represents an intermediate estimate between the cross-sectional area derived radius (2.8 nm) and the major-axis radius (4.5 nm). Filaments were also labeled at 1:1 stoichiometry with a phalloidin conjugated fluorophore (Alexa-488, Sigma) and diluted to nanomolar concentrations for fluorescence imaging. At such low concentrations, individual filaments were clearly distinguishable; at higher concentrations networks predominate.

2.2 Mechanical Properties of Actin Filaments

Actin filament persistence length (interchangeable with bending rigidity by Equation 1.4) was determined by analysis of thermal fluctuations. To obtain single filaments, g-actin was polymerized at 1 µM (for 30-60 minutes in 1 µM phalloidin) and

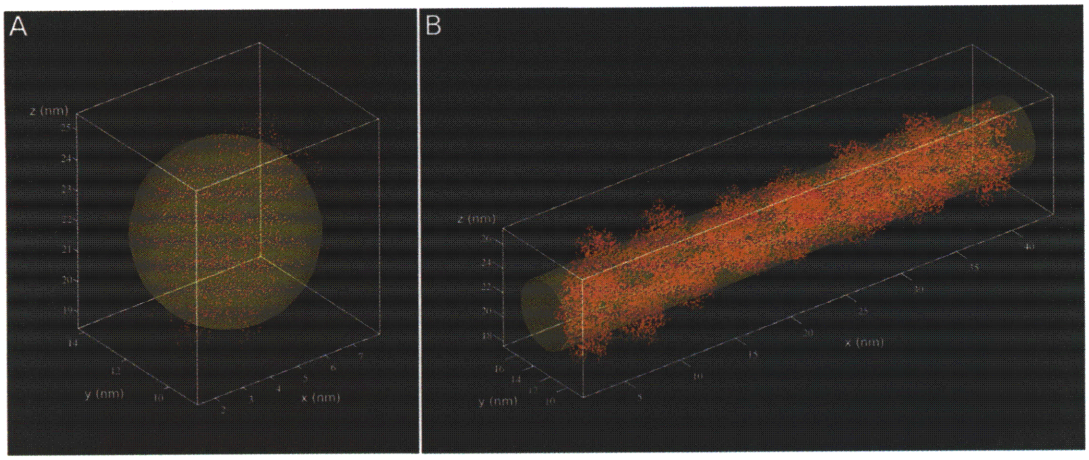

Figure 2-1: Molecular structure of monomeric (A) and filamentous actin (B). The structures from Kabsch and Holmes are shown in red with the average radius (from dynamic light scattering or direct measurement) overlaid in yellow [50, 55]. Both average radiuses are suitable approximations for the underlying structure.

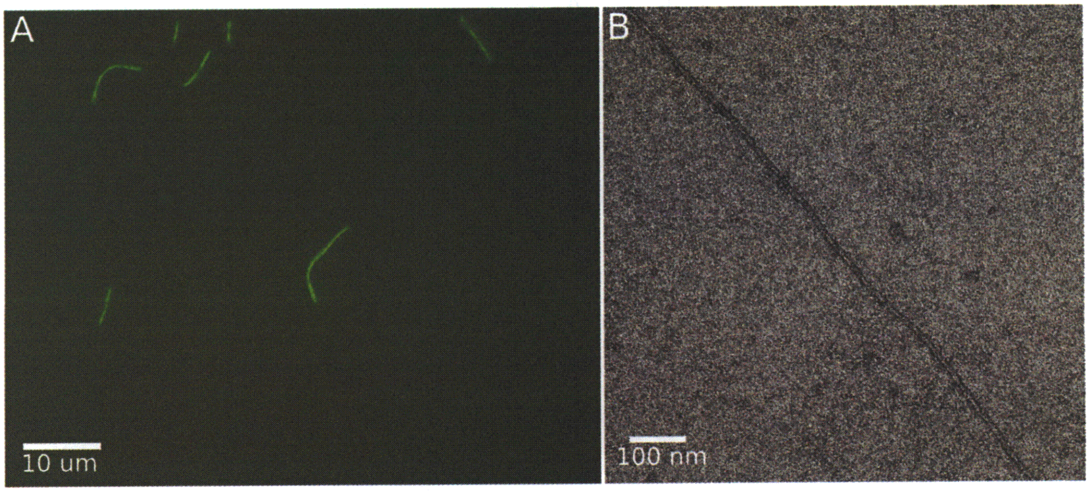

Figure 2-2: Microscopy of actin filaments. Fluorescence imaging of single actin filaments (A) was used to determine the persistence length from thermal fluctuations, while electron microscopy (B) revealed a single filament radius of 3.2 ± 0.8 nm.

the resultant f-actin diluted to 10 nM for imaging. Meanwhile, a flowcell was constructed from a cleaned slide and coverslip separated by 100 μm thick double sided tape to form a channel 5-10 μl in volume (see Appendix Figure B-2). To prevent non-specific binding of the filaments to the coverslip, the channel was incubated for several minutes in 10 mg/ml casein (which proved considerably more effective than BSA). In addition to the 10 nM f-actin, the following components were added immediately prior to imaging: 0.5 mg/ml casein for ongoing blocking; 20mM lactic acid and 1:50 Oxyrase to reduce fluorophore bleaching; and 2% dextran sulfate to confine the filaments to the surface of the coverslip. Filaments were imaged in a Nikon widefield 100× fluorescence microscope using a FITC filterset. Combined with the Alexa-488 phalloidin labeling, this provided a strong fluorescence signal with a narrow point spread function. Frames were sampled at 2 Hz for 200-500 frames. No samples showed evidence of bundle formation due to the dextran sulfate.

For each image in the sequence the filament was skeletonized, smoothed into a continuous $x-y$ trace and converted to $s-\theta$ space (where θ is the tangent angle at arc length s along the filament, see Figure 2-3). This transformation is necessary as the modal analysis requires a constant length L which is not guaranteed in $x-y$ space. A fourier series was then fit to the $s-\theta$ waveform and the amplitude coefficients a_j calculated from

$$a_j = \sqrt{\frac{2}{L}} \int_0^L \theta \cos(k_j s), \tag{2.2}$$

where L is the filament length, $k_j = \frac{j\pi}{L}$ is the wavenumber, and j is the mode number (typically the first 9 modes were used). The variance of a_j provides an independent persistence length estimate for each mode j (see the derivation in Supplemental Section A.1). For a dataset to be included in the final analysis, the filament length had to remain constant for the entire timelapse and the persistence length estimates for each mode were required to converge after several hundred frames. A sharp decrease in the persistence length trace for any mode may indicate a breakage, or a significant change in filament shape; while an increase may indicate that the filament is stuck.

An additional validation plots the log of the amplitude coefficient variance against the log of the wave number and compares the slope to that predicted by bending theory. Restating Equation A.21

$$\ell_j = \frac{1}{k_j^2 \sigma_j^2}, \tag{2.3}$$

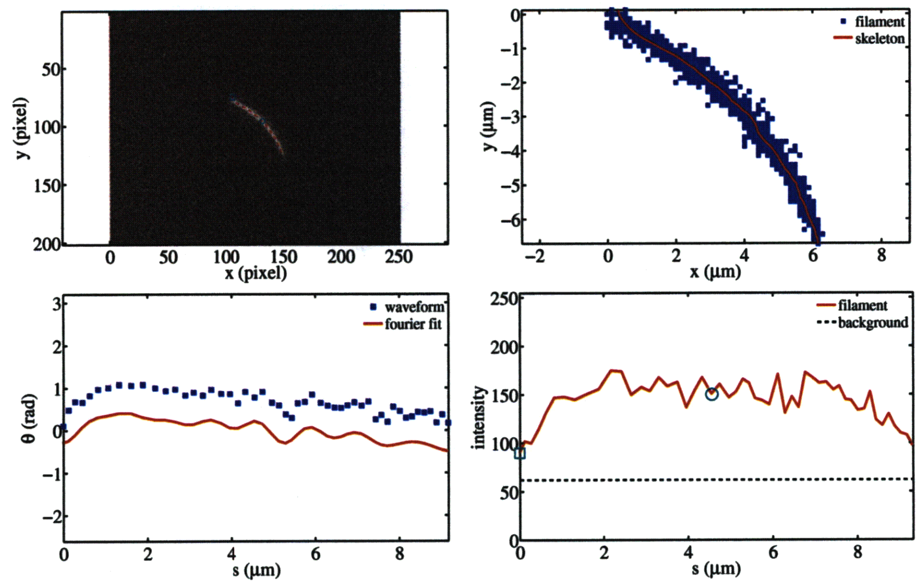

Figure 2-3: Fourier reconstruction of actin filament shape. Clockwise from top left: original greyscale image and skeleton (red, the cyan square is the start of the filament, the circle its midpoint); thresholded filament (blue) and skeleton (red); intensity profile of filament (red) as a function of arc length s and median background intensity (black); filament tangent angle θ (blue) and fourier fit (red).

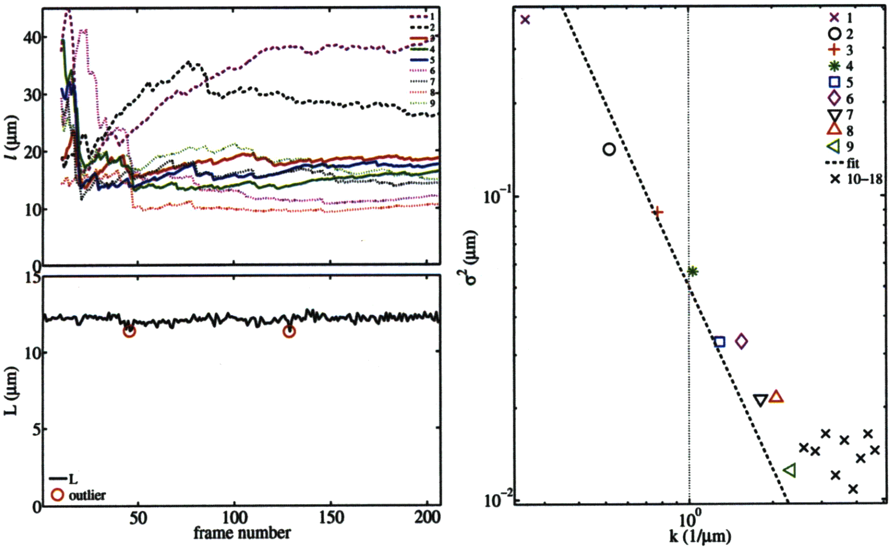

Figure 2-4: Persistence length fit for actin filament. Clockwise from top left: persistence length estimate ℓ for all modes (1-9) over all frames (1-210) for a single actin filament; amplitude coefficient variance σ^2 as a function of wavenumber k; filament length L over all frames. For this filament the average persistence length was 19.9 µm.

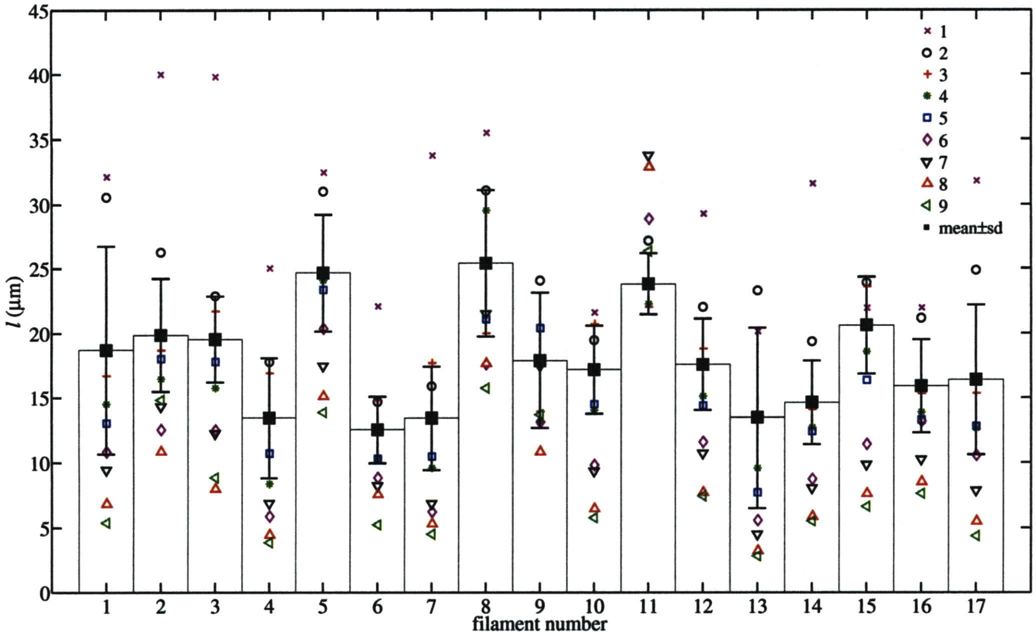

Figure 2-5: Mean persistence length ℓ of all actin filaments (1-17). The symbols represent the individual modal estimates, the errorbars the mean and standard deviation for modes 2-5. Lower modes (1-2) tend to overestimate while higher modes (6-9) tend to underestimate the persistence length. The average persistence length over all filaments in 17.9 ± 4.0 µm.

and taking the log of both sides gives

$$\log \sigma_j^2 = -2 \log k_j - \log \ell, \tag{2.4}$$

so a plot of $\log \sigma_j^2$ against $\log k_j$ has slope -2 and intercept $-\log \ell$ (Figure 2-4). For these plots, the lower modes generally fall below the fitting line indicating there are insufficient frames to fully capture the sample space of these high amplitude modes, while the higher modes typically lie above the line as these are dominated by noise.

For all valid datasets (17 in total, see Figure 2-5) the persistence length was

$$\ell_f = 17.9 \pm 4.0 \ \mu\text{m}, \tag{2.5}$$

which compares well in both mean and standard deviation to the literature (14.7-19.0 µm). The equivalent bending rigidity is

$$\beta_f = 7.3 \pm 1.6 \times 10^{-26} \ \text{Nm}^2. \tag{2.6}$$

Invalid datasets (96 in total) were disregarded due to: insufficient frames (fewer than 200); poor convergence; or filament length standard deviation too high (above 0.5 µm). Additionally, a number of shorter filaments (8 in total, all shorter than 5.5 µm) displayed a low persistence length of 6.3 ± 2.3 µm. This arises because shorter filaments have lower amplitudes and are more subject to noise. Here the cutoff length was manually determined in order to separate the two distributions.

2.3 Acrosome Seeds

The true and false discharges were purified according to the protocols described in Appendix Section B.1.5. Both methods are nearly identical and involve induction of the acrosome (in high Ca^{2+} for the TD or high salt for the FD) followed by demembranation and washing. Purified acrosomes are typically 5-10 µm long and show the characteristic crystalline structure when viewed under the electron microscope (see Figure 2-6). They can be stored for up to two months in a-buffer (10 mM Tris pH 8, 1 mM $CaCl_2$, 100 mM NaCl, 3 mM NaN_3, 0.5 mMDTT).

Short seeds with fresh interfaces are desirable for the bundling experiments so samples were sonicated for 30-60 seconds at 3 W (in a Misonix probe tip sonicator). The length of the sonicated fragments depended on the sonication conditions: from 659 ± 155 nm under stronger sonication (100% duty cycle, 45-60 seconds) to 1006 ± 422 nm under lighter sonication (20-50% duty cycle, 30 seconds). Seed radius was found to be independent of the sonication conditions but showed some variation between samples, ranging from 49 ± 7 nm to 59 ± 8 nm. The combined statistics for all seeds (TD and FD combined) revealed an average length L_t (111 seeds measured) of

$$L_t = 769 \pm 297 \text{ nm}, \tag{2.7}$$

and an average radius R_t (93 seeds measured) of

$$R_t = 53.7 \pm 8.0 \text{ nm}. \tag{2.8}$$

The seed interfilament spacing was primarily determined using fourier analysis of electron micrographs (by taking the fast fourier transform – FFT– of high resolution images). This method provides the additional benefit of indicating the arrangement of filaments within the bundle. A seed and its fourier transform are shown in Figure 2-6, showing a 2.8 nm actin rise, a 12.7 nm projected lattice spacing and a 39 nm unit cell length. These compare favorably with the literature: 2.7 nm for the rise, 12.6 nm for

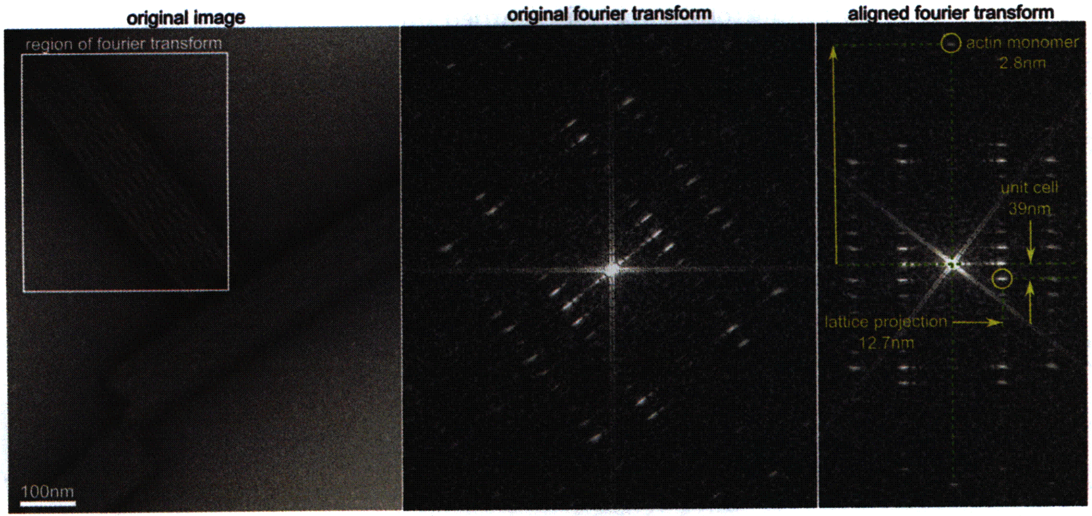

Figure 2-6: Fourier transform of true discharge seeds. Original image (left) and fourier transform (middle) of selected region. The FFT was rotated to align the 2.8 nm actin peak with the vertical axis (right).

the projected lattice spacing and 38.3 nm for the unit cell length [17, 52, 92]. The FFT diffraction pattern was consistent with that of an hexagonally packed structure, so the interfilament spacing t_t can be related to the projected lattice spacing dx by

$$dx = t_t \cos\left(\frac{\pi}{6}\right), \tag{2.9}$$

giving a filament spacing of

$$t_t = 14.9 \pm 0.4 \text{ nm}, \tag{2.10}$$

(5 bundles measured), which compares well to the 14.4-14.7 nm from the literature. A tilt series of a TD seed showed diminished FFT peaks away from the 0° plane, further confirmation of hexagonal packing (see Supplemental Figure A-7).

2.4 Depletion Induced Actin Bundles

Uncrosslinked actin bundles can be readily formed by polymerizing actin in the presence of acrosome seeds – which act as preferential nucleation sites for filament growth [66, 121] – but the bundles formed are irregular and divergent (see Figure 2-7).

High molecular weight polymers such as PEG (polyethylene glycol) and dextran are often used as depletion agents to induce crosslinked actin bundle formation. Dextran (410 kD or 670 kD, Fluka) is an inert branched polymer approximately 25 nm

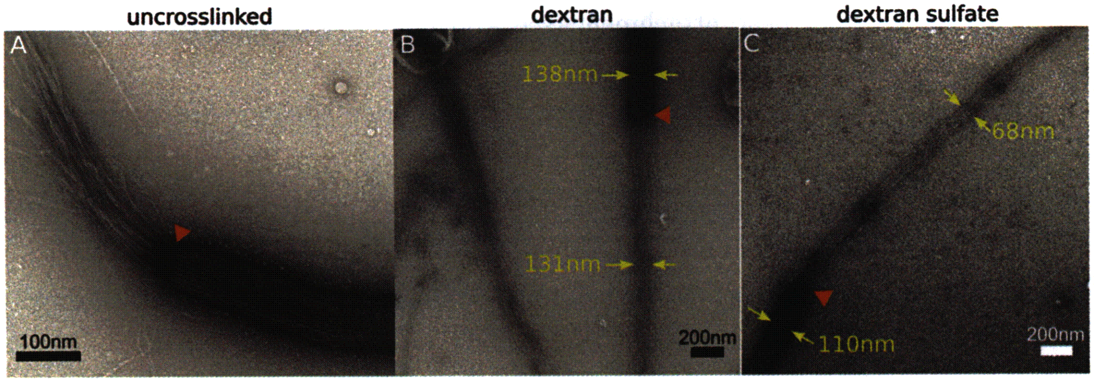

Figure 2-7: Electron microscopy of crosslinked and uncrosslinked bundles. Seeded bundles formed by dextran (B) showed looser packing than those formed by dextran sulfate (C). Bundles formed without a depletion agent showed no regular packing of filaments (A).

long that creates a phase separation between the filaments and the bulk [74]. Osmotic pressure and weak divalent cation interactions serve to pack the filaments into bundles. A variant, Dextran sulfate (500 kD, Sigma), incorporates negative sulfur atoms into the polymer chain to provide an additional electrostatic component to the depletion force. The high molecular weight of both these agents will preferentially exclude filaments rather than monomers.

Seeded and crosslinked actin bundles, formed in a flowcell with dextran or dextran sulfate, were imaged under phase microscopy to measure growth kinetics, and bent with an optical trap to probe their mechanical properties (see Appendix Figure B-3). These flowcells were slightly different from their persistence length counterparts: the coverslip was first coated with BioBond (Electron Microscopy Sciences) then sonicated seeds were flowed into the channel and incubated for 5 minutes to allow them to stick to the BioBond. The unbound seeds were flushed out with a double volume of a-buffer then incubated in casein for several minutes to block the remaining coverslip surface. The flowcell was transferred to the microscope stage and a suitable seed located for timelapse imaging. The casein was flushed out with more a-buffer before the actin solution (prepared separately in a PCR tube) was flowed into the channel to begin bundle formation. Typical conditions were 1 μM actin and 2% dextran sulfate for a nominal growth rate of 2 μm/hr with a framerate of 1 Hz. Polymerization was halted by washing out the remaining g-actin with a 2% dextran sulfate solution. Finally gelsolin coated beads were flowed into the channel; these could be captured by the optical trap and attached to the bundle ends for the transverse bending experiments. Gelsolin binds to the barbed end of actin filaments and proved to be a robust and convenient method for bead attachment (see Appendix Section B.1.3).

Under phase microscopy, bundles formed by dextran sulfate were qualitatively denser and straighter than those formed in dextran, implying a tighter packed bundle (see Supplemental Figure A-4). Bundles grew longer and more quickly for increasing actin concentrations, with most bundles straight and convergent over their entire length. Adapting the flowcell method to electron microscopy yielded high resolution images of bundle structure (Figure 2-7), revealing a filament spacing of 8.3 ± 1.4 nm (8 bundles measured).

When the depletion agent was washed out of the flowcell and replaced by regular a-buffer, the bundles floated out of the focal plane as their rigidity decreased (osmotic pressure is required for bundle crosslinking, see Supplemental Figure A-5). Electron microscopy showed a corresponding decrease in filament packing density.

Diffraction patterns for seeded bundles were too weak for the FFT analysis however free bundles formed from actin filaments (without seeds) showed comparable packing but much stronger FFTs (see Figure 2-8 and Figure 2-9). These unseeded bundles were formed by polymerizing 1 μM actin in the presence of 2% dextran sulfate over several hours. Fourier transforms of bundle tilt series revealed no evidence of hexagonal structure (see Supplemental Figure A-8), despite some reports to the contrary [11]. Instead, a polycrystalline structure (some regions are ordered while others are disordered) with square packing was assumed. Direct measurements of the bundle in Figure 2-9 revealed a mean spacing of 8.2 ± 1.3 nm (45 measurements); the fourier transform showed clear peaks at 7.8 nm and 8.2 nm consistent with the direct measurement, as well as a peak at 11.2 nm indicative of looser packed regions within the bundle. The mean filament spacing t_x over multiple bundles (8 in total) was

$$t_x = 8.6 \pm 0.6 \text{ nm}. \tag{2.11}$$

(8 bundles measured), fully consistent with the seeded bundle filament spacing above. This suggests a polarity-free packing mechanism: seeded bundles are aligned as a consequence of seed polarity while unseeded bundles suffer no such restrictions; yet filament spacings in both cases were comparable. Bundles formed overnight showed tighter packing and a mean spacing of 6.8 ± 0.4 nm (5 bundles measured). This indicates that filaments are free to slide past each other in search of lower energy configurations.

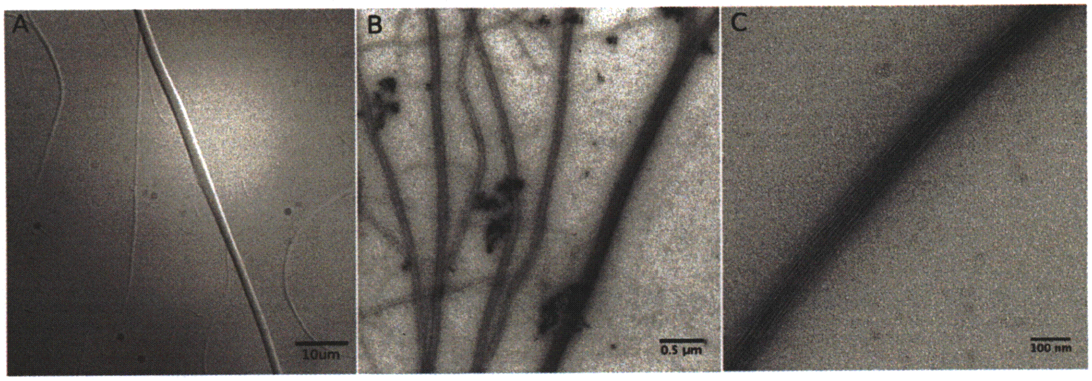

Figure 2-8: Free bundles formed by dextran sulfate. Phase (A) and electron microscopy (B) of bundles formed overnight in 1% dextran sulfate showed long thick actin bundles. Bundles formed in 2% dextran sulfate over 4 hours (C) were narrower due to the reduced incubation time but showed regular tight packing of filaments.

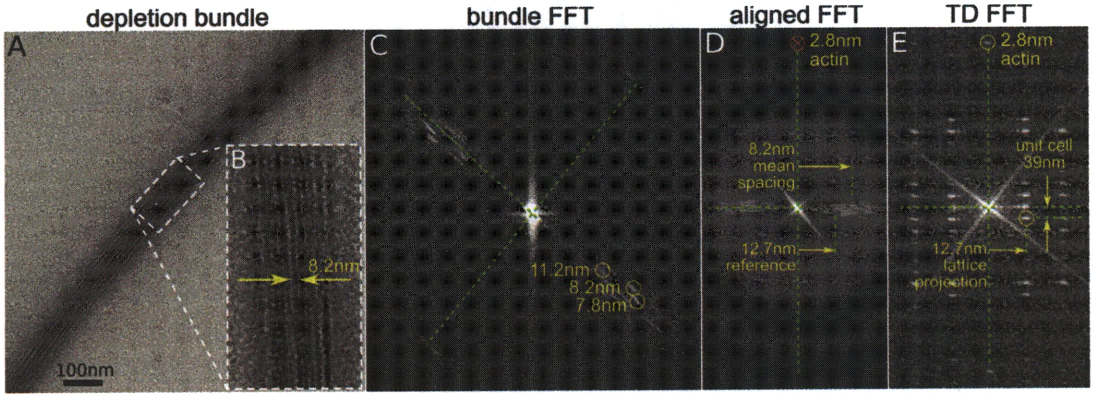

Figure 2-9: Fourier transform of free bundles formed by dextran sulfate. Original image (A) of a free bundle formed by 2% dextran sulfate over 4 hours; inset (B) shows two filaments with spacing consistent with both the mean measured filament spacing of 8.2±0.3 nm and the peaks from the fourier transform (C). The bundle FFT was aligned so the bundle axis was vertical (D). The MTF null occurred at 3.9 nm so it was not possible to resolve the 2.8 nm actin peak, but its nominal location (red cross) is shown for comparison to the true discharge FFT (E, from Figure 2-6).

2.5 Kinetics of Bundle Formation

The flowcell assay described above readily lends itself to the measurement of bundle growth rates and the estimation of kinetic rate constants. For each image sequence, the initial frames showing just the seed were used to define the start of the bundle and the length at subsequent frames was directly measured using the ImageJ software package (National Institutes of Health). For all bundles measured, the length was found to increase linearly over time (data not shown) and the slope of a linear fit to the data provided an estimate of the growth rate. A single bundle at a given actin concentration provided a single growth rate estimate – for a full kinetics dataset, two or more bundles were measured at three or more actin concentrations (for a minimum of six datapoints per dataset). This provided sufficient data for a linear fit: the slope is the on rate k_{on} and the intercept the off rate -k_{off} (see Figure 2-10 and Table 2.1).

Three datasets (24 bundles total) were gathered to determine the effect of: depletion agent (dextran vs dextran sulfate); divalent cation (Ca^{2+} vs EGTA); and seed (TD vs FD). The resultant kinetics were found to be: independent of both depletion agent and seed; consistent with actin filaments for the EGTA bundles; and slightly faster than actin filaments for the Ca^{2+} bundles. The difference between Ca^{2+} and EGTA is noteworthy: EGTA facilitates the exchange of Ca^{2+} for Mg^{2+} thereby promoting filament growth, yet bundles formed faster in Ca^{2+}, perhaps as a result of a higher ionic strength in Ca^{2+} over EGTA.

While on-rates were generally consistent between the measurements, off-rates showed significant variation and some even were negative. This is likely due to the variation of growth rates within each actin concentration group which renders the off-rate estimates less reliable than the on-rates. A more accurate estimate for k_{off} was achieved by direct measurement of bundle depolymerization. Actin bundles were formed as above (in the absence of phalloidin) and after several minutes the flowcell was flushed with g-buffer, triggering depolymerization (as the bulk g-actin concentration falls below the critical concentration). The shortening rate was measured for three bundles and found to be 1.5-1.9 subunits per second, consistent with the literature off-rate of 1.3 subunits per second (see Supplemental Figure A-6).

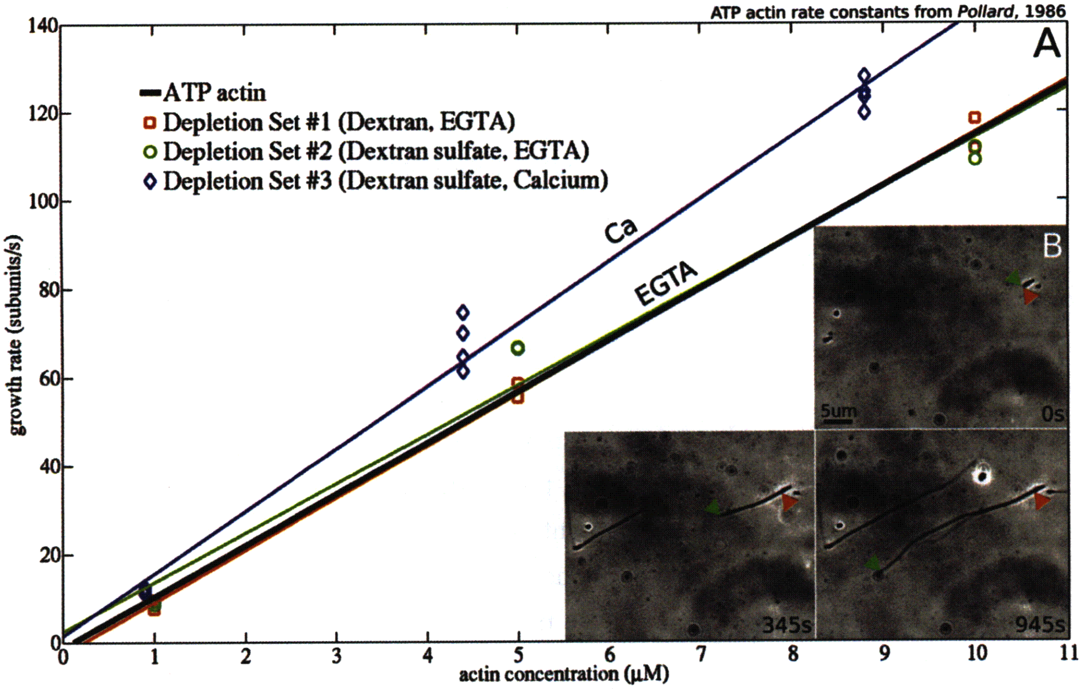

Figure 2-10: Kinetics of phalloidin-free actin bundles (A). Kinetic on- and off-rates for EGTA (red, green) agreed closely with single actin filament kinetics from the literature (black) and independent of depletion agent (dextran or dextran sulfate) or seed (TD or FD). On-rates were slightly higher in Ca^{2+} (blue). Timelapse of bundle formation (B) at 0.9 µM actin revealed a growth rate of 12 subunits per second. The red arrow shows the start of the bundle, the green arrow its end.

Table 2.1: Depletion bundle rate constants. On-rates for EGTA bundles were consistent with the literature and little difference was seen between dextran and dextran sulfate depletion agents. Ca^{2+} bundles showed slightly higher on-rates than those predicted by the Pollard rate constants. Off-rates showed significant variation, likely due to the spread of the data, though direct measurement of depolymerization rates yielded off-rates consistent with the literature.

	k_{on} (1/µMs)	k_{off} (1/s)
Pollard	11.6	1.3
EGTA dextran	11.2	-2.4
EGTA dextran sulfate	11.8	2.8
Ca^{2+} dextran sulfate	14.1	-1.4
depolymerization	–	1.5-1.9

2.6 Bending Rigidity of Actin Bundles

Dextran sulfate bundles were formed in a flowcell with 1 μM actin, equimolar phalloidin and 2% dextran sulfate, and imaged in an optical trap microscope (100x DIC-H). Bundles were polymerized for 2 minutes to a nominal length of 4 μm (based on a growth rate of 2 μm/min from the kinetics) before flushing the flowcell with 2% dextran sulfate to stop polymerization while maintaining bundle structure. Gelsolin coated polystyrene beads (1 μm diameter) were diluted to 1:200 in 2% dextran sulfate then flowed into the chamber. Spontaneous binding of the beads to the bundle end was rare but trapped beads placed against the bundle end tended to attach firmly.

To bend the bundle and measure transverse displacement the bead was trapped in the primary laser and the stage moved perpendicular to the bundle axis. A second laser was used to track the displacement of the bead relative to the trap center, measured as a voltage change across a photodiode. Trap stiffness was determined by measuring the brownian motion of a free bead, the calibration parameters were then used to calculate equivalent forces from the displacement detector voltages [6, 58, 65, 71, 72]. A force displacement curve was then be plotted with the stage displacement along the x-axis and the calibrated trap force along the y-axis (see Figure 2-11).

The transverse deflection of a cantilevered Euler beam is linear with applied force for small displacements (see Supplemental Section A.1). The optical trap is also linear for trap displacements of up to 150 nm. Beyond these limits both bundle and trap will exhibit non-linear behavior. These regions are useful, though, and were used to center the bundle in the trap. First, an initial large displacement "sweep" cycle was used to locate the linear bending region. Then a smaller displacement "pull" cycle was applied to probe the transverse bending characteristics in the region of the bundle neutral axis. Linear regions from both profiles were used to measure the bundle stiffness k. The bending rigidity β can be calculated from k by

$$\beta = \frac{kL}{3}. \tag{2.12}$$

To accurately determine the length L bundles were skeletonized from the microscopy images and fit to the beam bending equations (see Equation A.1, Figure 2-12 and Figure 2-13).

The bending rigidity for all valid dextran sulfate bundles (17 in total, 1 μM actin and 2% dextran sulfate) is shown in Figure 2-14. Invalid bundles (33 in total) were disregarded due to: nonlinear force-displacement curves; inconsistent stiffness between sweep/pull cycles; and inconsistent beam shape. Several bundles exhibited regions of

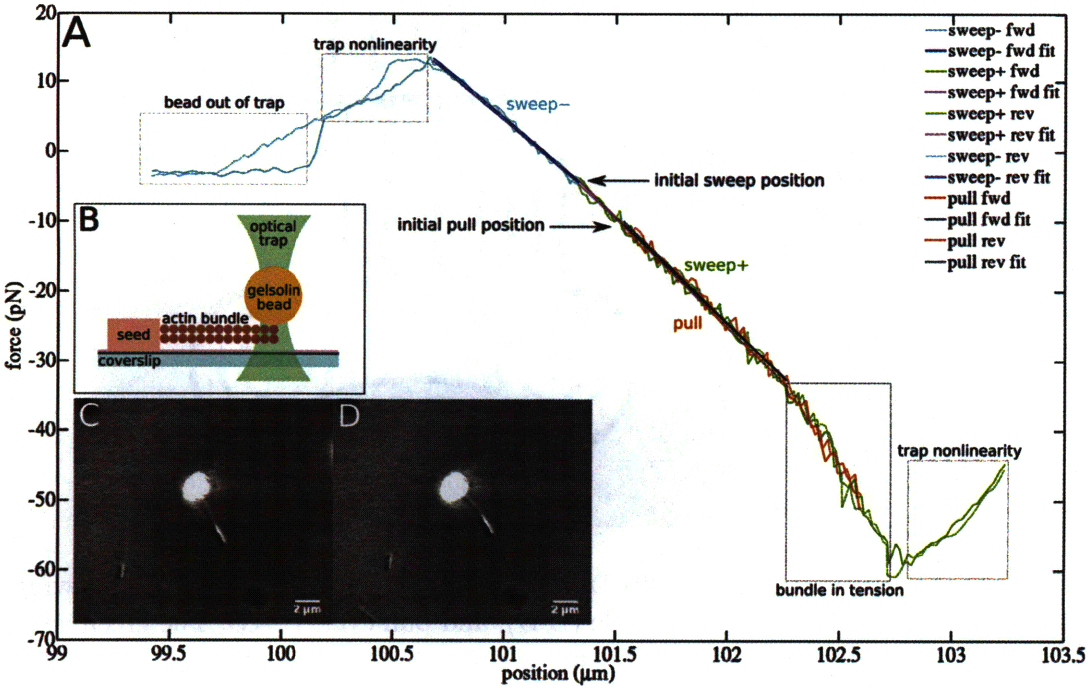

Figure 2-11: Force-displacement plot for optical trap bending of dextran sulfate bundles (A). The slope of the central linear region provides a direct measure of the transverse stiffness k which can be used to estimate the bundle bending rigidity. The regions at far left and far right are characteristic of trap non-linearity. The increased slope at right was due to a transition to a tension regime. A schematic of bundle formation and gelsolin bead binding summarizes the assay setup (B) while phase microscopy captures the bundle shape during the sweep-pull cycles (C-D).

increased stiffness prior to the onset of trap non-linearity, likely due to a transition to a tension-dominated regime. Other bundles showed zero force regimes, typically resultant from bead rotation over the bundle or detachment of bead from bundle entirely. These regions were readily identified from both the force-displacement traces and the video feeds, and not included in the analysis. Bundle lengths varied from 3.0 − 4.8 μm and gelsolin beads were bound to the end of the bundles in all cases.

The mean bending rigidity was

$$\beta_x = 4.4 \pm 2.3 \times 10^{-22}\ \mathrm{Nm}^2, \tag{2.13}$$

several orders of magnitude higher than a single actin filament ($7.3 \pm 1.1 \times 10^{-26}\ \mathrm{Nm}^2$ from Equation 2.6).

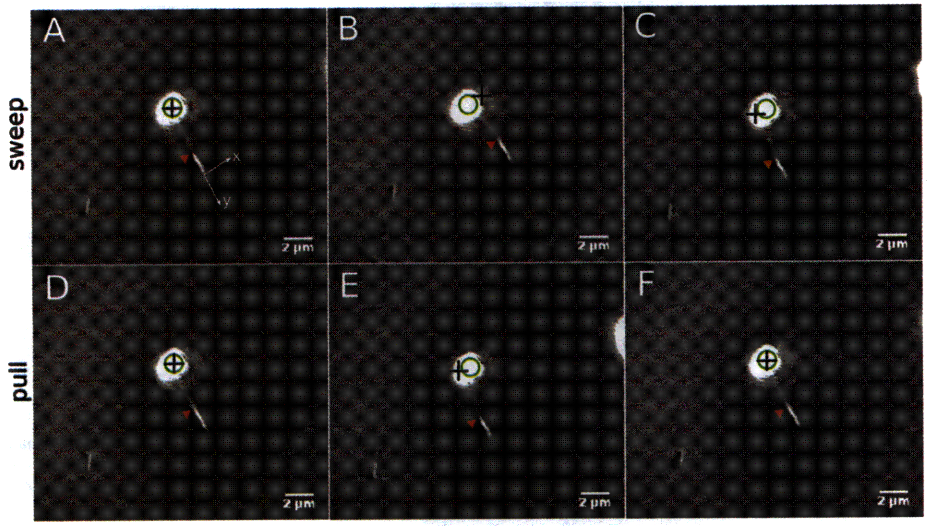

Figure 2-12: Phase microscopy (100x DIC-H) of optical trap bundle bending showing: initial bundle position (A), sweep cycle (B-D), and pull cycle (E-G). The green circle shows the instantaneous trap center; the cross-hairs the initial trap position; while the red arrow indicates the seed-bundle interface.

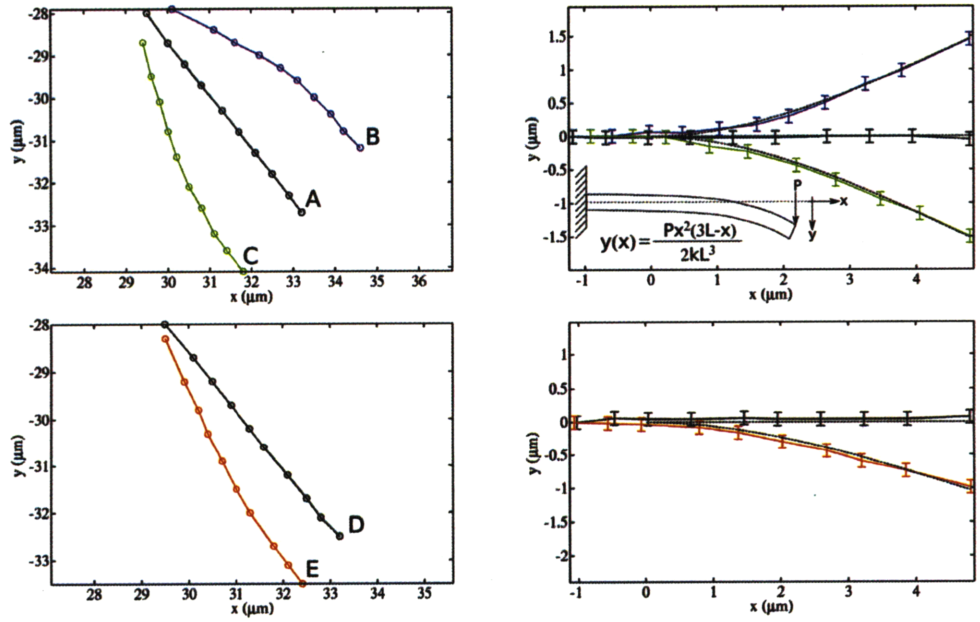

Figure 2-13: Shape analysis of bundle bending. Clockwise from top left: bundles skeletonized from the sweep cycle of the microscopy images from Figure 2-12 (A-C); beam shapes were rotated to align the initial (black) position with the x-axis, the maximum bent shapes (blue and green) were then fit with the cantilever beam cubic (dashed and inset); initial and bent shapes for the pull cycle fit using the same length parameter; bundle skeleton for the pull cycle (D-E). All errorbars are 99 nm (image pixel size).

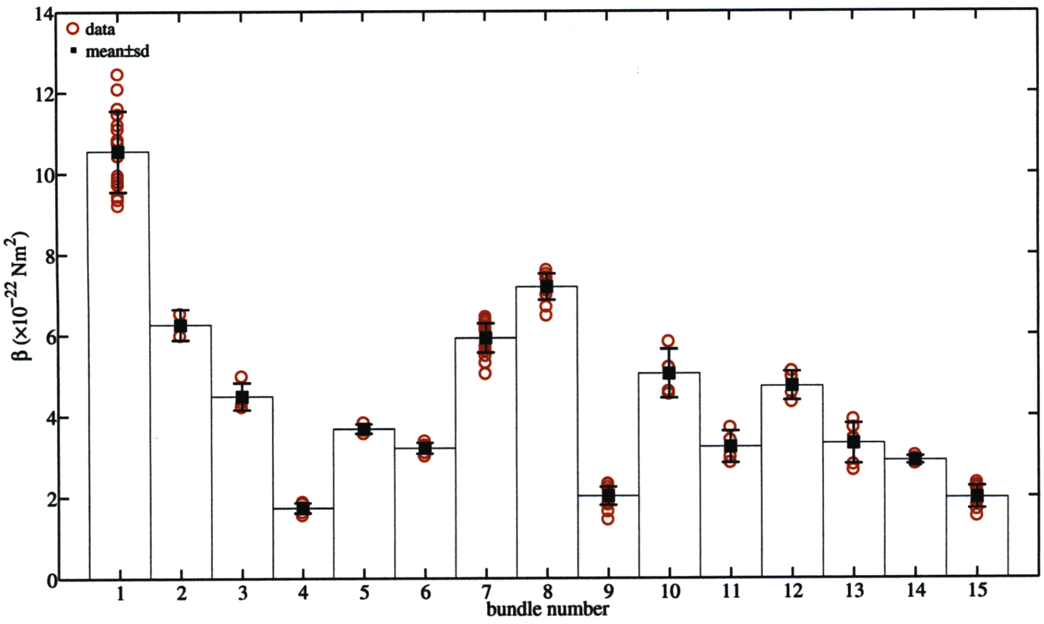

Figure 2-14: Bending rigidity β for all 15 dextran sulfate bundles. The circles represent the individual stiffness measurements; the errorbars the mean and standard deviation.

Hysteresis

The dextran sulfate bundles probed in the optical trap were formed over several hours. Over longer periods free bundles were found to show a significant reduction in filament spacing (from 8.6 to 6.8 nm) implying ongoing rearrangement of structure. In order to probe whether these bundles could rearrange their structure over shorter periods, the sweep-pull protocol was modified to include a pause halfway through the pull cycle. The entire sweep cycle, and the forward half of the pull cycle, act as a control and a difference in the magnitude or slope of the pull reverse force-displacement data would be indicative of a structural rearrangement. Several datasets (4 in total) showed a change in force but were disregarded due to trap nonlinearity during the pause or stage drift that moved the bead in the z-direction thereby changing the effective trap stiffness. Valid datasets (2 in total, not shown) showed no change in force or stiffness for pauses of up to 2 minutes. While this does not rule out hysteresis on a longer timescale, it does establish a lower bound.

2.7 Summary of Actin Properties

In this chapter, protocols were presented to purify monomeric actin from rabbit skeletal muscle and polymerize it into filaments. Electron and fluorescence microscopy revealed a filament shape and persistence length fully consistent with the literature. Depletion agents were then used to induce bundle formation both in free solution and seeded from acrosome fragments. Both bundle types revealed densely packed filaments with an interfilament spacing less than the major-axis diameter, suggestive of interdigitated structure.

Seeded bundle growth was measured by phase microscopy and the kinetics found to be in close agreement with the kinetics of single actin filaments from the literature. This is consistent with the notion that large molecular weight depletion agents serve only to bundle filaments and do not affecting the local monomer concentration. The bending rigidity of these bundles was measured by optical tweezers and found to be orders of magnitude higher than for individual filaments, suggestive of a fully crosslinked structure. This crosslinking derives predominantly from osmotic pressure (removal of depletion agent induces significant bundle softening) as well as weaker divalent cation binding.

The methods developed in this chapter will be extended to the study of scruin filaments and bundles in the following chapter.

Chapter 3

Scruin

This chapter investigates the effect of the scruin actin-binding protein on actin filament and bundle formation. Protocols are presented to: purify monomeric scruin; decorate actin filaments with scruin; characterize filament persistence length; induce bundle formation by scruin crosslinking; measure the kinetics of bundle formation; determine the role of scruin conformation; and measure bundle bending rigidity.

3.1 Monomers, Filaments and Ribbons

Scruin monomers were purified from the true discharge using protocols by Way (see Appendix Section B.1.4) [119, 120]. Acrosomes, induced by Ca^{2+}, were separated from the sperm body by low speed centrifugation, homogenized and demembranated in a mild detergent (Hecameg, CalBioChem), then crushed to separate the filaments. Actin was crystallized in 1 M Ca^{2+} and separated from scruin by size exclusion (AcA-44, Pharmacia) followed by ionic exchange (MonoQ, Pharmacia) and finally size exclusion (S12, Pharmacia). The peak fraction was typically around 2 mg/ml (16 μM) above which scruin tends to aggregate. Scruin was stored in p-buffer (10 mM Pipes pH 7.8, 3 mM NaN_3, 0.1 mM EGTA, 100 mM NaCl) and used within two months.

The purified scruin monomer is a complex of calmodulin (CaM, calcium binding protein, 17 kD) and two actin binding domains (spherical S and elongated E, 103 kD combined) with a total molecular weight of 120 kD. Dynamic light scattering revealed an hydrodynamic radius of 4.7 ± 0.1 nm (4 samples measured, independent of Ca^{2+} or EGTA, see Figure 3-1) which compares well with the x-ray scattering measurements (4.63 nm in EGTA and 4.83 nm in Ca^{2+}) [116].

Scruin decorated actin filaments were prepared by diluting 1 μM of pre-formed f-actin filaments to 30 nM and incubating them for 30 minutes in 1-2 μM scruin. This

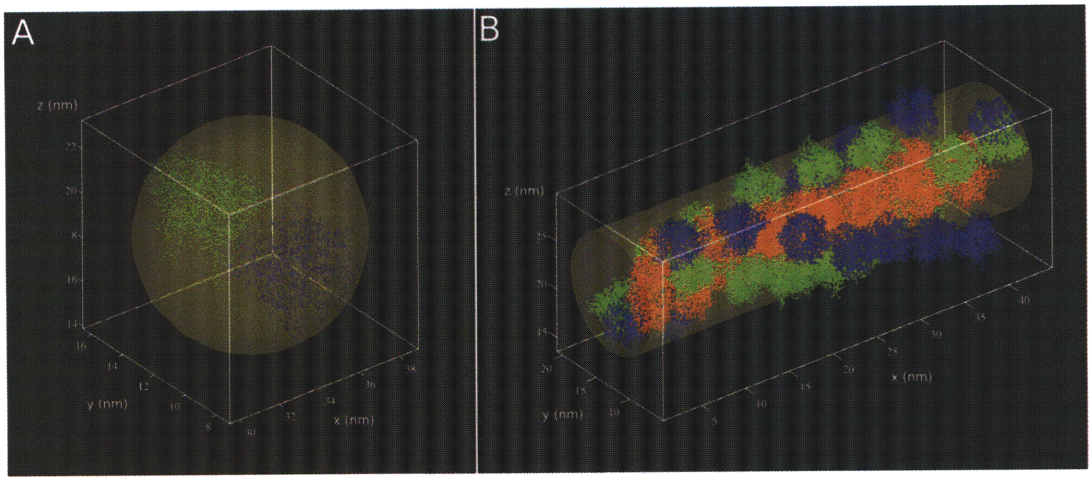

Figure 3-1: Molecular structure of scruin monomers (A) and filaments (B) with average radius shells shown in yellow. Based on tomogram reconstructions from Schmid *et al*, the averaged acrosome filament is partitioned into its actin core (red) and scruin sheath [92]. Individual scruin monomers are fit to the spherical (blue) and elongated domains (green). The monomer and filament diameters provide a reasonable approximation of the underlying structure.

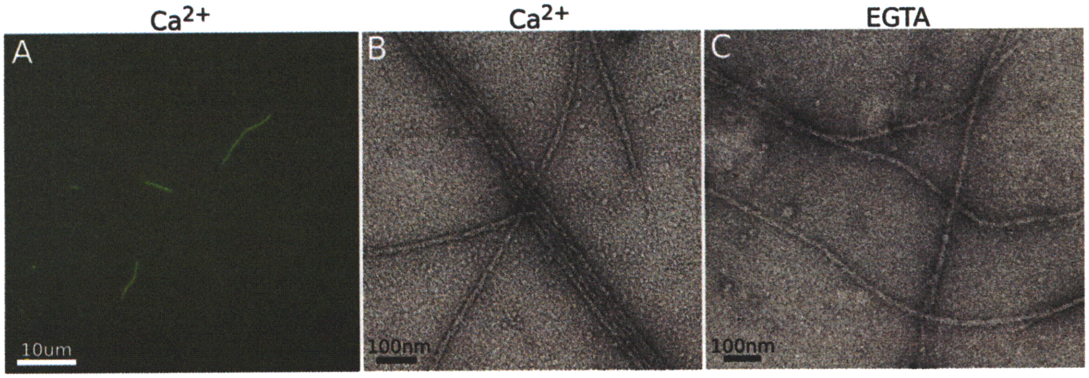

Figure 3-2: Scruin decorated actin filaments. Fluorescence microscopy of single filaments used for persistence length estimation (A). Negative stain electron microscopy showed little difference diameter or morphology between the Ca^{2+} (B) and EGTA conformations (C). Single filaments predominate when pre-formed actin filaments are incubated in excess scruin, while ribbons are common when actin and scruin are co-polymerized at higher and equimolar concentrations.

produced a majority of single filaments (see Figure 3-2). Multi-filament ribbons were prevalent when actin was co-polymerized in equimolar scruin at higher concentrations.

Electron microscopy of single filaments revealed an average radius r_{fs} of

$$r_{fs} = 6.8 \pm 1.1 \text{ nm}, \tag{3.1}$$

(5 filaments, 103 measurements). As for actin this represents the average of a helical structure (hence the high standard deviation). Direct measurements of multi-filament ribbons yielded the interfilament spacing and the major and minor axes. Filaments in the banded regions had an average spacing t_s of

$$t_s = 15.3 \pm 0.6 \text{ nm} \tag{3.2}$$

(4 ribbons, 57 measurements) and a minor-axis radius of 5.3 ± 0.3 nm (1 ribbon, 6 measurements). The width of the dense region divided by the number of filaments gave an average major-axis radius of 7.6 ± 0.1 nm (same ribbon, 9 measurements). For all filaments and ribbons studied, no statistical difference in diameter or spacing was observed between scruin's Ca^{2+} and EGTA conformations.

3.1.1 Persistence Length of Decorated Filaments

Several modifications to the actin persistence length protocol were required to gather acceptable data for the scruin decorated actin filaments. First, dextran sulfate was found to interfere with scruin decoration of actin (perhaps due to interference between scruin and the charged sulfate groups, see Supplemental Figure A-16) and so could not be used as a depletion agent. The alternative, uncharged dextran, caused no such problems but was ineffective at confining the filaments to the coverslip. Also, casein proved significantly less effective at preventing non-specific binding of filaments to the coverslip, resulting in a majority of stuck filaments.

To mitigate these problems, a direct confinement approach was developed (see Appendix Section B.2). First, low concentrations of pre-formed actin filaments were decorated by scruin: electron microscopy of these samples confirmed fully decorated single filaments (see Supplemental Figure A-13). A small volume (1-2 µl) was then sandwiched between two PEG coated coverslips – capillary action will pull the two coverslips together to within 1 µm separation – sufficient to prevent motion out of the focal plane. Dextran was added to slow the fluctuation speed and minimize blurring during timelapse imaging. Subsequent analysis of the thermal fluctuations

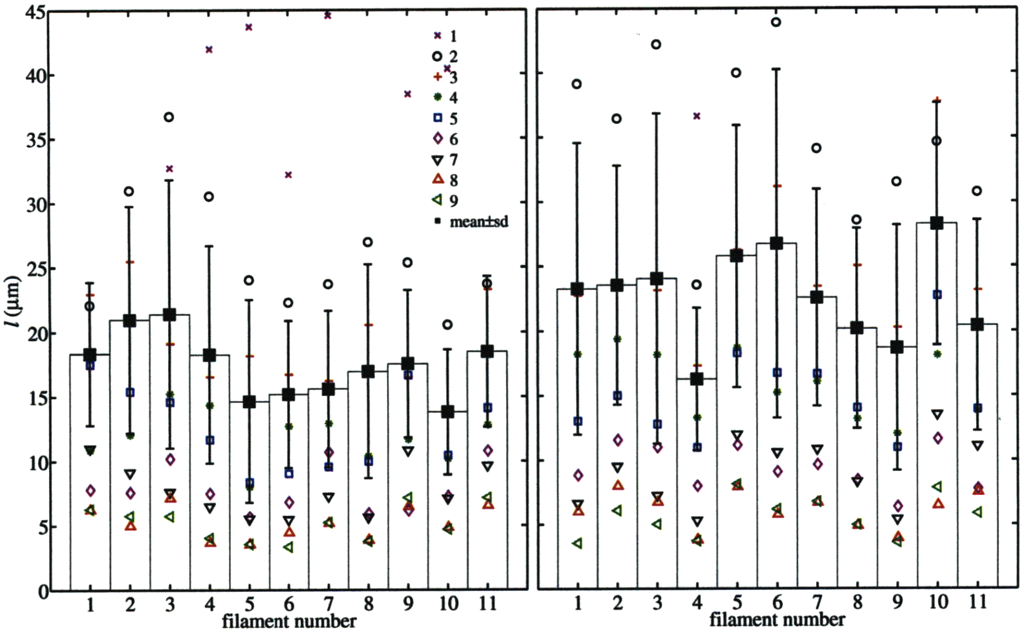

Figure 3-3: Mean persistence length for scruin Ca^{2+} and EGTA filaments. The average for scruin Ca^{2+} (left) was 17.4 μm, similar to actin's 17.9 μm and slightly lower than the 22.7 μm for EGTA (right).

was consistent with the actin filaments.

The persistence length in Ca^{2+} (11 filaments) was

$$\ell_{fs} = 17.4 \pm 2.5\ \mu\text{m}, \tag{3.3}$$

and in EGTA (also 11 filaments) it was

$$\ell_{fe} = 22.7 \pm 3.6\ \mu\text{m}, \tag{3.4}$$

where these are the averages of datasets presented in Figure 3-3. Compared to actin (17.9 ± 4.0 μm), Ca^{2+} filaments showed no statistical difference in persistence length while EGTA filaments were slightly stiffer (though all are within one standard deviation of the actin filament persistence length, see Supplemental Figure A-19).

The variation of modal estimates within each filament was greater than for actin, and the central modes on the log – log plots were not always well approximated by a line of slope -2. This may indicate that additional phenomena are contributing to the bending energy for these experiments.

Invalid datasets (58 in total) were disregarded based on the same metrics developed for the actin analysis: too few frames; poor convergence; or stuck filament. For the Ca^{2+} filaments, the cutoff length was set at 4.7 μm for Ca^{2+}, below which the persistence length distribution was 6.3 ± 2.9 μm (14 in total). Only a single EGTA filament of length 4.1 μm and persistence length 10.2 μm was disregarded. Additionally, several datasets (7 in total) displayed significantly higher persistence lengths, indicative of multi-filament ribbons. For Ca^{2+} (5 ribbons total) the average persistence length was 44.0 ± 4.3 μm and for EGTA only two ribbons were observed with persistence lengths of 39.5 μm and 51.6 μm.

In some cases, ribbons were brighter than their single filament neighbors, other times no intensity difference was seen or there were no other filaments in the field of view. Moreover, intensity is a poor metric for comparison due to the many potential sources of variation: reduced filament intensity due to focus drift, blurring or bleaching over the long imaging times; uneven or pulsing illumination from the light source; camera noise or image intensity saturation; or changes in background intensity between different regions of the coverslip. Consequently, multi-filament ribbons were disregarded based on their very high persistence length, rather than because of their intensity profile.

3.2 Kinetics of Scruin Bundle Formation

Scruin crosslinked bundles were imaged using similar protocols to those developed for dextran sulfate bundles, except no depletion agent was used – only scruin crosslinking could account for bundle formation. (As a negative control, bundle formation in the absence of scruin or depletion agents showed only divergent filaments, see Figure 2-7.) But formation of scruin bundles proved significantly more sensitive to the conditions compared to the depletion bundles. In particular, scruin bundles tended diverge at higher actin concentrations and they invariably bifurcated after several micrometers (see Figure 3-4). Divergence (fanning out of filaments, akin to the uncrosslinked example) was most evident at higher concentrations, presumably due to a mismatch between the fast growing actin and the slower scruin crosslinking. By contrast, bifurcation emerged as a near universal phenomenon, occurring at both low and high actin concentrations, though exacerbated by the latter. Consequently, analysis of growth rates at higher actin concentrations was less reliable and most measurements were restricted to the first few micrometers (much shorter than the depletion bundles which grew to tens of micrometers).

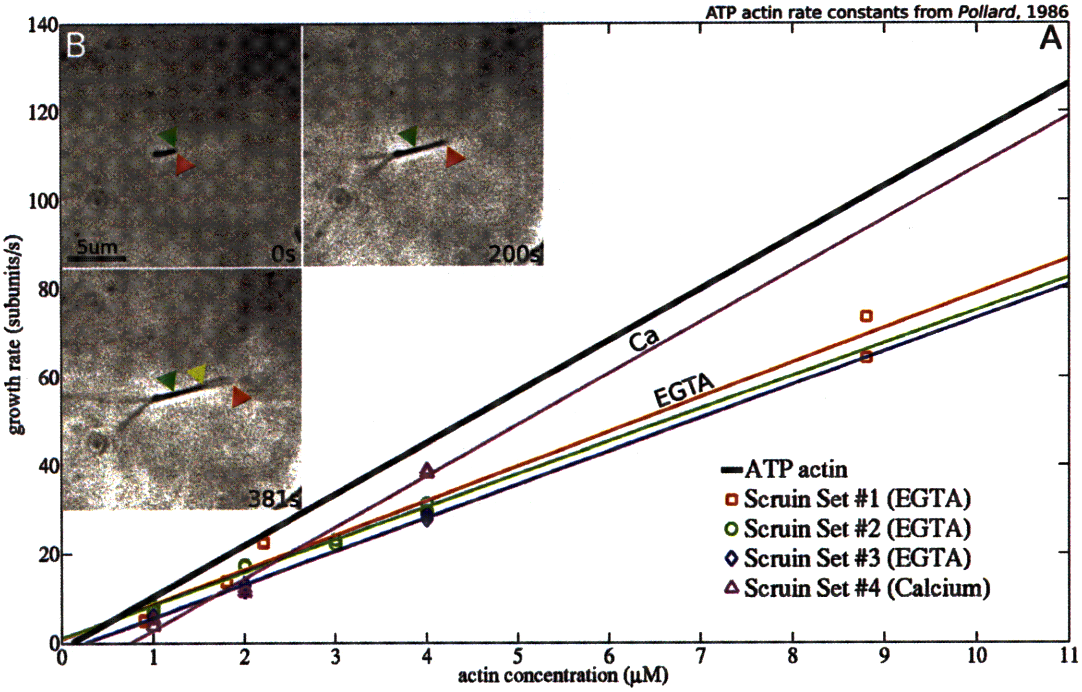

Figure 3-4: Kinetics of scruin bundle formation (A). Bundles formed in Ca^{2+} were comparable to actin filaments but with a higher off-rate (magenta), while in EGTA on-rates were significantly lower (red, blue and green). A timelapse of bundle growth (B) showed straight bundle formation over several micrometers prior to branching (yellow arrow).

Table 3.1: Scruin bundle rate constants. The on-rate for the Ca^{2+} bundle is consistent with the literature but the off-rate is significantly higher. All EGTA bundles have significantly lower on-rates compared to Ca^{2+}. Phalloidin shows little effect on either rate constant. Literature rate constants are based on Pollard *et al* [83].

Experiment		k_{on} (1/μMs)	k_{off} (1/s)
Pollard	phalloidin-free	11.6	1.3
Ca^{2+}	phalloidin	11.6	8.8
EGTA	phalloidin	7.5	1.9
EGTA	phalloidin-free	7.8	-0.9
EGTA	phalloidin-free	7.4	-1.1

Kinetics were analyzed in the same fashion as for depletion bundles: four datasets were gathered to determine the effect of phalloidin, Ca^{2+} and EGTA (see Figure 3-4 and Table 3.1). All experiments were conducted in excess scruin to promote complete decoration and crosslinking. Kinetics in Ca^{2+} were found to be faster than EGTA, consistent with the depletion findings, though below 2 μM actin this was reversed and EGTA became faster than Ca^{2+}. Phalloidin showed little effect on either rate constant. Qualitatively, bundle formation improved at lower actin concentrations (bundles grew longer before diverging or bifurcating) implying that slowing the growth rate builds better bundles.

To confirm this, bundles were grown at 4°C and 22°C and their respective length and structure compared by electron microscopy. The length of bundles formed over 45 minutes at 4°C was 2.3 ± 0.6 μm (19 bundles measured) and 5.3 ± 0.9 μm at 22°C (17 bundles measured). The average seed length L_t was 790 ± 253 nm (11 seeds measured) which, when subtracted from the bundle lengths, gave nominal growth rates (for both ends combined) of 2 μm/hr at 4°C and 6 μm/hr at 22°C. Reduction in temperature therefore caused a three-fold reduction in growth rate, which can be applied to the 22 °C kinetics to determine the effective growth rate over a range of actin concentrations. Importantly, structure was significantly improved at 4°C (see Supplemental Figure A-14). Though it is not possible to further reduce the temperature (the proteins would freeze), even slower growth rates can be achieved by reducing the actin concentration.

3.3 Optimization of Bundle Structure

Several key factors were identified as critical to scruin bundle formation: actin and scruin concentrations; seed type and scruin conformation; seed concentration; and ionic strength. Each of these was investigated in order to determine the optimal conditions for bundle growth.

Ionic Strength

Bundle formation during the kinetics experiments was typically done at an ionic strength of around 150 mM, the default for a sample consisting primarily of a-buffer (100 mM NaCl) and f-buffer (50 mM KCl). To determine the optimal range, bundle formation was observed in samples where the ionic strength was raised from 76 mM to 500 mM (see Supplemental Figure A-11). Optimal conditions were found to occur around 100-200 mM, consistent with the default conditions. Above 200 mM, bundle

Table 3.2: Bundle reconstitution matrix. The combination of seed (TD, FD or coil) and scruin conformation (Ca^{2+} or EGTA) can be used to reconstitute all acrosome conformations.

equivalent structure	seed template	scruin conformation
true discharge	TD	Ca^{2+}
false discharge	FD	EGTA
coil	coil	EGTA
nascent acrosome	TD	EGTA
none	FD	Ca^{2+}
none	coil	Ca^{2+}

length decreased significantly and at 500 mM virtually no bundles were formed (only actin filaments were seen).

The effect of increasing the ionic strength on pre-formed bundles was not examined. The literature reports that native TD and FD are resistant to changes in pH, low or high salt, high Ca^{2+} or Mg^{2+}, high EGTA, and high ATP; though they did begin to dissociate in 500 mM divalent salts [110].

Seed Type and Scruin Conformation

During spermatogenesis, the acrosome is seeded at the anterior vesicle and grows down the nuclear channel in a straight conformation (but in the absence of Ca^{2+}). At the base of the cell it is bent and twisted into the coil where it remains in a stable state until it is converted to either the true or the false discharge. Each 700 nm arm of the coil is twisted by approximately 60° representing an overtwist of 0.23° per scruin monomer. The straight and irreversible TD arises from a conformation change in scruin upon binding Ca^{2+}. In contrast, the FD undergoes a -90° change of twist per arm compared to the coil but remains in a Ca^{2+}-free state, which arises from a realignment of scruin-scruin crosslinks as opposed to a conformation change. Moreover, the different scruin conformations are implicated in the difference in bending rigidity between the TD and FD.

The four native bundle states and their corresponding scruin conformations are: TD-EGTA, TD-Ca^{2+}, coil-EGTA and FD-EGTA (see Table 3.2). Two additional states are: coil-Ca^{2+} and FD-Ca^{2+}, though these do not occur naturally. For the reconstitution studies: TD-Ca^{2+} and FD-EGTA– proxies for the true and false discharge, respectively – are the most relevant. Electron microscopy of bundles formed under these conditions (see Supplemental Figure A-12) showed little difference in bundle structure, though in EGTA large amounts of unseeded filaments were observed (consistent with the mechanism of actin polymerization: EGTA facilitates the exchange of Ca^{2+} with Mg^{2+} thereby promoting spontaneous nucleation and polymerization of filaments). No twist was evident for any bundle, implying that twisting of the coil and FD does not occur spontaneously, rather it likely arises from an external mechanical force.

Seed Concentration

Significant variations in bundle structure were observed depending on the final bundle length. Shorter bundles tended to be tapered while longer ones diverged or bifurcated after several micrometers. In order to properly compare different conditions, a final bundle length of 2-5 µm was desirable. Two factors were adjusted to achieve this: seed ratio and polymerization time. The seed ratio is defined as

$$\xi = \frac{l_b}{l_t}, \tag{3.5}$$

where l_b is the final bundle length and l_t is the average seed length. Given an input actin concentration c_a and a seed concentration c_t

$$\frac{l_b}{l_t} = \frac{c_a}{c_t}, \tag{3.6}$$

which assumes the same number of filaments in the seed and the bundle, and that all the bulk g-actin is recruited to the bundles. This equation can be explained by considering that the seed concentration is the same as the concentration of actin within that seed, and that this concentration gives rise to the average seed length – adding twice the concentration of actin as seeds forms bundles that are twice as long as the seed length. For example, given 100 nM of 750 nm long seeds with 400 nM actin, the bundles will be 3 µm long on average. Shorter bundles can be grown by decreasing the polymerization time. Typically, structural experiments were allowed to polymerize overnight while optical trap bundles were grown over four hours (to reduce sticking to the coverslip).

Actin Concentration

Bundles were formed over a range of actin concentrations (50-1000 nM) and their structure examined by electron microscopy (see Figure 3-5). Best results were observed for 200-400 nM actin (with $\xi > 4$) which formed long and highly convergent bundles off the barbed end of the seed. Although these bundles did not diffract strongly enough for the FFT analysis, direct measurement of interfilament spacing showed 15.1 ± 1.3 nm (one bundle, 16 measurements) consistent with the ribbon spacing of 15.3 ± 0.6 nm. All bundles were formed in excess scruin (typically 1-2 μM, a 5-fold excess) though little improvement was seen for higher scruin concentrations. Rarely was decent structure observed at the pointed end, whose on-rate is significantly slower according to the literature. This suggests that despite significantly slower kinetics, improved bundle structure is contingent on seeding from the barbed end.

At low actin concentrations and low seed factors (100-200 nM actin, $\xi < 3$) short bundles with nice crystalline structure were formed. Longer bundles, though tightly packed, did not show the same crystalline structure and were typically less dense. This is likely an experimental limitation – *in vivo* the acrosome forms very slowly and likely in very low actin and scruin concentrations – perhaps due to impurities in the purified g-actin stock.

For all bundle types, bifurcation tended to occur after several micrometers, regardless of initial actin concentration or seed factor. This may highlight a fundamental limit to this reconstitution technique. *In vivo* the acrosome barbed end is associated with the anterior vesicle template. Incoming actin monomers are therefore bounded on one side by the template and the other by the barbed end of the growing acrosome. This minimizes the separation between the seeding location and the bundle end. In contrast, bundles seeded in free solution see monomers recruited at progressively greater distances from the seed, resulting in an increased probability of imperfections and dislocations, eventually giving rise to bifurcations.

Scruin Concentration

So far, all bundles have been formed in excess scruin to promote complete decoration and full crosslinking. It is also of interest to form bundles in sub-stoichiometric scruin to probe the mechanics of partially crosslinked bundles. Experiments were conducted under the following conditions: low actin (250-500 nM), low scruin (0-500 nM) and Ca^{2+} or EGTA (see Supplemental Figure A-15). Several bundle types emerged: completely uncrosslinked bundles (no scruin); very short bundles (sub-stoichiometric scruin); or very long bundles (equimolar or above scruin). Very short bundles occurred for 500 nM actin in Ca^{2+} or 250 nM actin in EGTA, both at less than 50 nM scruin. At low actin concentrations bundles form roughly twice as fast in

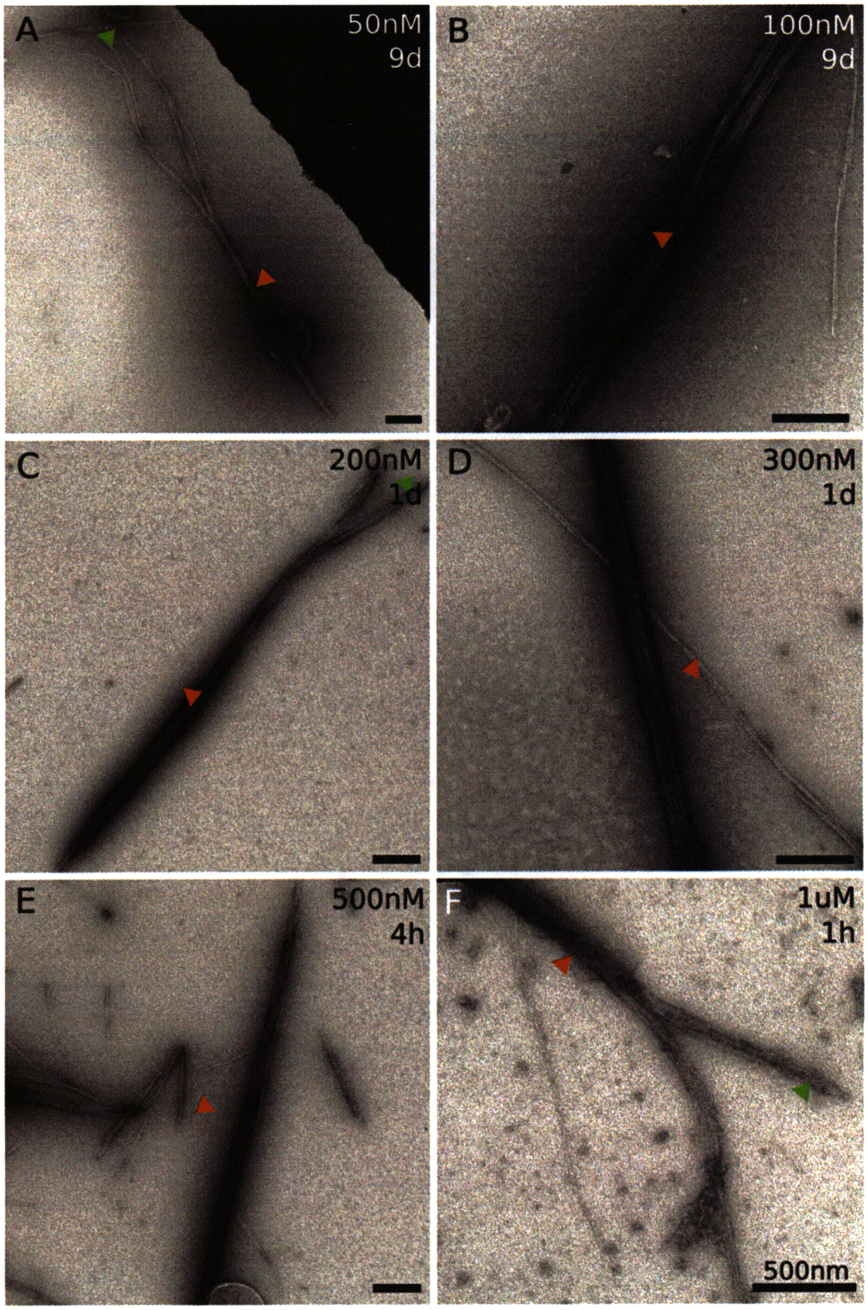

Figure 3-5: Optimal actin concentration. Bundles formed over multiple days at very low actin concentrations (A-B) showed poor structure. Intermediate concentrations (C-D) gave rise to optimal conditions, producing long straight bundles with good structure (see also Figure 3-6). Higher concentrations over shorter periods produced comparable bundles of length suitable for manipulation by optical tweezers (E). Above 500 nM branched bundles predominate (F). Scale bar: 500 nm.

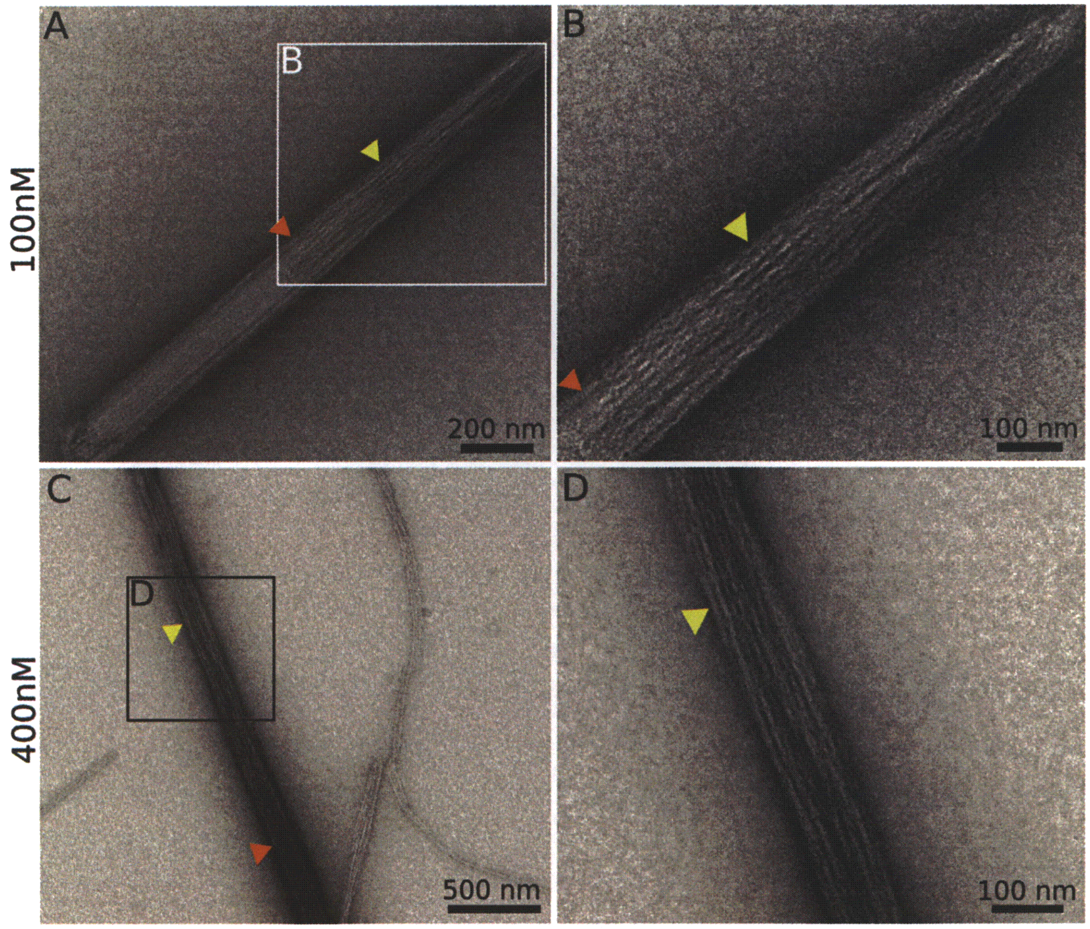

Figure 3-6: Optimal bundle structure. Short bundles formed over long periods in low actin (A-B) showed TD-like crystalline structure (yellow arrow). Longer bundles formed at intermediate concentrations displayed long parallel filaments but minimal crystal structure. Red arrows show the approximate seed-bundle interface.

EGTA as in Ca^{2+}, so bundles grown at 500 nM actin in Ca^{2+} tend to be qualitatively consistent with those formed at 250 mM but in EGTA. The paucity of bundle suggests very slow kinetics, indicating that the rate constants are dependent on the scruin concentration. Longer bundles (though not partially crosslinked) were achieved under two conditions: 500 nM actin, 250 nM scruin and EGTA (completely uncrosslinked bundles); or equimolar scruin (fully crosslinked bundles).

Despite a significant number of experiments, no conditions were found under which suitably long and partially cross-linked bundles could be formed, which may indicate a fundamental limitation for scruin-actin bundle formation.

Optimal Conditions

Optimal conditions for bundle formation were found to require: low actin concentrations; excess scruin; low temperature; long incubation times; moderate seed ratios; and moderate ionic strength. Less critical was: seed type (TD or FD) or scruin conformation (Ca^{2+} or EGTA). Variation of one or more of these parameters typically results in suboptimal bundles, such as those presented in Supplemental Figure A-16. These generally suffered from: divergence (fanning of bundle due to insufficient crosslinking), bifurcation (branching due to imperfections in the replication mechanism); or tapering (convergent bundles thinner than the seed). Divergence and forking were caused and compounded by: high actin concentrations (rapid polymerization); low scruin concentrations (inability to crosslink); or long bundles (the probability of bifurcation increases with bundle length). Tapering arose from: short polymerization times (bundle too short); high seed concentrations (too little actin per bundle); low actin concentrations (insufficient protein to form a dense bundle); or old actin (lower effective actin concentration).

These imperfections can provide insight into the underlying mechanism of bundle formation. Consider bundles formed in 400 nM actin and 2 μM scruin: overnight incubation yielded long parallel bundles with decent structure, yet polymerization over just one hour formed short tapered bundles. This suggests that initial bundle formation (during which crystalline structure is often observed) forms a triangular leading edge while subsequent growth proceeds with a flat front (leading to long parallel filaments with polycrystalline structure). Consider also bifurcation: bundles fork after several micrometers seemingly independent of the formation conditions, with each branch typically maintaining a crosslinked structure past the bifurcation point. This highlights the importance of the confined geometry in which the native acrosome is formed and that in order to mitigate the bifurcation problems, a *Limulus*-like assembly mechanism should be explored.

3.4 Bending Rigidity of Scruin Bundles

The optical trap bending protocol developed for the depletion bundles was readily extended to the measurement of scruin bundles, though with several key alterations. First, casein proved again to be a poor blocking agent against nonspecific scruin binding, so the majority of bundles tended to stick to the coverslip. To mitigate this, bundles were formed over shorter periods (4 hours as opposed to overnight)

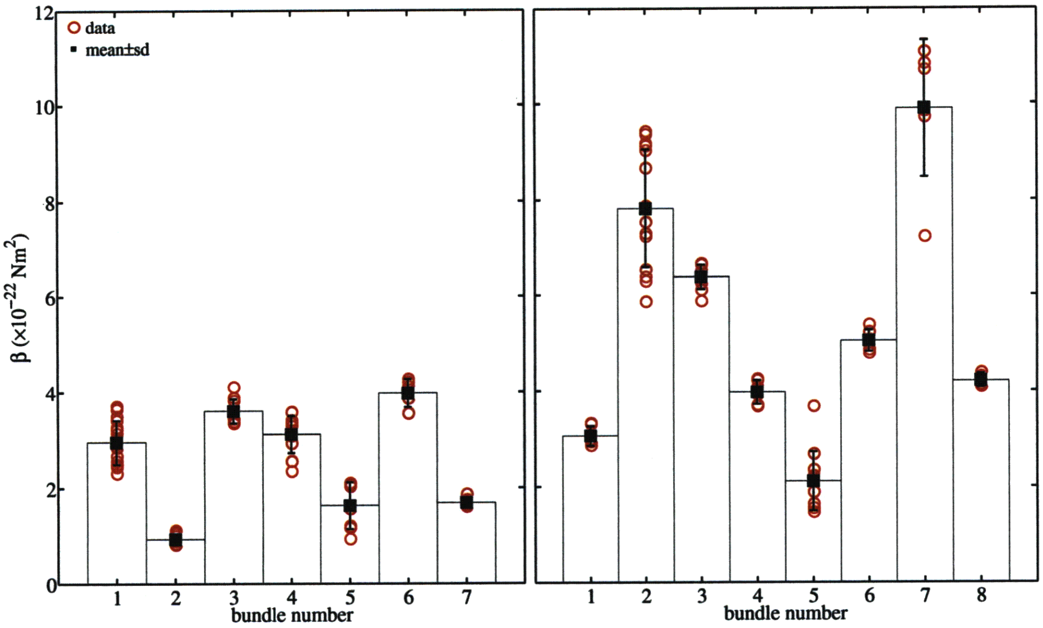

Figure 3-7: Bending rigidity of scruin bundles in Ca^{2+} and EGTA. All bundles were formed in 2 μM scruin. Bundles grown in 500 nM actin and Ca^{2+} (left) had an average bending rigidity of $2.6 \pm 1.2 \times 10^{-22}$ Nm^2. Scruin bundles in 250-500 nM actin and EGTA had a higher bending rigidity of $5.3 \pm 2.6 \times 10^{-22}$ Nm^2 (right), though still within one standard deviation of the Ca^{2+} bundle rigidity.

and at slightly higher actin concentrations (250-500 nM as opposed to 200-400 nM), producing long parallel bundles with comparable structure to those formed over longer periods and at lower actin concentrations (see Figure 3-5). Even under these modified conditions, a great many bundles still stuck to the coverslip, though these were easily identified during the sweep-pull cycles due to their very high stiffness (and the fact that they didn't move).

The bending rigidity for all scruin bundles (15 in total, 7 in Ca^{2+} and 8 in EGTA) is shown in Figure 3-7. For scruin Ca^{2+} bundles the average rigidity was

$$\beta_s = 2.6 \pm 1.2 \times 10^{-22}\ \mathrm{Nm}^2. \tag{3.7}$$

All seven Ca^{2+} bundles were grown over fours hours in 500 nM actin and 2 μM scruin; all were relatively short with an average length of 2.9 ± 0.7 μm; and all had beads bound to the end of the bundle (see Supplemental Figure A-17). For EGTA bundles

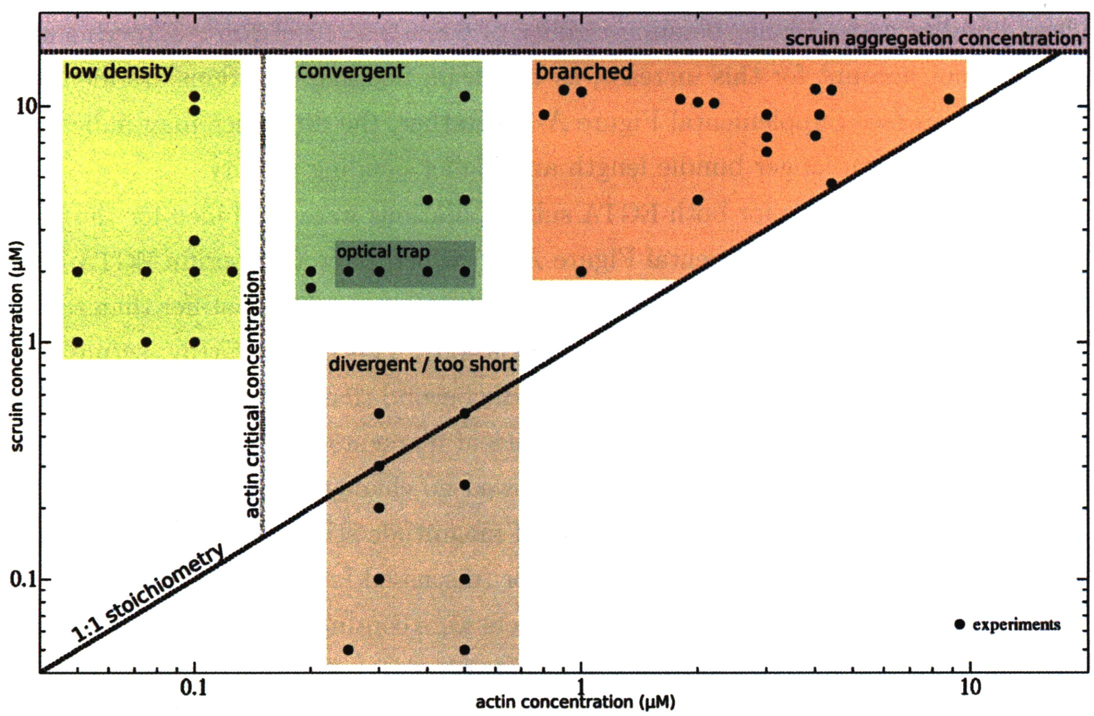

Figure 3-8: Concentration phase space for actin scruin bundle formation. Scruin crosslinked bundles were significantly more difficult to form than depletion bundles and require a precise combination of conditions for optimal structure. Low actin concentrations, moderate ionic strength, low temperatures and excess scruin were all critical. Even under these conditions bundles bifurcated after several micrometers, suggesting a fundamental limit to free-end replication.

the average bending rigidity was

$$\beta_e = 5.3 \pm 2.6 \times 10^{-22}\ \mathrm{Nm}^2, \tag{3.8}$$

though this represents the average of two slightly different sub-populations: longer bundles with beads bound partway; and shorter bundles with beads bound at their ends. This arises from the difference in kinetics between Ca^{2+} and EGTA (EGTA bundles form roughly twice as fast as those in Ca^{2+} at low actin concentrations). The first sub-population of EGTA bundles were formed in 250 nM actin and 2 μM scruin and showed an average rigidity of $3.8 \pm 1.2 \times 10^{-22}$ Nm^2. Their mean length was 3.9 ± 0.9 μm and all beads were bound to bundle ends – these bundles were qualitatively and quantitatively comparable to the Ca^{2+} bundles above. The second sub-population of EGTA bundles were formed in 250-500 nM actin and 2 μM scruin but were longer than the Ca^{2+} bundles with the bead bound partway along the bundle.

These bundles had a higher bending rigidity of $6.8 \pm 2.9 \times 10^{-22}$ Nm^2. Experimental setup cannot account for this increase, as the beam bending equations are identical for both cases (see Supplemental Figure A-1). Rather, the difference may indicate a correlation between longer bundle length and higher bending rigidity.

Regardless, statistics for both EGTA sub-populations were combined for the bundle comparisons (see Supplemental Figure A-19) which show that scruin EGTA bundles were comparable to dextran sulfate bundles (both were slightly stiffer than scruin Ca^{2+}, though all were within one standard deviation). This is noteworthy: scruin confers no additional bending rigidity to the bundle beyond that of an actin-only bundle, but serves instead to resist shear between adjacent filaments. This is also fully consistent with the single filament data, which showed no change in persistence length by scruin decoration. All bundles were orders of magnitude stiffer than their respective filaments, suggestive of fully coupled behavior (discussed further in Chapter 4).

As with the depletion bundles, valid datasets were contingent on several criteria: a linear force-displacement profile, consistent between sweep and pull cycles; a stiffness in range for the optical trap (typically 5-100 pN/μm); and a shape consistent with beam bending theory. Bundles were disregarded (81 in total) due to: non-specific binding to coverslip; nonlinear force-displacement curves; or incorrect beam shape.

3.5 Summary of Scruin Properties

This chapter presented protocols to purify monomeric scruin from *Limulus* and to decorate actin filaments by incubating nanomolar concentrations of pre-formed f-actin in excess scruin. Their persistence length was measured using the same timelapse microscopy techniques developed for actin and found to be comparable to actin for both Ca^{2+} and EGTA scruin conformation. This implies that scruin confers no additional mechanical stiffness by decorating the actin filament. Kinetics of bundle formation were found to be comparable to the literature for Ca^{2+} bundles but slower for EGTA, for actin concentrations above 2 μM. Below this an inversion occurred and EGTA bundles formed twice as fast as Ca^{2+} bundles. For both scruin and depletion bundles, on-rates in Ca^{2+} were consistently higher than in EGTA. Preliminary experiments were also conducted in sub-stoichiometric scruin to probe the formation of partially crosslinked bundles. Determination of optimal conditions was problematic as the system became highly sensitive to both actin and scruin concentrations, a potential indication of the limitations of scruin-actin bundle formation.

A phase space summarizing scruin bundle formation is depicted in Figure 3-8.

Above equimolar stoichiometry, scruin bundles fall into three categories: low density, convergent or branched. Convergent bundles formed in 200-400 nM actin with overnight incubation at low temperature resulted in long parallel bundles of fully decorated actin filaments. To mitigate non-specific binding issues, optical trap bundles were formed at 250-500 nM actin over 4 hours (also at low temperature) and their bending rigidity suggested fully coupled bending. Low density tapered bundles occurred at very low actin concentrations (below 100 nM actin) though this is likely an experimental limitation arising from impurities in the g-actin stock. Above 500 nM actin, bundles branched rapidly as a result of mismatched kinetics between rapid actin polymerization and slower scruin crosslinking.

In the following chapter, the mechanical properties of scruin bundles are related to the material properties of decorated single filaments by simple mechanical models. Scruin filaments and bundles are compared to actin-only filaments and bundles studied in Chapter 2 in order to elucidate the role of scruin in actin bundle formation.

Chapter 4

Bundle Mechanics

This chapter summarizes the material properties of bundles crosslinked by either dextran sulfate or by the scruin actin-binding protein. Simple models are used to relate bundle rigidity to the mechanics of individual filaments in order to elucidate the role of scruin in the crosslinking of actin bundles.

4.1 Material Properties of Filaments and Bundles

In Chapter 2 the material properties of phalloidin actin filaments were measured, revealing an average radius r_f (4 filaments measured) and persistence length ℓ_f (17 filaments measured)

$$r_f = 3.2 \pm 0.7\ \text{nm}, \tag{4.1}$$

$$\ell_f = 17.9 \pm 4.0\ \mu\text{m}, \tag{4.2}$$

which leads to a moment of area I_f of

$$I_f = \frac{\pi r_f^4}{4} \tag{4.3}$$

$$= 82.4\ \text{nm}^4, \tag{4.4}$$

and a bending rigidity β_f and elastic modulus E_f

$$\beta_f = 7.3 \pm 1.6 \times 10^{-26}\ \text{Nm}^2, \tag{4.5}$$

$$E_f = 874 \pm 196\ \text{MPa}. \tag{4.6}$$

Here $E_f = \frac{\beta_f}{I_f}$ is the equivalent elastic modulus of an isotropic rod and β_f is calculated from the persistence length by $\beta_f = \ell_f K_b T$ (from Equation 1.4).

The average radius R_t (93 seeds measured, independent of TD, FD or sonication conditions) and interfilament spacing t_t (5 seeds measured) for the true or false discharge seeds was

$$R_t = 53.7 \pm 8.0 \text{ nm}, \tag{4.7}$$

$$t_t = 14.9 \pm 0.4 \text{ nm}. \tag{4.8}$$

For seeded actin dextran sulfate bundles, the interfilament spacing t_x (for 8 bundles) was

$$t_x = 8.6 \pm 0.6 \text{ nm}, \tag{4.9}$$

and the bundle radius was approximated by

$$R_x = R_t \frac{\bar{t_x}}{\bar{t_t}} \tag{4.10}$$

$$= 30.9 \pm 4.6 \text{ nm}, \tag{4.11}$$

which despite different packing between the seed and the bundle proved a decent estimate (see Supplemental Figure A-18). The standard deviation for R_x was solely based on R_t and did not consider variations in seed or bundle filament spacings. The corresponding bending rigidity β_x and elastic modulus E_x were

$$\beta_x = 4.3 \pm 2.1 \times 10^{-22} \text{ Nm}^2, \tag{4.12}$$

$$E_x = 604 \pm 298 \text{ MPa}, \tag{4.13}$$

comparable to actin filaments in elastic modulus but several orders of magnitude higher in bending rigidity.

In Chapter 3, the radius r_{fs} (averaged over 5 filaments, independent of Ca^{2+} or EGTA) and persistence length ℓ_{fs} (11 filaments measured) for scruin Ca^{2+} decorated phalloidin actin filaments were found to be

$$r_{fs} = 6.8 \pm 1.1 \text{ nm}, \tag{4.14}$$

$$\ell_{fs} = 17.4 \pm 2.5 \ \mu\text{m}, \tag{4.15}$$

so the bending rigidity β_{fs} and filament elastic modulus E_{fs} are

$$\beta_{fs} = 7.1 \pm 1.0 \times 10^{-26}\ \mathrm{Nm}^2, \tag{4.16}$$

$$E_{fs} = 42 \pm 6\ \mathrm{MPa}. \tag{4.17}$$

Here the bending rigidity is comparable to actin filaments but the elastic modulus is significantly lower.

For actin scruin Ca^{2+} bundles the interfilament spacing t_s (5 ribbons measured) and corresponding bundle radius R_s were

$$t_s = 15.3 \pm 0.6\ \mathrm{nm}, \tag{4.18}$$

$$R_s = R_t \frac{t_s}{t_t} \tag{4.19}$$

$$= 55.3 \pm 8.3\ \mathrm{nm}. \tag{4.20}$$

The bundle rigidity β_s and modulus E_s were

$$\beta_s = 2.6 \pm 1.2 \times 10^{-22}\ \mathrm{Nm}^2, \tag{4.21}$$

$$E_s = 35 \pm 16\ \mathrm{MPa}. \tag{4.22}$$

Here the bending rigidity is orders of magnitude higher than for a single filament and comparable to that of an actin-only bundle, but the elastic modulus is significantly lower than for actin (though comparable to that of a single scruin Ca^{2+} filament).

Compare these results to the TD hydrodynamic flow measurements

$$\beta_{td} = 84 \pm 29 \times 10^{-22}\ \mathrm{Nm}^2, \tag{4.23}$$

$$E_{td} = 2500 \pm 720\ \mathrm{MPa}, \tag{4.24}$$

and the magnetic trap measurements

$$\beta_{td} = 47 \pm 12 \times 10^{-22}\ \mathrm{Nm}^2, \tag{4.25}$$

$$E_{td} = 1340 \pm 340\ \mathrm{MPa}, \tag{4.26}$$

both from Shin [97]. Despite the two-fold difference in TD rigidity between the two experiments, these suggest that the true discharge is at least an order of magnitude stiffer than the equivalent reconstituted bundle.

For scruin EGTA filaments there was no statistical difference in filament radius

Table 4.1: Summary of structural and mechanical parameters. Key: †in Ca^{2+} or EGTA; $^{\mathrm{t}}$TD; $^{\mathrm{f}}$FD; ‡TD or FD; §for 3.2 nm actin filament radius; all actin properties are for phalloidin labeled filaments.

Param.	Value	Literature	Units	Description
				radius of
r_f	3.2 ± 0.7	2.4-4.5	nm	actin filament
r_{fs}	6.8 ± 1.1	–	nm	actin scruin filament†
R_t	53.7 ± 8.0	24-68	nm	seed‡
				interfilament spacing of
t_t	14.9 ± 0.4	14.4-14.7	nm	seed‡
t_x	8.6 ± 0.6	–	nm	dextran sulfate bundle
t_s	15.3 ± 0.6	–	nm	scruin bundle†
				number of filaments in
N_t	54 ± 16	15-85	–	seed‡
				persistence length of
ℓ_f	17.9 ± 4.0	14.7-19	µm	actin filament
ℓ_{fs}	17.4 ± 2.5	–	µm	actin scruin Ca^{2+} filament
ℓ_{fe}	22.7 ± 3.6	–	µm	actin scruin EGTA filament
				bending rigidity of
β_f	7.3 ± 1.6	6.8-7.7	$\times 10^{-26}$ Nm^2	actin filament
β_{fs}	7.1 ± 1.0	–	$\times 10^{-26}$ Nm^2	actin scruin Ca^{2+} filament
β_{fe}	9.2 ± 1.5	–	$\times 10^{-26}$ Nm^2	actin scruin EGTA filament
β_x	4.3 ± 2.1	–	$\times 10^{-22}$ Nm^2	dextran sulfate bundle
β_s	2.6 ± 1.2	47-84$^{\mathrm{t}}$	$\times 10^{-22}$ Nm^2	scruin Ca^{2+} bundle
β_e	5.3 ± 2.6	23$^{\mathrm{f}}$	$\times 10^{-22}$ Nm^2	scruin EGTA bundle
				elastic modulus of
E_f	886 ± 199	834-899	MPa	actin filament§
E_{fs}	42 ± 6	–	MPa	actin scruin Ca^{2+} filament
E_{fe}	55 ± 9	–	MPa	actin scruin EGTA filament
E_x	604 ± 298	–	MPa	dextran sulfate bundle
E_s	35 ± 16	1340-2500$^{\mathrm{t}}$	MPa	scruin Ca^{2+} bundle
E_e	73 ± 36	198$^{\mathrm{f}}$	MPa	scruin EGTA bundle

compared to the Ca^{2+} filaments, but the persistence length ℓ_{fe} (11 filaments measured) was slightly higher at

$$\ell_{fe} = 22.7 \pm 3.6\ \mu\mathrm{m}, \tag{4.27}$$

leading to a bending rigidity β_{fe} and elastic modulus E_{fe} of

$$\beta_{fe} = 9.2 \pm 1.5 \times 10^{-26}\ \mathrm{Nm}^2, \tag{4.28}$$
$$E_{fe} = 55 \pm 9\ \mathrm{MPa}, \tag{4.29}$$

both of which are comparable to scruin Ca^{2+} filaments.

For actin scruin EGTA bundles

$$\beta_e = 5.3 \pm 2.6 \times 10^{-22}\ \mathrm{Nm}^2, \tag{4.30}$$
$$E_e = 73 \pm 36\ \mathrm{MPa}, \tag{4.31}$$

which are within one standard deviation of the scruin Ca^{2+} bundles.

Compare these EGTA bundles to the FD hydrodynamic measurements

$$\beta_{fd} = 23 \pm 2.5 \times 10^{-22}\ \mathrm{Nm}^2, \tag{4.32}$$
$$E_{fd} = 198 \pm 22\ \mathrm{MPa}, \tag{4.33}$$

from Tam [105]. Here, the equivalent reconstituted bundles are only half as stiff as the false discharge.

Table 4.1 presents a summary of the material properties, allowing a direct comparison of filament and bundle rigidities. It reveals that scruin single filaments have roughly the same rigidity as actin single filaments. Bundles formed from each of the three filament types all had similar rigidities and all were orders of magnitude stiffer than their individual filaments. These results indicate that scruin contributes little mechanical stiffness to either the decorated filament or the crosslinked bundle, rather it serves primarily to crosslink these filaments and resist shear during bending. By comparison, the TD and FD are significantly stiffer than any of the reconstituted bundles, suggesting an additional regime where scruin does contribute to the mechanical stiffness, likely as a consequence of the crystalline packing.

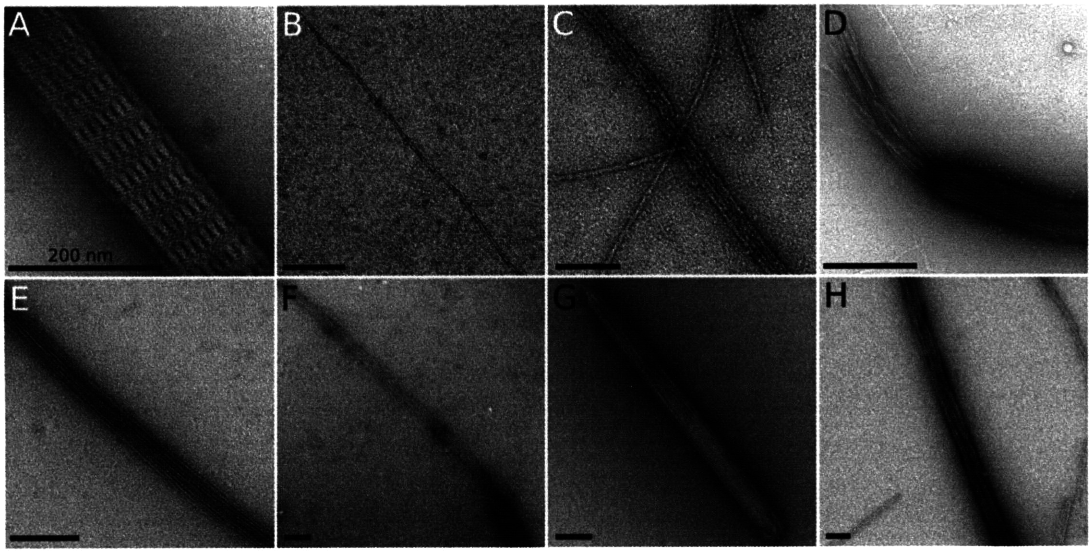

Figure 4-1: Electron microscopy of filaments, ribbons and bundles. The crystalline structure of true discharge seed displays a characteristic banded pattern (A). Actin filaments were imaged to determine their average diameter (B). Actin scruin ribbons formed in the absence of any seed showed identical structure to the TD, indicating a natural inclination towards this type of packing (C). Seeded polymerization of actin filaments (here formed off the FD) in the absence of any crosslinker formed divergent bundles (D). Free actin dextran sulfate bundles displayed polycrystalline square packing (E) consistent with seeded bundles formed under comparable conditions (F). Short actin scruin Ca^{2+} bundles nucleated off true discharge seeds retained some of the seed's crystal structure (G), longer bundles consisted of regularly packed parallel filaments with polycrystalline structure (H). Scale bar: 200 nm.

4.2 Mechanism of Bundle Formation

Many filaments, ribbons and bundles were formed during the course of this research, a small selection of which is presented in Figure 4-1. At the core of all bundles is the actin filament, whose mechanical and geometric properties were measured and found to be consistent with the literature. At low f-actin and high scruin concentrations, single scruin decorated actin filaments displayed an average radius significantly larger than that of the core actin filament. When higher concentrations of actin were co-polymerized with scruin at equimolar ratios, filaments were decorated and spontaneously crosslinked into ribbons, whose structure was comparable to that of the true discharge. This shows that the acrosome structure arises from the morphology of the underlying filaments.

Scruin crosslinking is irreversible so ribbon formation is kinetically trapped: ribbons must form during polymerization rather than afterwards (actin-scruin filaments intersecting at oblique angles form crosslinked networks instead). Consequently, the formation of scruin crosslinked bundles becomes highly sensitive to the initial conditions – only under low actin and high scruin concentrations could regular parallel bundles be formed. Although these bundles showed polycrystalline structure, they were sufficiently crosslinked for manipulation by optical tweezers. Shorter bundles showed replication of the seed structure but only in the first micrometer of growth, beyond which the polycrystalline structure dominated. By contrast, depletion bundle formation is not kinetically trapped and actin filaments are able to slide past each other, enabling bundles to be spontaneously formed over a wide range of conditions. These bundles also displayed a polycrystalline structure but their packing was square as opposed to the hexagonal packing of the templates from which they were seeded. In the absence of any crosslinker, actin bundles were unstructured and divergent.

Bifurcation of scruin bundles was a near universal occurrence during bundle formation and was found to be essentially independent of actin concentration (though bundle length prior to forking was typically longer under conditions of slower growth). Even under optimal bundling conditions, bundles rarely extended beyond 4-5 μm before branching, implying a limit to the free-end replication approach. One could postulate a branching probability p that increases with length from the seed L and is dependent on temperature T; actin, scruin and seed concentrations (c_a, c_s and c_t); and the quality of the seed interface q. Beyond a certain critical length L_c, the probability would trend to unity and branching would occur

$$p\left(L \rightarrow L_c, T, c_a, c_s, c_t, q\right) \rightarrow 1. \tag{4.34}$$

Formation of the acrosome mitigates this *in vivo* by assembling the bundle between two templates: on one side lies the seeding template; on the other the barbed end of the growing acrosome. This sandwich approach minimizes the distance between the bundle end and the seed thereby minimizing replication errors, dislocations and bifurcations.

The kinetics for depletion and scruin bundles at the barbed end are summarized in Figure 4-2. Despite variations within each dataset (a dataset comprised at least three actin concentrations with at least two bundles measured apiece) two trends were evident: depletion bundles formed faster than scruin bundles over all actin concentrations; and Ca^{2+} bundles formed faster than EGTA bundles at higher actin concentrations. At lower actin concentrations, EGTA bundles formed approximately twice as fast as Ca^{2+} bundles (qualitatively comparable bundles formed at half the

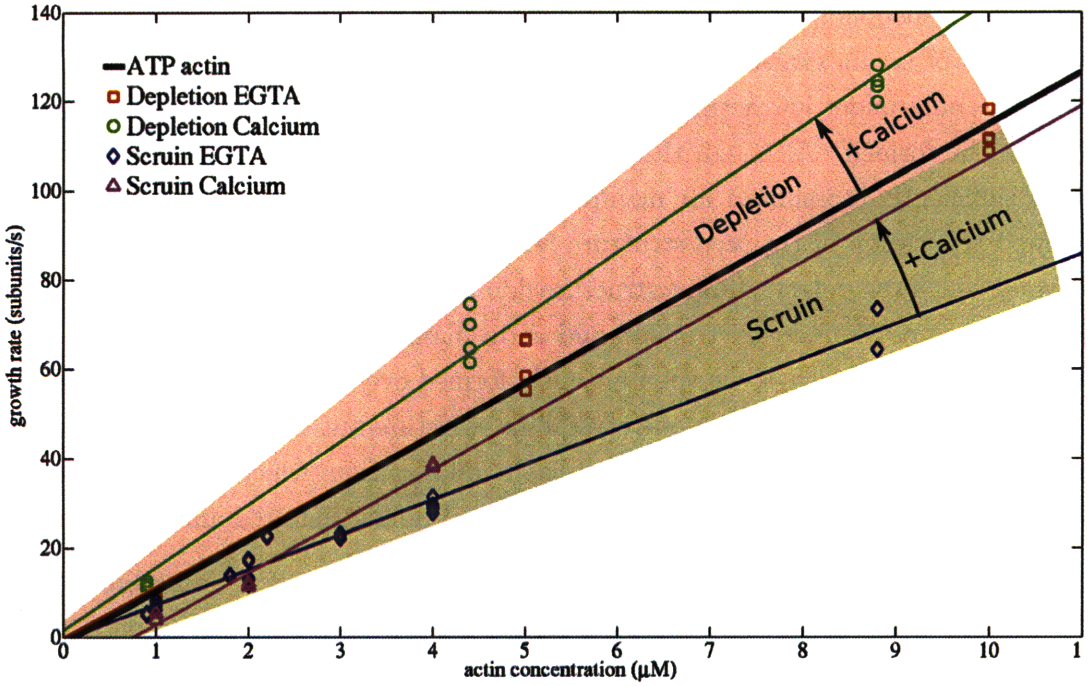

Figure 4-2: Kinetics of depletion and scruin bundles. Depletion bundles tended to form faster than scruin bundles, regardless of the presence or absence of Ca^{2+}, though the on-rate of depletion bundles in EGTA was comparable to that of scruin in Ca^{2+} (both were close to the literature values for ATP-actin). Within each group, bundles tended to form faster in Ca^{2+} than in EGTA. Phalloidin had little effect on either rate constant.

actin concentration in EGTA compared to Ca^{2+}). The slower scruin kinetics are likely due to electrostatic or steric hindrance by scruin at the barbed end of the filaments, leading to a reduction in the on-rate. The faster kinetics in Ca^{2+} is noteworthy as heretofore little difference has been observed in growth rates between Ca^{2+}- and Mg^{2+}-bound actin [22].

4.3 Mechanical Models

An order of magnitude approach represents the coarsest possible model to describe the filament and bundle mechanics and can be used to determine whether the bundles are coupled or uncoupled.

The bending rigidity of an uncoupled bundle is proportional to the rigidity and number of its constituent filaments (see Equation 1.11), while coupled rigidity scales as the square of the number of filaments (see Equation 1.13). The number of filaments in an acrosome is typically 15-85 (from Tilney [110]) and the bending rigidity of the underlying filaments was found to be 7.1-9.2$\times$10^{-26} Nm^2. For an order of magnitude assessment, assume the number N of filaments is 10-100 and the filament bending rigidity β is 10$\times$10^{-26} Nm^2. The uncoupled regime becomes

$$\beta_u = 10\beta \rightarrow 100\beta \tag{4.35}$$

$$= 0.01 \rightarrow 0.1 \times 10^{-22}\ \mathrm{Nm}^2, \tag{4.36}$$

and the coupled regime is

$$\beta_c = 10^2\beta \rightarrow 100^2\beta \tag{4.37}$$

$$= 0.1 \rightarrow 10 \times 10^{-22}\ \mathrm{Nm}^2. \tag{4.38}$$

These limits are presented in Figure 4-3 together with the bending rigidities for all filament and bundle types: Actin (f-actin filaments and dextran sulfate bundles); Scruin Calcium; and Scruin EGTA. For each bundle type the bending rigidity was found to occupy the upper limit of the coupled regime, indicating that these bundles are fully crosslinked. However, all bundles were significantly less stiff than the two acrosome conformations (TD and FD). Electron microscopy has shown that reconstituted scruin bundles had polycrystalline structure compared to their crystalline acrosome counterparts, suggesting that packing density is responsible for the significant increase in acrosome rigidity.

In order to rule out geometry as a contributing factor, the bundle elastic modulus was estimated (see Supplemental Figure 4-4). Each bundle modulus was found to be comparable to that of its constituent filaments, indicating these bundles were sufficiently tightly packed to approximate a homogeneous structure. Scruin bundles and filaments had a lower modulus than actin, consistent with the notion that scruin contributes little to the mechanical properties of these structures (beyond fully crosslinking filaments). Both scruin bundles showed a lower modulus than the true and false discharges, also consistent with the bending rigidity results. Furthermore, if the scruin bundles are modeled as a homogeneous rod with the same elastic modulus as an actin filament (886 MPa) the predicted homogeneous bundle rigidity β_h would be

$$\beta_h = 66 \pm 38 \times 10^{-22}\ \mathrm{Nm}^2, \tag{4.39}$$

here the standard deviation arises from the variation in seed diameter. This is within one standard deviation of the true discharge rigidity – so the acrosome is equivalent

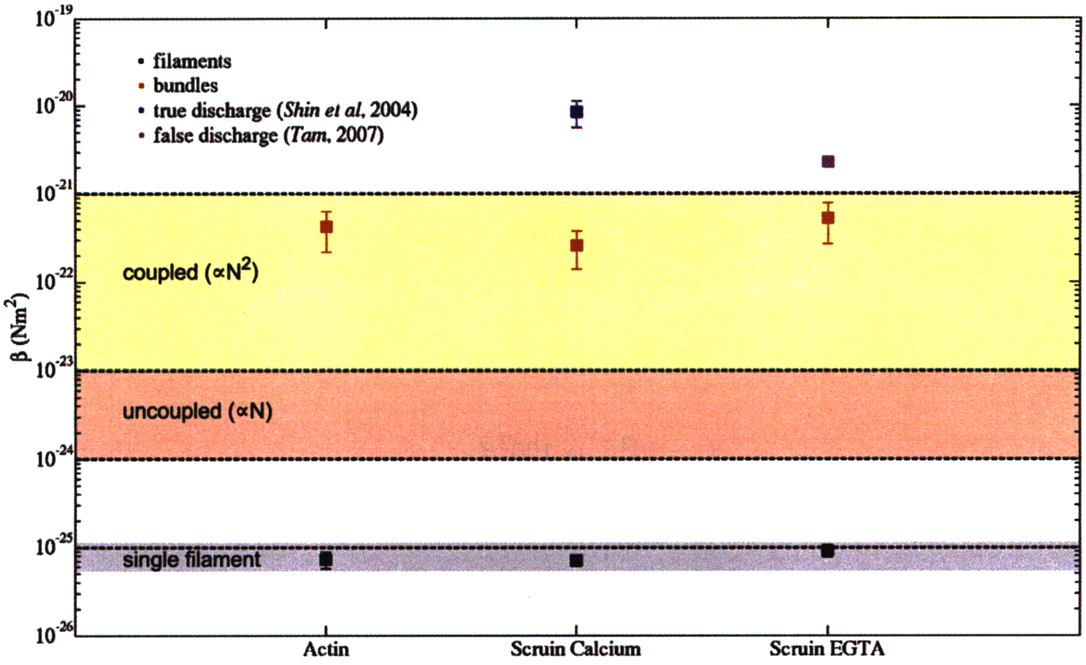

Figure 4-3: Comparison of bending rigidity for Actin (f-actin filaments and dextran sulfate bundles); Scruin Calcium; and Scruin EGTA. Actin and actin-scruin single filaments (black) were found to have comparable bending rigidities indicating that scruin decoration has little effect on filament stiffness. All bundles (red) had comparable rigidities and were consistent with fully crosslinked bundles of actin filaments. Scruin therefore contributes no mechanical stiffness to these bundles, rather it serves primarily as a rigid crosslinker to resist shear between adjacent filaments. In contrast, the TD (blue) and FD (magenta) are significantly stiffer than any reconstituted bundle, suggesting an additional regime where scruin does play a role in increasing the bundle bending rigidity, likely as a result of their optimal crystal packing.

to an isotropic rod with the equivalent material properties of a single actin filament but an order of magnitude larger diameter.

One noteworthy difference arising from the elastic modulus analysis concerns the FD, whose modulus is lower than actin filaments and close to that of the reconstituted scruin bundles. As the false discharge also displays crystalline packing, yet differs from the true discharge in its twist, one can postulate that scruin EGTA confers less stiffness to the bundle than scruin Ca^{2+}. The packing in the TD might represent the absolute optimum for this system, with the slight change in hydrodynamic radius associated with the EGTA conformation sufficient to cause the lower FD bending rigidity (while still maintaining the crystal structure).

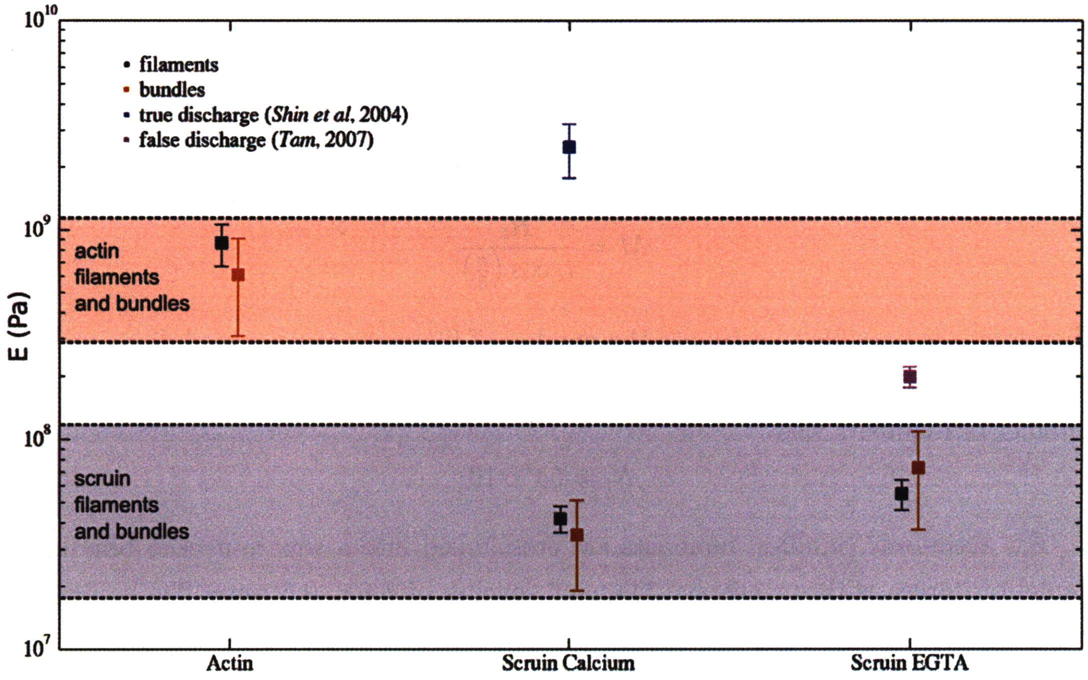

Figure 4-4: Comparison of filament and bundle elastic modulus. The elastic modulus for each bundle was comparable to that of its constituent filaments, indication that bundle packing was sufficiently tight to approximate a homogeneous structure. The modulus of scruin filaments and bundles was lower than for actin alone, due to the larger diameter of the scruin decorated filament but the same core rigidity as actin. The TD modulus was higher than all reconstituted bundles, consistent with the notion that scruin crosslinking adds rigidity to the bundle under conditions of crystalline packing. The lower FD modulus suggest a significant decrease in scruin-added-rigidity due to the conformation change in EGTA. By comparison to these bundles, the equivalent elastic modulus of reconstituted actin-scruin networks is at least eight orders of magnitude lower (0.1-300 Pa) despite the presence of crosslinked bundles observed in those experiments [46]. The marked difference illustrates the fundamental differences between the material properties of individual bundles compared to bundles crosslinked into a network.

Structural-Mechanical Models

Finer grained models were also developed, based on the geometric data gathered from electron microscopy of filaments and bundles. The key to these models lies in relating the seed diameter statistics to a corresponding number of filaments. From this the bending rigidity can be estimated using Equation 1.13.

For the packing schematic described in Supplemental Figure A-18, let the number of layers M be $[3, 5, 7, 9 and 11]$ and let the corresponding number of filaments N be $[7, 19, 37, 61 and 91]$. The seed radius R_t and the interfilament spacing t are related by

$$M = \frac{R_t}{t_t \cos\left(\frac{\pi}{6}\right)}, \tag{4.40}$$

therefore it is possible to estimate the number of filaments given a seed diameter and an interfilament spacing. Over all combinations of R_t and t_t (465 in total) the average number of filaments was

$$N_t = 54 \pm 16. \tag{4.41}$$

For actin-only bundles, filaments are crosslinked into a square-packed bundle by depletion forces with an average filament spacing of 8.6 ± 0.6 nm. The equivalent coupled bending rigidity (from Equation 1.13) is

$$\beta_{xc} = 5.9 \pm 3.5 \times 10^{-22}\ \mathrm{Nm}^2, \tag{4.42}$$

which agrees well with the experimentally obtained value of $4.3 \pm 2.6 \times 10^{-22}$ Nm^2.

For scruin bundles, an hexagonally packed model was proposed using the same filament statistics as for the depletion bundles. The material properties of scruin decorated filaments, though, are quite different: due to the comparable bending rigidity but larger diameter, scruin decorated filaments have a much lower elastic modulus than actin. An intuitive way of thinking of this is to consider a core filament of actin within a sheath of scruin – the sheath doesn't stiffen the filament, rather it acts only to resist shear between adjacent filaments. Due to the rigidity of scruin-scruin bonds, this leads to fully coupled bending.

For scruin Ca^{2+} bundles the coupled rigidity model predicted a bending rigidity of

$$\beta_{sc} = 3.3 \pm 1.9 \times 10^{-22}\ \mathrm{Nm}^2, \tag{4.43}$$

which agrees well with the experimentally obtained value of $2.6 \pm 1.2 \times 10^{-22}$ Nm^2.

For EGTA bundles, the same filament and packing geometry but difference filament rigidity was used, leading to

$$\beta_{ec} = 4.4 \pm 2.5 \times 10^{-22}\,\mathrm{Nm}^2, \tag{4.44}$$

lower than the observed $5.3 \pm 2.6 \times 10^{-22}$ Nm^2 but still within one standard deviation.

These filament models are fully consistent with the order of magnitude approach and provide a more detailed estimate for the bending rigidity, based on measurable filament and bundle properties.

4.3.1 Variational Analysis

Elastic modulus is not a measured quantity, rather it is derived from the bending rigidity (which is a measured quantity) and the filament or bundle radius (which is assumed). Moreover, the choice of filament radius has a significant effect on the predicted elastic modulus. In order to quantify its effect, a error analysis was conducted to consider variations in both actin and scruin-actin filament radius.

For the actin filament, the lower and upper bounds for the radius estimates were derived from the major-minor axis geometries and the cross-sectional area, respectively. Given a major-axis radius (a) and minor-axis radius (b), the corresponding area A and moment of area I are

$$A = \pi ab, \tag{4.45}$$

$$I = \frac{1}{4}\pi a^2 b^2. \tag{4.46}$$

For the actin filament: $a_f = 2.7$ nm, $b_f = 4.5$ nm, $A_f = 38$ nm^2 and $I_f = 116$ nm^4, equivalent to an average radius r_f of 3.5 nm. Given the cross-section area of $A_f = 25$ nm^2 the equivalent radius is 2.8 nm. So the lower bound for the actin filament radius was 2.8 nm and the upper bound was 3.5 nm. Similarly, for the actin scruin filaments: $a_{fs} = 5.3$ nm, $b_{fs} = 7.6$ nm, $A_{fs} = 127$ nm^2 and $I_{fs} = 1274$ nm^4, equivalent to $r_{fs} = 6.3$ nm for the lower bound. Half of the seed interfilament spacing (7.3 nm) was used for the upper bound.

For each choice of radius, the bending rigidity was estimated (see Table 4.2) and the 2.8 nm radius found to increase the bending rigidity by 30% and the elastic modulus by 70%. In order to account for this, the elastic modulus regimes (see Figure 4-4) were adjusted accordingly. All other parameter variations showed only modest differences.

Several additional experimental error sources were considered but ultimately dis-

Table 4.2: Effect of parameter variations on the coupled bending rigidity. Key: §average measured filament radius; †cross-sectional area radius (lower limit), major-minor axis equivalent radius (upper limit); ‡half of interfilament spacing (lower limit), major-minor axis equivalent radius (upper limit).

Parameter	Value (nm)	β_{xc} ($\times 10^{-22}$ Nm^2)	β_{sc} ($\times 10^{-22}$ Nm^2)	β_{ec} ($\times 10^{-22}$ Nm^2)
experiment		4.3 ± 2.1	2.6 ± 1.2	5.3 ± 2.6
model§		5.9 ± 3.5	3.3 ± 1.9	4.4 ± 2.5
r_f†	2.8	7.7 ± 4.6		
	3.5	4.9 ± 2.9		
r_{fs}‡	6.3		3.9 ± 2.3	5.1 ± 3.0
	7.3		2.9 ± 1.7	3.8 ± 2.2

Table 4.3: Effect of parameter variations on the elastic modulus (same key as above).

Parameter	Value (nm)	E_f (MPa)	E_{fs} (MPa)	E_{fe} (MPa)
average§		886 ± 199	42 ± 6	55 ± 9
r_f†	2.8	1514 ± 339		
	3.5	620 ± 139		
r_{fs}‡	6.3		57 ± 8	75 ± 12
	7.3		32 ± 5	41 ± 7

regarded. First, for the actin filament bending rigidity, temperature T was measured to be 22 °C– a ±3 °C change represents only a 1% difference in rigidity, so temperature variations were neglected. Second, the bundle bending rigidity has a cubic dependence on length – a ±0.1 μm length error in the fitting process resulted in a the mean bending rigidity range for the dextran sulfate bundles of 4.0-4.7$\times 10^{-22}$ Nm^2, within the original range ($4.3 \pm 2.1 \times 10^{-22}$ Nm^2) and consequently neglected.

4.4 Summary of Bundle Properties

A comparison of bending rigidity for each of the filaments and bundles measured in the previous chapters revealed several orders of magnitude difference between the stiffness of bundles and their individual filaments. An order of magnitude model estimated that all bundles were fully crosslinked. Finer grained models, that considered the electron microscopy geometric data, agreed closely with the experimentally obtained measurements for bundle rigidity. Reconstituted bundles were an order of magnitude less stiff than either the true or false discharges indicating further room for improvement in the reconstitution protocols. Images of polycrystalline rather than fully crystalline bundles are consistent with these findings.

This raises interesting conclusions on the role of scruin in crosslinking actin bundles. On a single filament level, scruin fully decorates actin filaments and significantly increases the overall filament diameter. However, there is no corresponding increase in rigidity, rather the decorated filaments maintain a persistence length comparable to that of their core actin filaments. When these filaments are packed into bundles the resultant bending rigidity is comparable to bundles formed with actin-only filaments. Once again, scruin does not contribute to the bending rigidity, rather it serves to resist interfilament shear through scruin-scruin bonds. The true and false discharge, on the other hand, display significantly higher rigidities, higher even than the upper limit of the coupled regime. This suggests an additional regime wherein scruin does contribute to the rigidity of the bundle and interacts with actin in a more homogeneous manner. Formation of crystalline structure is likely a hallmark of this interaction.

Therefore, depending on the initial conditions and the formation geometry, scruin bundles can be formed that span several orders of magnitude in bending rigidity – a significant range given just two proteins – though the bundles are highly sensitive to changes in those conditions. By contrast, depletion agents, whose osmotic pressure serves to crosslink adjacent actin filaments through steric interactions, readily form over a wide range of conditions. But their bending rigidity is limited in range and cannot exceed the coupled upper limit. These two systems therefore describe two orthogonal mechanisms: depletion bundles that are easily formed from actin alone but offer a limited range of bending rigidity; or scruin crosslinked bundles that are highly sensitive to formation conditions but can span several orders of magnitude in rigidity depending on these conditions.

Chapter 5

Conclusions

This thesis presents a comprehensive study of actin filaments and crosslinked bundles, inspired by the *Limulus* acrosomal process. During the course of the research, actin bundles were formed off acrosome fragments and crosslinked by either depletion agents or actin-binding proteins. Dextran and dextran sulfate were used as depletion agents, the *Limulus* specific scruin protein in its Ca^{2+} and EGTA conformations as an actin-binding protein. Individual scruin decorated actin filaments were found to have persistence lengths comparable to actin-only filaments, as determined by fluorescence microscopy of thermal fluctuations. Filament and seed diameters, as well as bundle interfilament spacings, were determined by measurement of negatively stained electron microscopy samples. Packing of depletion induced bundles was tighter than the major axis diameter of actin filaments; while scruin bundles interlocked at their major-axes and showed similar packing to the acrosome seeds. Kinetics were measured and optimal conditions determined for the formation of long parallel bundles.

Depletion bundles were readily formed over a wide range of conditions while scruin bundles were significantly more sensitive and formed long bundles only at low temperatures and low actin concentrations. Bundles were actively manipulated by optical tweezers and their bending rigidity directly measured. All bundles were found to be orders of magnitude stiffer than their individual filaments, consistent with fully coupled bending. Both depletion and scruin bundles had comparable rigidities, suggesting a crosslinking independent regime of actin bundle formation. In this regime, scruin crosslinking confers no mechanical stiffness and serves only to prevent shear between neighboring filaments. Moreover, these crosslinked bundles represent an intermediate regime between scruin crosslinked actin networks and the native acrosome. Elastic modulus estimates indicate a span of nine orders of magnitude between the soft networks and the rigid acrosome. This highlights the enormous range of material properties accessible through the interaction of scruin with actin, depending on the initial conditions.

This thesis builds on the foundation of actin research, which has characterized the mechanical properties of actin filaments and the structure of crosslinked actin bundles. The manipulation of depletion and scruin bundles by optical tweezers represents a novel new technique for the direct measurement of bundle mechanical properties. The extensive characterization of filament and bundle structure by electron microscopy, combined with simple mechanical models to relate the rigidity of these bundles to the material properties of their underlying filaments, provides new and important insight into the mechanism of actin bundle formation and the role of scruin as a crosslinking protein.

5.1 Future Work

The techniques developed during this research lend themselves to the study of other aspects of crosslinked bundle formation. Three key areas are envisaged for future focus: further improvement of the structure of reconstituted bundles; investigation of the uncoupled to coupled transition in the bending rigidity diagram; and direct measurement of single molecule scruin-scruin interactions.

Towards Crystalline Structure

Improved bundle structure is fundamental to exploring the transition between reconstituted bundles and their much stiffer acrosome counterparts. Bifurcation and divergence currently limit the length and structure of scruin bundles reconstituted in Ca^{2+} or EGTA. Formation in confined channels combined with a templating mechanism comparable to that in *Limulus* (as opposed to the free-end bundles presented herein) should yield improvements in bundle structure. Alternatively, daisy-chains (which form when adjacent seeds are bridged by filaments) could be used to progressively link together seeds into a hybrid bundle, potentially with significantly improved crystallinity.

With improved bundle structure comes the possibility of introducing twist and fully reproducing the FD conformation. Current bundles formed in EGTA off FD seeds show little difference in structure compared to straight bundles formed off TD seeds in Ca^{2+}. Yet the true and false discharges in their native state show significant differences in structure and mechanical properties. It is clear that only under conditions of near-optimal crystalline structure can these differences be replicated in a reconstituted system. Within this goal is the fundamental challenge of rearranging the bundle structure to introduce twist. Initial attempts to probe the rearrangement of dextran sulfate bundles placed a lower limit of several minutes on the re-organization of filaments. Further investigation should reveal timescales over which both depletion and scruin crosslinked filaments are able to rearrange their bonds in response to an external load.

Partially Crosslinked Bundles

The uncoupled to coupled transition can be probed through the study of partially crosslinked scruin bundles. Although subject to a significantly more restricted window of optimality, the formation of bundles in sub-stoichiometric scruin should reveal bending rigidities significantly lower than those measured for fully crosslinked bundles. This would also establish a lower bound for scruin's ability to crosslink actin into convergent bundles. Alternative actin-binding proteins could also be studied using the same protocols: fimbrin would be a suitable candidate given its similar size (12 nm) while vastly different bundle morphologies could be studied with the much larger α-actinin (39 nm).

Single Molecule Measurements

Finally, the strength of scruin-scruin crosslinking could be directly measured using an assay similar to that described in Ferrer *et al* [41]. Here, optical tweezers were used to probe the rupture force between α-actinin (or fimbrin) and actin filaments. A scruin-decorated actin filament could be attached to the coverslip and a second decorated filament (with bead attached) laid orthogonally on top of the first. By pulling on the top filament with the optical trap, the linear stiffness of the decorated filament and then the rupture force of the scruin-scruin bond could be discerned from the force-displacement data. Additionally, an atomic force microscope (AFM) tip could be coated with scruin, brought into contact with a scruin decorated actin filament and the bond stiffness and rupture force measured and compared to the optical trap results.

Appendix A

Supplemental Information

A.1 Euler Beam Theory

Cantilever (Fixed-Free) Bending

The transverse deflection y of an Euler beam with fixed-free boundary conditions (see Figure A-1) and bending rigidity β under an applied point load P at distance $x = L$ is

$$y\left(x\right) = \frac{P}{6\beta}\left(3Lx^2 - x^3\right), \tag{A.1}$$

for which the maximum deflection is

$$y\left(x = L\right) = \frac{PL^3}{3\beta}. \tag{A.2}$$

For small deflections, the transverse stiffness is

$$k = \frac{3\beta}{L^3}, \tag{A.3}$$

from which the bending rigidity can be calculated, given an accurate estimate for the bundle length L.

Filament (Free-Free) Bending

The bending energy U of an Euler beam is given by

$$U = \frac{\beta}{2}\int_0^L \left(\frac{d^2y}{dx^2}\right)^2 dx, \tag{A.4}$$

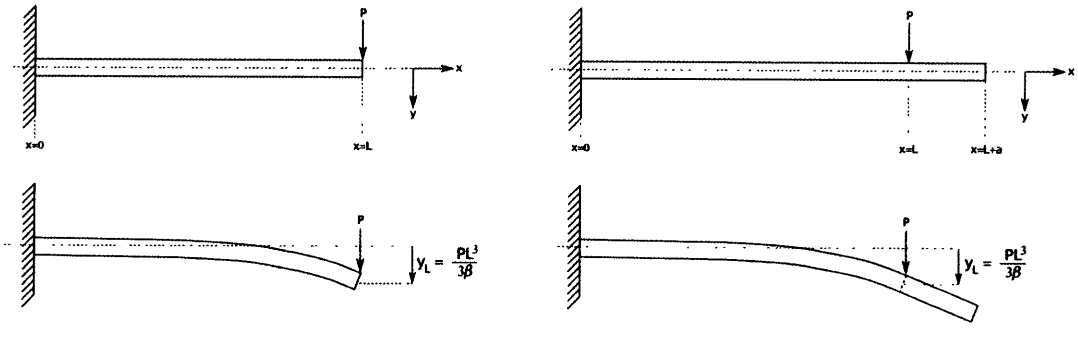

Figure A-1: Schematic of Euler beam bending with fixed-free (cantilever) boundary conditions. The maximum transverse deflection is independent of the applied load location for colocated force and displacement measurements.

Using the small angle approximation

$$\theta \approx \frac{dy}{dx} \tag{A.5}$$

$$ds \approx dx, \tag{A.6}$$

here θ is the tangent angle at arc length $s \approx x$ along the beam (Figure A-2), leading to

$$U \approx \frac{\beta}{2} \int_0^L \left(\frac{d\theta}{ds} \right)^2 ds. \tag{A.7}$$

The boundary conditions for a free-free Euler beam are zero moment

$$\left. \frac{\delta^2 y}{\delta x^2} \right|_{x=0,L} = 0, \tag{A.8}$$

and zero shear

$$\left. \frac{\delta^3 y}{\delta x^3} \right|_{x=0,L} = 0; \tag{A.9}$$

assuming small angles

$$\left. \frac{d\theta}{ds} \right|_{s=0,L} = 0, \tag{A.10}$$

$$\left. \frac{d^2\theta}{ds^2} \right|_{s=0,L} = 0. \tag{A.11}$$

All boundary conditions are non-essential (from the general solution to the wave equation, not shown) so it is not necessary to solve the wave equation for the beam

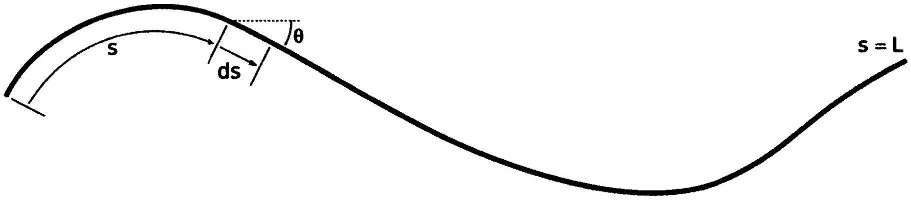

Figure A-2: Schematic of filament bending with free-free boundary conditions. The tangent angle θ at arc-length s is derived from the slope of the segment $s \longrightarrow s + ds$.

shape. Instead a simpler trial function can be chosen, such as

$$\theta_j = \sqrt{\frac{2}{L}} a_j \cos\left(k_j s\right), \tag{A.12}$$

where $k_j = \frac{n\pi}{L}$ is the wave number of the j^{th} mode and a_j are the modal amplitude coefficients (with units of $\sqrt{\mathrm{\mu m}}$). Taking the derivative

$$\frac{d\theta_j}{ds} = -k_j a_j \sqrt{\frac{2}{L}} \sin\left(k_j s\right), \tag{A.13}$$

and substituting into Equation A.7 gives

$$U = \frac{\beta}{2} \int_0^L \left(-k_j a_j \sqrt{\frac{2}{L}} \sin\left(k_j s\right) \right)^2 ds \tag{A.14}$$

$$= \frac{\beta}{2} k_j^2 a_j^2 \left(\frac{2}{L} \int_0^L \sin\left(k_j s\right)^2 ds \right). \tag{A.15}$$

Using the identity

$$\frac{2}{L} \int_0^L \sin\left(k_j s\right)^2 ds = 1, \tag{A.16}$$

gives

$$U = \frac{1}{2} \beta k_j^2 a_j^2, \tag{A.17}$$

or in terms of the average bending energy $\overline{U}$

$$\overline{U} = \frac{1}{2} \beta k_j^2 \overline{a_j^2}, \tag{A.18}$$

where $\overline{a_j^2}$ is the average mean squared amplitude coefficient. For distributions with non-zero mean ($\overline{a_j} \neq 0$), the variance $\sigma^2 = \overline{\left(a_j - \overline{a_j}\right)^2}$ is used instead. From the equipartition theory the average energy available to each mode is $\frac{1}{2}K_bT$

$$\frac{1}{2}K_bT = \frac{1}{2}\beta k_j^2\sigma_j^2, \tag{A.19}$$

where K_b is Boltzmann's constant and T is temperature (assumed to be 22 °C).

Rearranging in terms of the bending rigidity

$$\beta = \frac{K_bT}{k_j^2\sigma_j^2}, \tag{A.20}$$

then substituting $\beta = \ell K_bT$ from Equation 1.4 yields

$$\ell_j = \frac{1}{k_j^2\sigma_j^2}, \tag{A.21}$$

the units of which are m^{-2} for k_j^2 and m for σ_j^2 and ℓ_j. Here k_j and σ_j^2 are measured quantities from the thermal fluctuation timelapse images, leading to an estimate for the j^{th}-mode persistence length ℓ_j.

A.2 Supplemental Figures

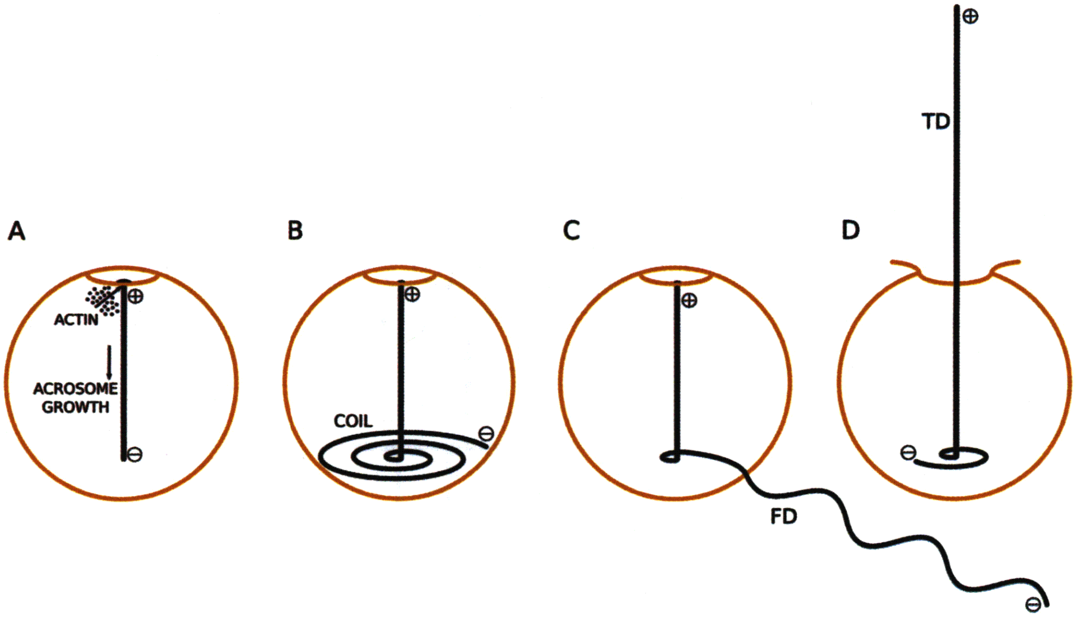

Figure A-3: Schematic of acrosome formation and conformations (not to scale). During spermatogenesis (A), growth initiates at a seeding region in the anterior of the 3-4 μm diameter cell with the preferred end of the filaments associated with the cell membrane. The acrosome grows down the nuclear channel and is bent and twisted into the coil (B). In the presence of high osmotic pressure, the coil changes twist into the false discharge and extends from the cell's posterior; it can be retracted upon relief of the external pressure. During the reaction the coil irreversibly untwists into the straight crystalline true discharge (D). There exists a continuity between the three acrosome conformations (FD ↔ coil → TD) whereby a fully extended false discharge subject to external Ca^{2+} will retract while simultaneously extending the true discharge.

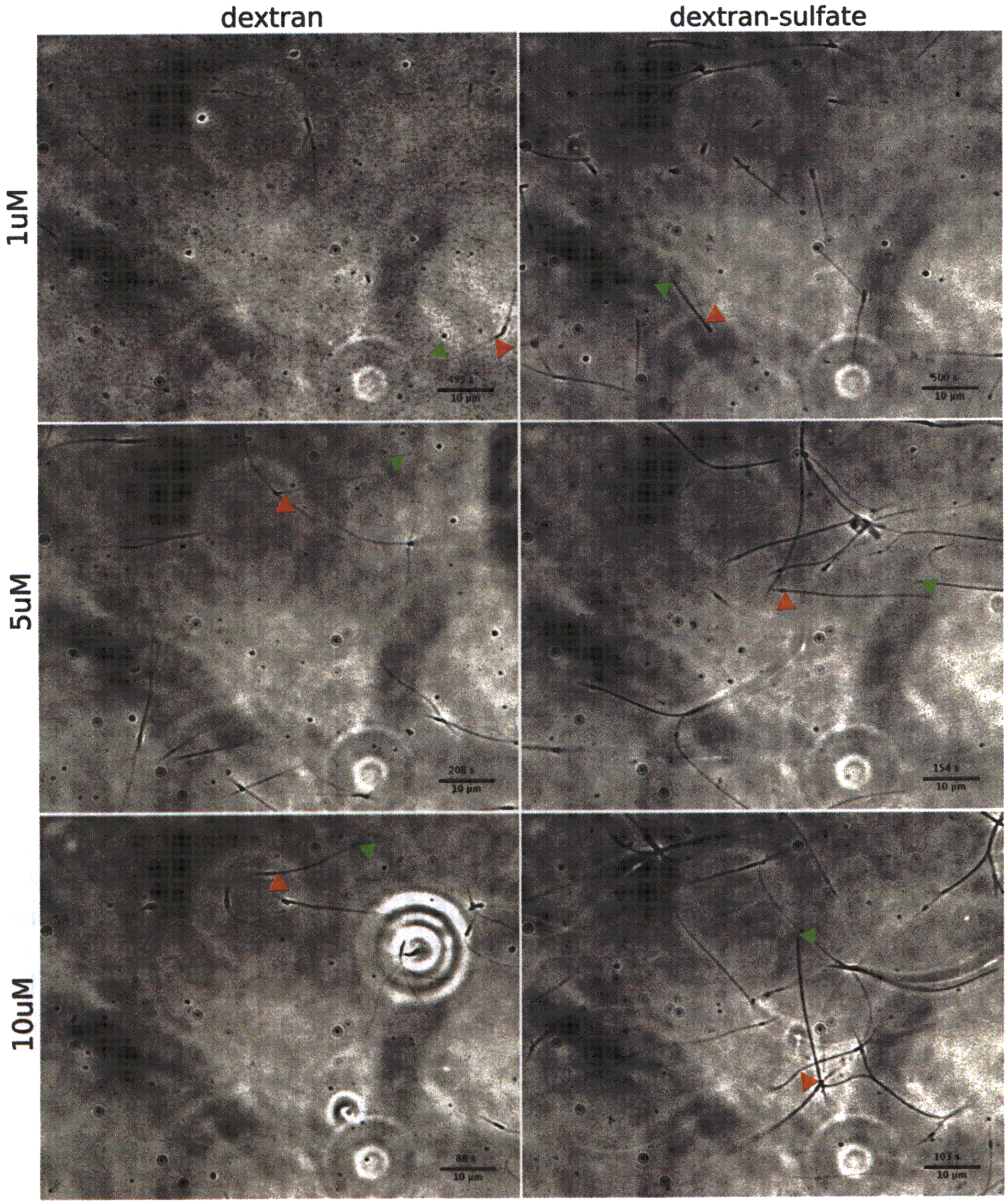

Figure A-4: Polymerization of depletion induced actin bundles. Growth of seeded bundles formed by dextran and dextran sulfate was imaged by phase microscopy (100x Ph3) for increasing actin concentrations. Bundles formed in dextran sulfate bundles were qualitatively denser than those formed under comparable conditions but in dextran. Bundles grown in 10 µM actin grew significantly faster than those in 1 µM though the final bundle density was qualitatively the same. Most bundles grew to tens of micrometers in length and maintained convergence over the entire length. Scale bar: 10 µm.

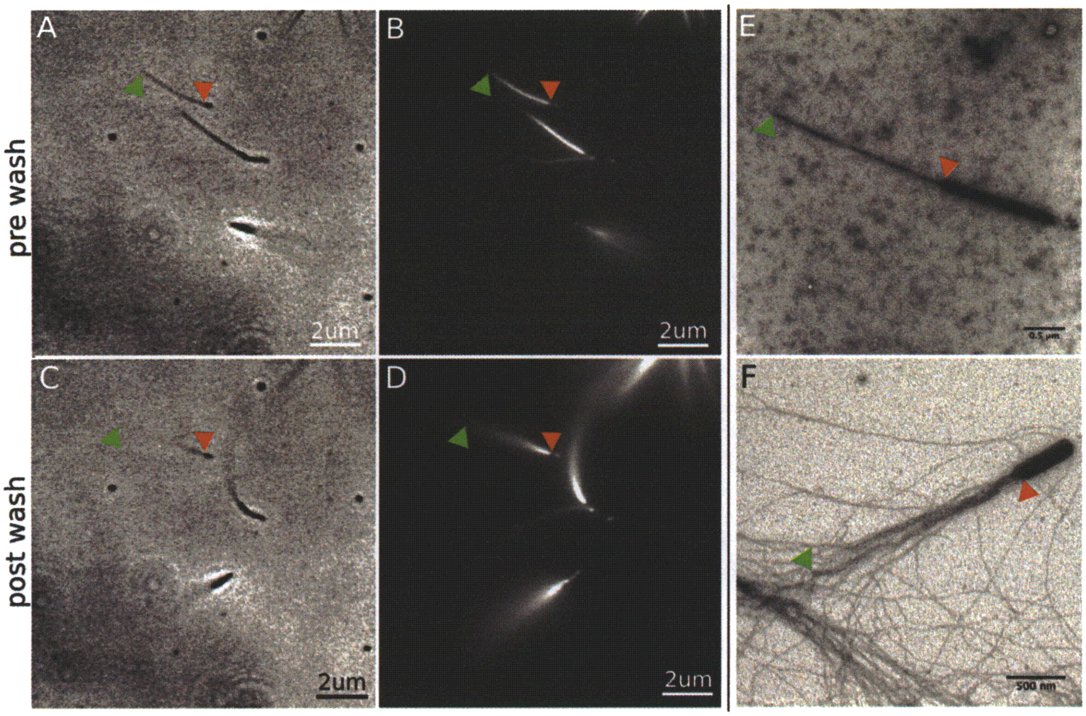

Figure A-5: Divergence of bundles upon removal of depletion agent. Dextran sulfate bundles were formed in a flowcell and imaged under phase (A) and fluorescence microscopy (B). Independent electron microscopy (E) on samples formed under comparable conditions showed consistent bundle shape and length. Removal of the depletion agent resulted in significant divergence of the bundle (F) correlated with a decrease in rigidity which caused the bundles to rise out of the imaging focal plane (C-D).

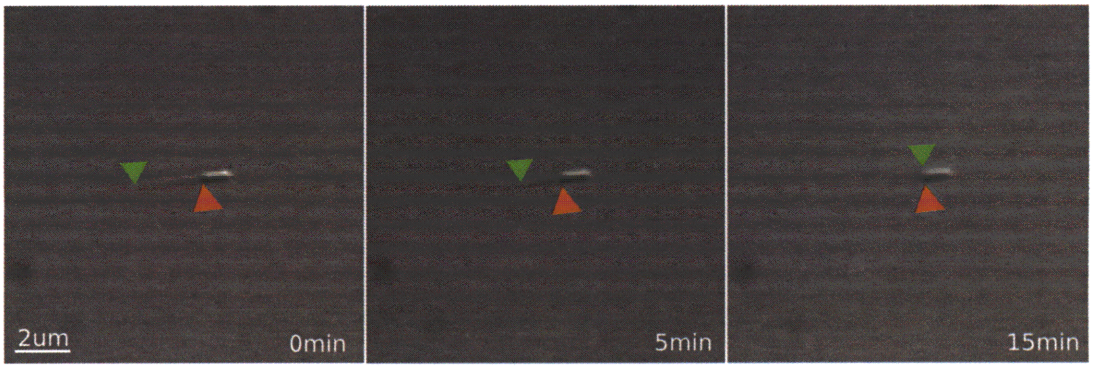

Figure A-6: Depolymerization of depletion induced actin bundles. Actin bundles formed in the absence of phalloidin depolymerized when free actin was flushed from the flowcell (and replaced by regular g-abuffer with depletion agent, to ensure ongoing bundle crosslinking). The dissociation rate was on the order 1-2 subunits per second (1-2 µm per hour) regardless of initial actin concentrations.

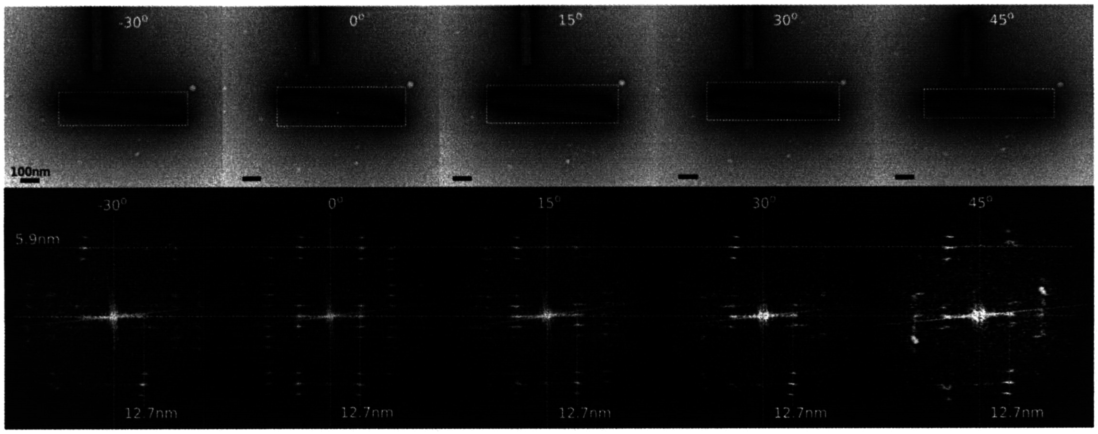

Figure A-7: Tilt series of a true discharge seed shows evidence of hexagonal packing. Original images are shown for tilt angles from -30° to 45°, their corresponding fourier transforms are rotated so that the bundle longitudinal axis is vertical in the FFT. Scale bar: 100 nm.

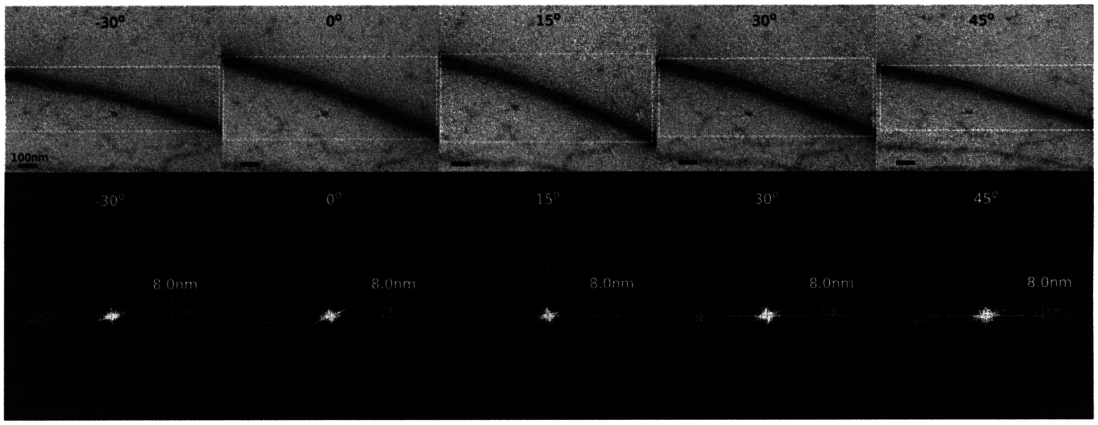

Figure A-8: Tilt series of a dextran sulfate induced bundle shows no evidence of hexagonal packing. Direct measurement of original images at -30°, 0° and 30° reveals filament spacings of 7.5 ± 0.8 nm, 8.0 ± 1.0 nm and 7.9 ± 1.0 nm, respectively. As with the TD, FFT images are rotated to align the bundle longitudinal axis with the vertical FFT axis. Scale bar: 100 nm.

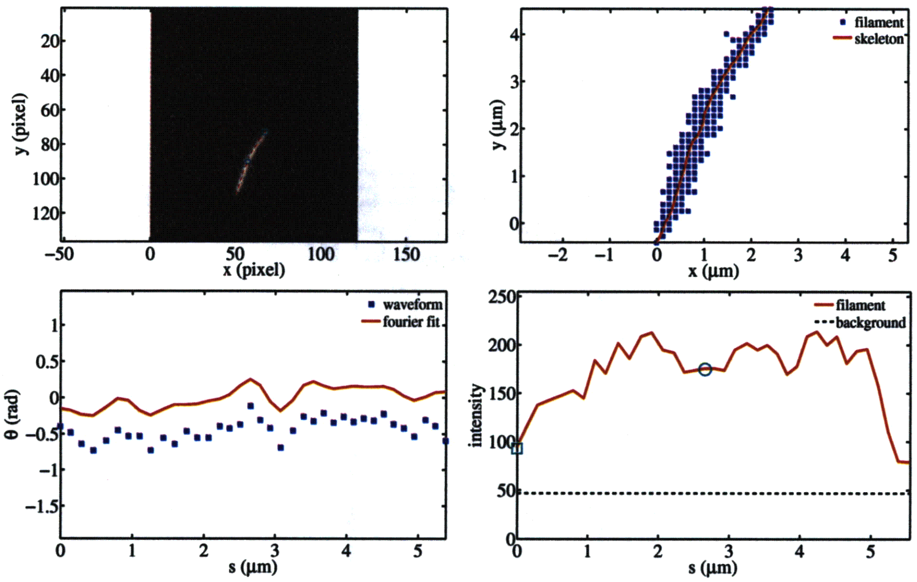

Figure A-9: Fourier reconstruction of a fluctuating actin scruin Ca^{2+} filament. Clockwise from top left: original greyscale image and skeleton (red); thresholded filament (blue) and skeleton (red); filament intensity as a function of arc length s (red) and median background intensity (black); filament tangent angle θ (blue) and fourier reconstruction (red).

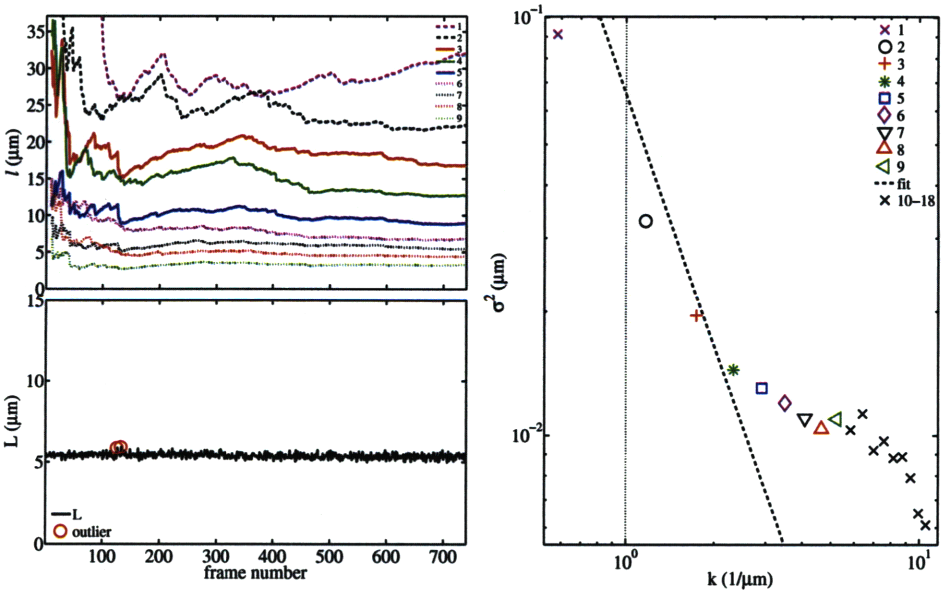

Figure A-10: Persistence length fit for actin scruin Ca^{2+} filament. Clockwise from top left: persistence length ℓ for all modes over all frames; amplitude coefficient variance σ^2 as a function of wavenumber k; filament length L over all frames. For this filament the average persistence length was 15.2 μm.

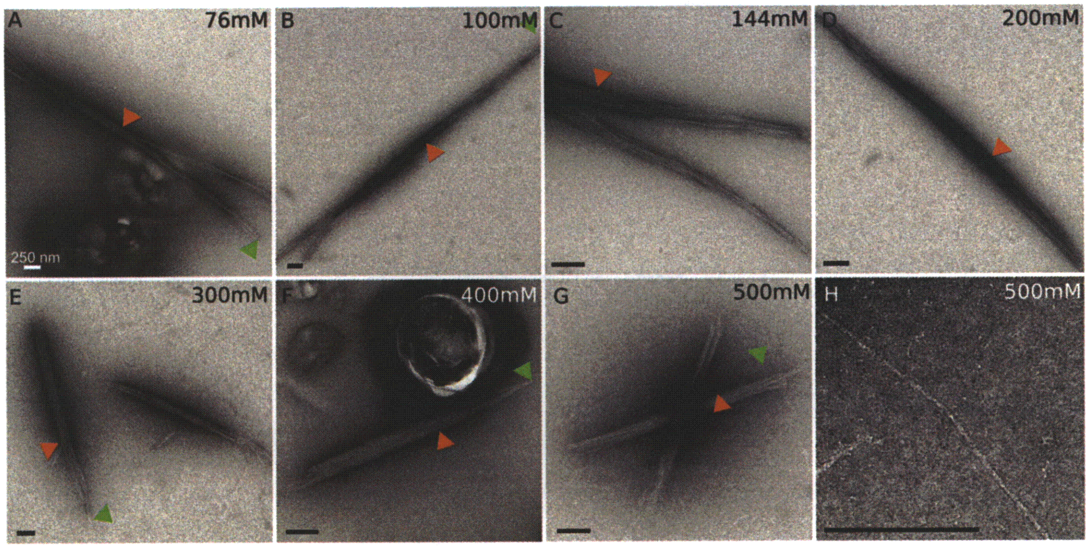

Figure A-11: Effect of ionic strength. Optimal conditions were observed for ionic strength in the range 100-200 mM (B-D), with deteriorating bundling above 200 mM (E-F). At 500 mM virtually no bundles were formed (G) and actin filaments (H) were not scruin decorated. Scale bar: 250 nm.

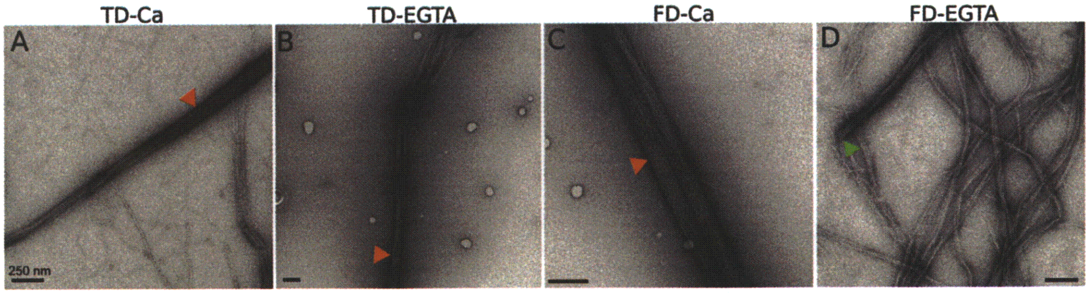

Figure A-12: Effect of seed and scruin conformation. Bundles were formed under comparable conditions, varying only the seed type and the Ca^{2+} concentration. Slightly better structure was observed for Ca^{2+} bundles, likely due to competition with unseeded filaments in EGTA (due to EGTA's promotion of spontaneous actin filament nucleation). Little difference was seen between bundles formed off either TD or FD seeds and no twist was seen for any bundle. Scale bar: 250 nm.

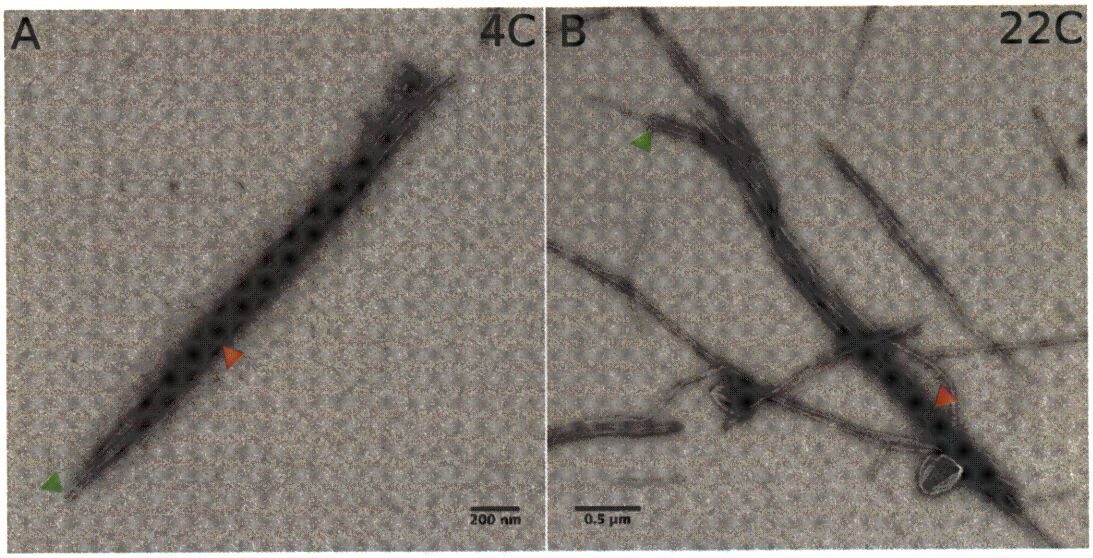

Figure A-13: Effect of temperature on bundle structure. Bundles formed at 4 °C were significantly shorter with superior structure compared to bundles formed under comparable conditions but at 22°C.

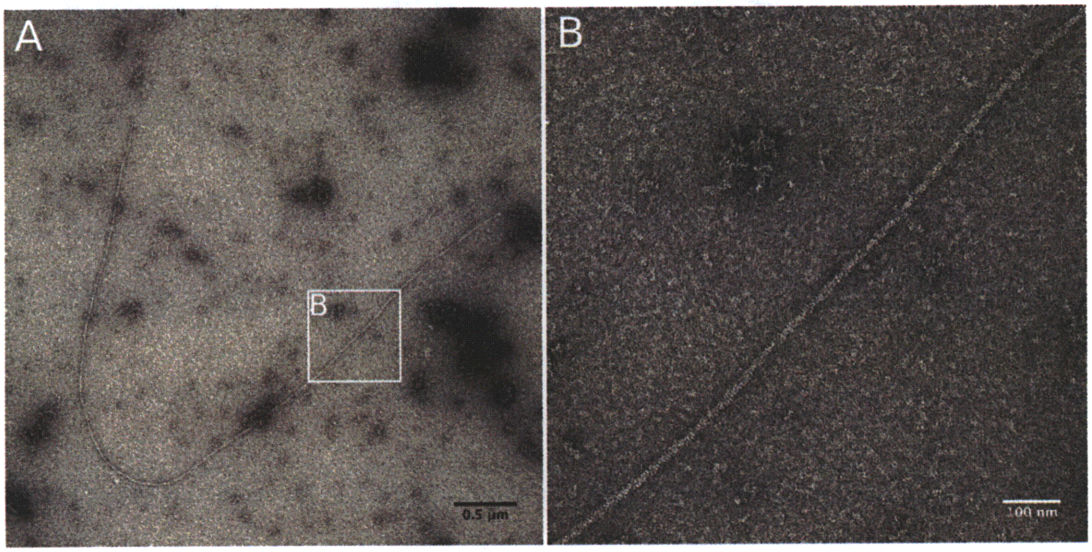

Figure A-14: Fully scruin decorated actin filament for thermal fluctuation experiments. Low concentrations of pre-formed f-actin filaments were incubated in excess scruin and found to be fully scruin decorated.

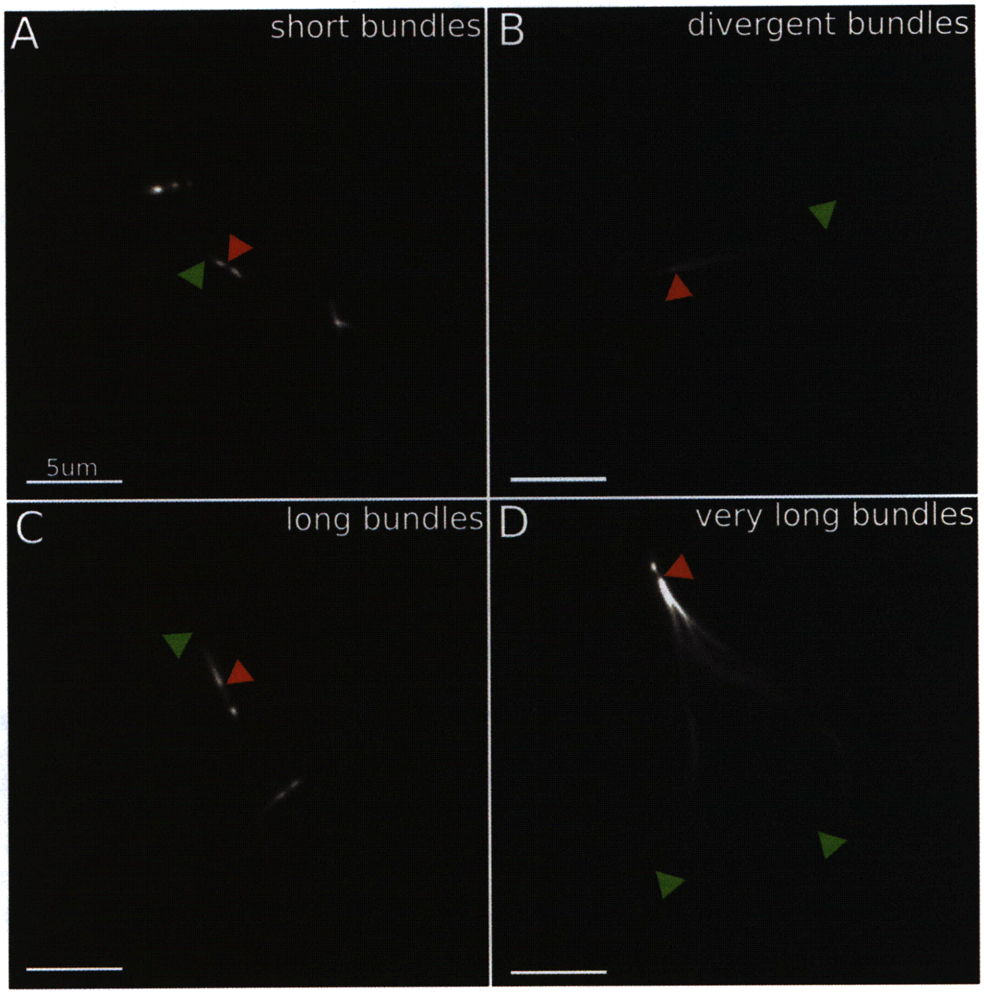

Figure A-15: Effect of scruin concentration on bundle formation in Ca^{2+} and EGTA. Bundles formed at low concentrations of both actin and scruin were very short ($A^{\dagger}$) while at higher concentrations, bundles were very long and bifurcated ($D^{\ddagger}$). Intermediate concentrations resulted in convergent bundles only in excess scruin ($C^{\S}$) but bundles formed in higher actin with low or no scruin were completely uncrosslinked (B^{*}). Conditions: $^{\dagger}Ca^{2+}$ with 500 nM actin and $\leqslant$ 50 nM scruin or EGTA with 250 nM actin and 50 nM scruin; ‡EGTA with $\geqslant$ 250 nM actin and $\geqslant$ 500 nM scruin; $^{\S}Ca^{2+}$ with 500 nM actin and $\geqslant$ 500 nM scruin; *EGTA with 500 nM actin and $\leqslant$ 250 nM scruin. Red arrows show the start of the bundle, green arrows the end.

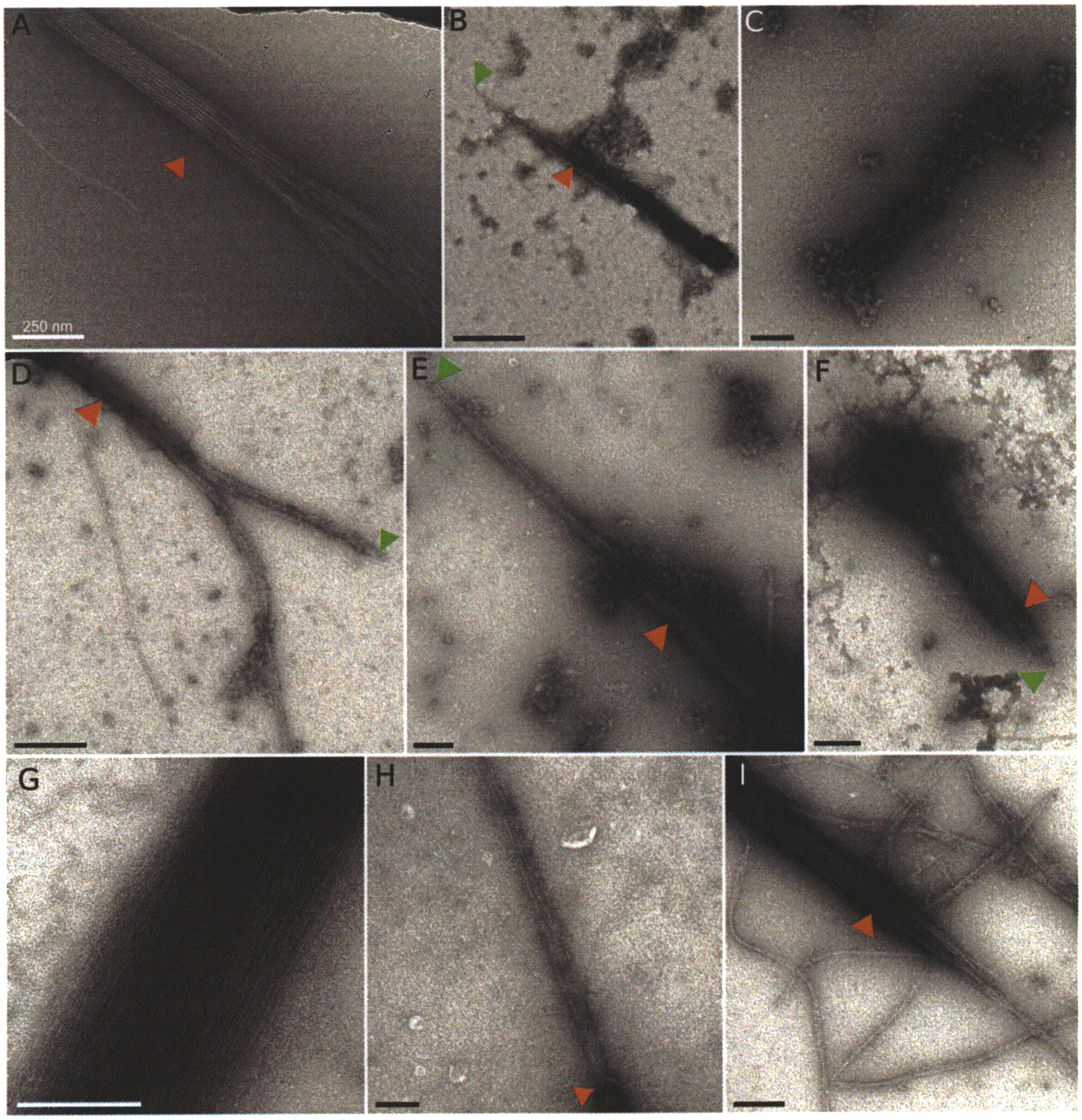

Figure A-16: Sub-optimal bundle structure. Divergence due to insufficient scruin crosslinking (A). Short tapered bundle due to short polymerization time (B). Problems with negative staining due to excess scruin (C). Forked bundle due to rapid polymerization (D). Long bundle with promising structure but slender taper (E). Short tapered bundle due to low actin concentrations and short polymerization time (F). No evidence of scruin decoration or crosslinking in unseeded (G) or seeded (H) bundles formed in dextran sulfate. Narrow tapered bundles resulting from periodic addition of monomeric actin (I). The red arrows show the start of the bundle, the green arrows the end. Scale bar: 250 nm.

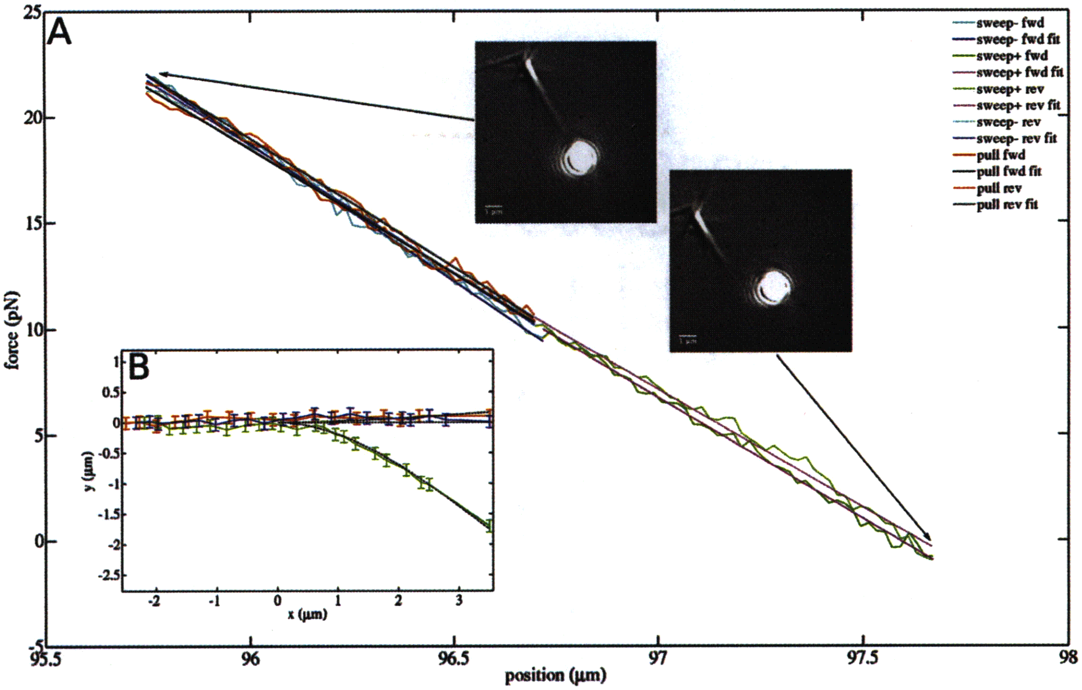

Figure A-17: Optical trap bending of a scruin Ca^{2+} bundle. Scruin crosslinked bundles were grown in 500 nM actin and 2 μM scruin over four hours at 4°C. The bundles formed were qualitatively similar to those formed by depletion agent, though without the characteristic taper of those bundles. Despite the generally poor blocking of casein against non-specific coverslip binding (particularly problematic in Ca^{2+}) a sufficient number of bundles were measured and their bending rigidity found to be comparable to dextran sulfate bundles. Here the force-displacement trace remains linear over the entire sweep-pull length (A). For the shape analysis (B) the the two extreme sweep positions (red and green) were measured and found to be consistent with beam bending theory.

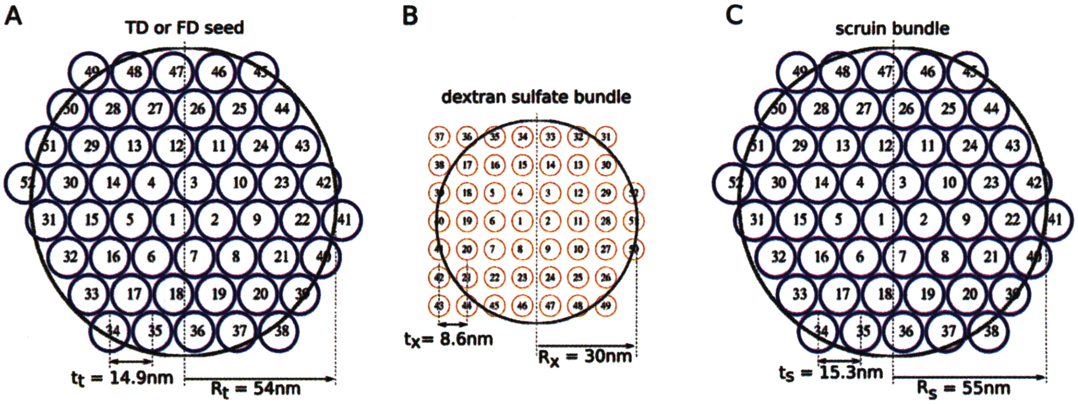

Figure A-18: Filament packing model for scruin and depletion bundles. All bundles share the same seed statistics (A, independent of TD or FD), with a filament spacing of 14.9 nm and radius of 54 nm corresponding to an average of 52 filaments per seed. Individual filaments of average radius 6.8 nm are shown in blue. Depletion bundles (B) had significantly tighter packing of 8.6 nm and an average bundle radius of 30 nm. Actin filaments of average radius 3.2 nm are shown in red. Square packing was assumed based on the fourier transforms of free dextran sulfate bundles. Scruin bundles (C, independent of Ca^{2+} or EGTA) had similar filament spacing to the seed at 15.3 nm and an average diameter of 55 nm (C). Both scruin and depletion bundles had an average of 52 filaments, the same number of filaments as the seed.

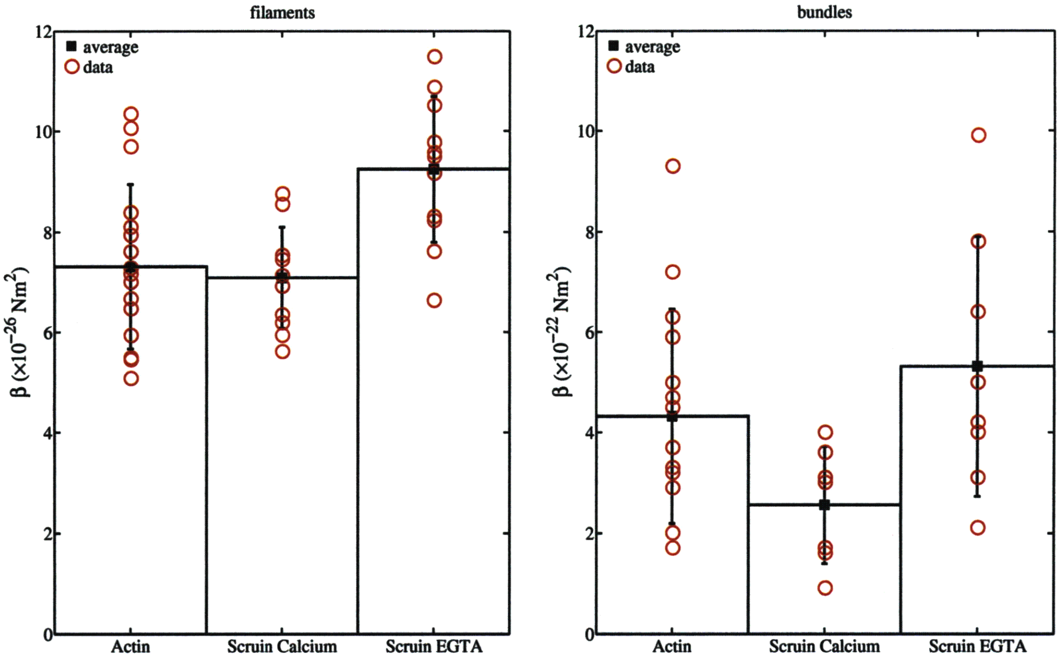

Figure A-19: Persistence length and bending rigidity of filaments and bundles. Filament persistence lengths were converted to bending rigidities (left) and compared to bundle rigidities (right). Scruin filaments showed little difference in stiffness compared to actin, indicating that scruin decoration confers no addition stiffness to the core actin filament. Scruin bundle rigidities were also comparable to actin-only bundles – scruin contributes little to these bundles either, rather it serves primarily to resist shear between filaments. Bundle rigidities were orders of magnitude stiffer than single filaments, implying full crosslinking (uncrosslinked bundles would only be 10-100 fold stiffer) and suggesting that scruin crosslinking is indeed rigid. A slight difference is noted between Ca^{2+} and EGTA, with the EGTA conformation associated with stiffer filaments and bundles.

Appendix B

Materials and Methods

B.1 Purification Protocols

B.1.1 Muscle Acetone Protocol

This protocol extracts actin acetone powder from rabbit skeletal muscle and is the first step in the purification of monomeric actin. The acetone powder can be stored for several years at -20°C.

Day 1

- Place meat grinder and acetone in cold room overnight.

Day 2

- Take one pack of tissue (150-250g) from -80°C freezer and place on ice wrapped in plastic wrap.

Myosin Extraction

- This step is necessary to dissociate the myosin from the actin to increase the yield.
- Cut up tissue (it should be semi-frozen or very cold), trim as much fat and connective tissue as possible.
- Grind in meat grinder that has been rinsed with 0.2 M EDTA. Weigh ground tissue.
- Prepare extraction buffer: (100 mM NaH_2PO_4 pH 6.5, 50 mM Na_2HPO_4, 300 mM KCl, 3 mM NaN_3, 1 mM $MgCl_2$, 10 mM EDTA, 50 μM PMSF, 2.5 mM ATP).
- Extract myosin for 10 min in cold room with constant stirring. Use 3 volumes of extraction buffer per 1 gram of tissue.
- Stop extraction by adding 3 volumes of cold water (4× overall dilution).
- Filter through 4 layers of cheesecloth.

Acetone Powder

- Wash pulp with 10 volumes of (50 mM $NaHCO_3$, 0.1 mM $CaCl_2$) in cold room for 15 minutes with constant stirring.
- Filter through 4 layers of cheesecloth.
- Wash pulp with 2-3 volumes of 10 mM (50 mM $NaHCO_3$, 0.1 mM $CaCl_2$, 10 mM Na_2CO_3).

- Stir in cold room for 10 minutes.
- Filter through 4 layers of cheesecloth.
- Add 10 volumes *room temperature* water to pulp and filter immediately through 4 layers of cheesecloth.
- From this point on, work at *room temperature* in the hood.
- Add 2 volumes *cold* acetone to pulp, stir and let stand for 15 minutes.
- Filter through 4 layers of cheesecloth.
- Repeat acetone step until solution comes out clear. Usually it is necessary to repeat only once.
- Place acetone treated pulp on large filter paper and cover with cheesecloth. Allow to dry overnight in the hood.

Day 3

- Pulverize dried pulp using a small grinder to give actin acetone powder.
- Weigh powder and place in -20°C freezer. Yield is around 10% of wet muscle.

B.1.2 Purification of Monomeric Actin

This protocol extracts monomeric actin from the actin acetone powder prepared above. It primarily consists of several polymerization-depolymerization steps designed to cycle actin from its filamentous to its monomeric forms, eventually producing a small volume of high purity g-actin.

Day 1

- Prepare: 30 ml of cold (2.5 mM Tris pH 8, 0.1 mM ATP): 1.5 ml of 50 mM Tris, 30 μl of 0.1 M ATP, cold MilliQ.
- Check pH (add 3 μl 10M NaOH to 30ml for pH 8).
- Add 1 g acetone powder (see Section B.1.1 above) to 20 ml of (tris-atp).
- Put in cold room for 15 minutes, stirring gently.
- Filter through Whatman #54 on #1 paper on ice using ceramic funnel (635).
- Take the remaining pulp and re-suspend in 10 ml of (tris-atp).
- Put in the cold room for 12 minutes, stirring gently.
- Filter remaining filtrate.
- Spin the filtrate for 15 min at 19,000 rpm (43e3g/SS-34).
- Wash the funnel with DI water.
- Filter supernatant through a 0.2 μm steriflip filter.
- Measure its volume then transfer to 70Ti centrifuge tube.
- To 15ml supernatant add (150 μl of 1 M NaCl, 10.5 μl of 1 M $MgCl_2$) for (10 mM NaCl, 0.7 mM $MgCl_2$).

- Incubate on rocker table for 12 hours at 4°C.

Day 2

- Spin the actin mixture for 3 hours at 50,000 rpm (2e5g/70Ti).
- Prepare 500 ml of (1 × g-buffer, 0.2 mM ATP, 0.5 mM DTT): 50 ml of 10× g-buffer no ATP, DTT, 100 µl of 1M ATP, 250 µl of 1M DTT, MilliQ.
- Check pH. 1 drop (25 µl) of 10 M NaOH in 500 ml for pH 7.5.
- Cut a 10 cm length of diameter 7 mm MW 6-7k (or 12-14k) dialysis tube and rinse in DI water.
- Resuspend the pellet in 1.5 ml (gbuff-atp-dtt) and inject into dialysis membrane.
- Put dialysis membrane in (gbuff-atp-dtt) and dialyze on stirrer in cold room.

Day 3-4

- Change buffer every day with fresh buffer. Flip dialysis bag every day to ensure even depolymerization.

Day 5

- Prepare 20 ml of (1× g-buffer, 0.2 mM ATP, 0.5 mM DTT): 2 ml of 10× g-buffer no ATP/DTT, 4 µl of 1M ATP, 10 µl of 1M DTT, MilliQ.
- Dilute g-actin to 20 ml in (gbuff-atp-dtt)
- To 20 ml supernatant add (200 µl of 1M NaCl, 14 µl of 1M $MgCl_2$) for (10 mM NaCl, 0.7 mM $MgCl_2$).
- Incubate overnight on rocker table at 4°C.

Day 6

- Spin the actin mixture for 2-3 hours at 50,000 rpm (2e5g/70Ti).
- Resuspend the pellet in 600 µl fresh (gbuff-atp-dtt), inject into dialysis membrane and dialyze in cold room.

Day 7

- Change buffer and flip dialysis bag.

Day 8

- Remove the g-actin from the dialysis tube (rinse tube with 200 µl of g-buffer).
- Spin for 2 hours at 50,000 rpm (18e4g/TLA120.2).
- Take top 50 µl (use within 1 week).
- Add 1:10 10× f-buffer to pellet/remaining supernatant and store at 4°C.
- Determine the concentration
    - Bradford assay at 1:20 dilution in (gbuff-atp-dtt) [12].
    - Spectrophotometer at 1:10 in ATP-free buffer (extinction coefficient = 1.1).

Days 15-17

- Transfer f-actin to dialysis membrane, dialyze in cold room.
- Change buffer and flip dialysis bag.

- Spin for 2 hours at 50,000 rpm (18e4g/TLA120.2), take 100 µl and measure concentration.

B.1.3 Gelsolin Coated Beads

This protocol coats 1 µm diameter polystyrene beads with gelsolin, which binds tightly to the barbed end of actin filaments. When attached to an actin filament or bundle, the bead can be manipulated by optical tweezers to probe the mechanics of that filament or bundle. Protocol from Hyungsuk Lee, Kamm Lab, MIT. Original protocol from Suzuki [104].
Day 1

- Buffers/reagents:
  - 100 mM borate buffer
  - 2.5% carboxylated microspheres
  - 100 mM Sodium carbonate buffer pH 9.6
  - 20 mM Sodium phosphate buffer pH 4.5
  - EDC (-20°C freezer)
  - 250 mM ethanolamine
  - Solution A (100 mM borate buffer pH 8.5, 0.1 mM $CaCl_2$ and 0.1 mM ATP)
  - Solution B without ATP (150 mM NaCl, 20 mM sodium phosphate buffer pH 7.4, 0.1 mM $CaCl_2$, 10 mg/ml BSA, 5% (v/v) glycerol, and 0.1% (w/v) NaN_3)
- Place 500 µl of 2.5% carboxylated microspheres in an Eppendorf centrifuge tube and add 500 µl of sodium carbonate buffer.
- Wash beads 4x by centrifugation for 5 minutes at 10,000 rpm.
  - After each wash, re-suspend by filling half way with sodium carbonate buffer, then vortex, and finally fill the tube with buffer.
- After last wash, re-suspend beads by adding 1 ml of sodium phosphate buffer.
- Wash 4x as above, but using sodium phosphate buffer.
- After last wash, re-suspend beads in 625 µl of sodium phosphate buffer and sonicate for 30 seconds (25% on cup sonicator in basement).
- Dissolve 20 mg of EDC in 1 ml of sodium phosphate buffer (2% w/v) and add 625 µl of this solution to the bead suspension. EDC solution should be prepared 15 minutes prior to using.
- Mix continuously and gently for 3.5 hours at room temperature.
  - Prepare borate buffer and solution A during the incubation.
- Centrifuge for 7 minutes at 10,000 rpm, and remove supernatant.
- Resuspend pellet with 1.25 ml of 100 mM borate buffer and wash beads 4x (5 minutes at 10,000 rpm) resuspending each time with borate buffer.
- After last wash, re-suspend beads in 700 µl of solution A and sonicate for 30 seconds (25% on cup sonicator).

- Use 500 µl of solution A to dissolve protein mix (choose one of the following)
  - protein mix (with actin): 5 µl of 10 mg/ml actin, 10 µl of 5 mg/ml gelsolin, 26 µl of 10 mg/ml BSA and 40 µl of 1 mg/ml rhodamine-BSA (total 400 μg of protein).
  - protein mix (no actin): 10 µl of 5 mg/ml gelsolin, 31 µl of 10 mg/ml BSA and 40 µl of 1 mg/ml rhodamine-BSA (total 400 µg of protein).
- Add protein solution to bead solution and mix continuously and gently for 8-10 hours at room temperature in dark.

Day 2

- Stop the reaction by adding 50 µl of 250 mM ethanolamine, and mix gently for 30 minutes at room temperature in dark.
  - Mix 20 µl of ethanolamine with 1300 µl of borate buffer to obtain 250 mM ethanolamine.
- Centrifuge bead solution for 7 minutes at 10,000 rpm, and re-suspend in 1200 µl of 10 mg/ml of BSA in solution A (1500 µl solA = 1491 µl borate buffer + 7.5 µl 20 mM $CaCl_2$ + 1.5 µl 100 mM ATP).
  - Prepare more solution A.
  - Mix 50 mg of BSA with 5 ml of fresh solution A.
- Sonicate for 30 seconds (25% on cup sonicator), and mix gently for 30 minutes.
- Wash beads 3 times at 10,000 rpm using 10 mg/ml BSA in solution A (5 ml borate buffer, 5 µl 100 mM ATP, 25 µl 20 mM $CaCl_2$)
- Prepare 10 ml of solution B:
  - 9.5 ml 20 mM sodium phosphate buffer, adjust to pH 7.4
  - add 88 mg NaCl, 10 µl 100 mM $CaCl_2$, 100 mg BSA, 0.5 ml glycerol, 10 mg NaN_3
- After last wash, re-suspend beads in 1 ml of solution B.
  - Add 1 ml of solution bead to bead pellet and vortex.
  - Add 10 µl of 10 mM ATP.
- Store at 0°C in dark. The coated beads are usable for about 6 months. Check binding with the assay described in Section B.2.

B.1.4 Purification of Monomeric Scruin

This protocol purifies monomeric scruin from horseshoe crab sperm. It yields a 500 µl peak fraction of 2 mg/ml scruin (MW 120 kD) – store at 4°C and use within 2 months.
Day1

- Collect 20 ml of sperm from horseshoe crabs; keep the sperm on ice while collecting.
- Takes around 2 hours at Wood's Hole.

Day2

- Prepare 1 L of (1× a-buffer, 0.5 mM DTT): 100 ml 10× a-buffer, 500 µl 1 M DTT, H_2O. Filter. Check pH.
- Wash the AcA-44 column: Put 1 L of (abuff-dtt) in large conical beaker. Put the column outlet tube into a beaker and open the column valve.
- Run overnight.

TD Extraction

- Prepare 200 ml of (0.5× ASW, 25 mM $CaCl_2$): 40 ml 2.5× ASW, 1 ml 5 M $CaCl_2$, H_2O, Pepstatin-A powder, 100 µl Leupeptin, 200 µl Aprotinin, 200 µl PMSF. Check pH.
- Add the sperm to a 300 ml conical beaker with 200 ml (asw-cacl).
- Incubate 30 min on ice.
- Homogenize with Biomixer
  - Biospec Products, blade attachment, speed I 5x8 sec.
  - Wait 60 sec between pulses to avoid overheating of sample.
  - Use the tall 300 ml beaker to avoid bubbles. Keep on ice at all times.
- Spin 10 min at 3250 rpm (2400g/BC-6R). Use 6 tubes.
  - Prepare 100 ml of (0.5× ASW, 25 mM $CaCl_2$): 20 ml 2.5× ASW, 0.5 ml 5 M $CaCl_2$, H_2O, Pepstatin-A powder, 50 µl Leupeptin, 100 µl Aprotinin, 100 µl PMSF. Check pH.
- Keep supernatant, keep pellet.
- Resuspend the pellet in 100 ml (asw-cacl). Use 4 tubes. KEY STEP!
- Spin 10 min at 3250 rpm.
- Keep supernatant, discard pellet.
- Spin all the supernatant for 10 min at 3250 rpm (2400g/BC-6R). Use 6 tubes.
- Spin the supernatant for 20 min at 20,000 rpm (43e3g/SS34). Use 8 tubes.
  - Prepare 15 ml of (1× a-buffer, 0.5 mM DTT, 38 mM hecameg): 1.5 ml of 10× a-buffer, 7.5 µl 1 M DTT, H_2O, 0.191g of hecameg.
  - Mix for 20 min to ensure the hecameg is fully dissolved. Filter with steriflip to remove undissolved hecameg.
  - Add inhibitors to 15 ml (abuff-dtt-hecameg): 7.5 µl Leupeptin, 15 µl Aprotinin, 15 µl PMSF, Pepstatin-A powder. Check pH.
- Keep pellets, discard supernatant.
- Resuspend pellets in 15 ml of (abuff-dtt-inhib-hecameg).
- Carefully homogenize 3× with a 15 ml tissue grinder (Wheaton).
- Incubate 15 min on ice.

  - Prepare 175 ml (1× a-buffer, 0.5 mM DTT, inhibitors): 17.5 ml 10× a-buffer, H_2O, 87.5 µl 1M DTT, 87.5 µl Leupeptin, 175 µl Aprotinin, 175 µl PMSF, Pepstatin-A powder. Check pH.

- Add 175 ml (abuff-dtt-inhib) to 15 ml sample in a conical beaker. Transfer to 6x SS34 tubes.
- Spin for 20 min at 20,000 rpm (48e3g/SS34).
  - Prepare 90 ml of (1× a-buffer, DTT, inhibitors): 9 ml (10× a-buffer), H_2O, 45 µl 1 M DTT, 45 µl Leupeptin, 90 µl Aprotinin, 90 µl PMSF, Pepstatin-A powder. Check pH.
- Save the pellets, discard supernatant.
- Resuspend pellets in 90 ml of (abuff-dtt-inhib). Use 2 tubes.
- Spin for 20 min at 20,000 rpm (48e3g, SS34).
  - Cool bottle of 5M $CaCl_2$ on ice.
  - Cool the L8-70M ultracentrifuge to 4°C.
  - Prepare 8 ml of (1× a-buffer, 0.5 mM DTT, inhibitors, E64): 1 ml of 1× a-buffer, 7 ml H_2O, 5 µl 1M DTT, 5 µl Leupeptin, 10 µl Aprotinin, 10 µl PMSF, Pepstatin-A powder, 10 µl E64. Check pH.
- Keep pellet, discard supernatant.
- Resuspend pellets in 8 ml of (abuff-dtt-inhib-e64).
- Homogenize 3× in the 15 ml tissue grinder.
- Add 2 ml of 5M $CaCl_2$ for 1 M $CaCl_2$ final concentration.
- Homogenize 3× more.
- Incubate at 0°C for 30 min, mixing every 5-10 min.
  - This step is critical to crystallize the actin and separate it from the scruin.
  - Gently mix the solution 3x in the homogenizer with a transfer pipette.
- Spin for 45 min at 20,000 rpm (48e3g/SS34). Use 1 tube.
- Remove immediately, keep supernatant, discard the pellet.
- Transfer to a 70Ti centrifuge tube for the next spin.
- Spin for 60 min at 40,000 rpm (15e4g/70Ti). Use 1 tube.
- Remove immediately, keep supernatant, discard pellet.
- Transfer to a 15 ml centrifuge tube for the AcA-44 column.

AcA-44 Column

- Make sure the column is equilibrated. Close the column valve.
- Use the BioRad fraction collector: 230 drops/tube.
- Tape the sample to the side of the column and move the column tube from the buffer beaker to the sample. Clamp the main beaker tube to prevent air bubbles.

- Open the column valve. Press Run on the collector.
- When sample loading is done (1 ml/min, 10 min for 10 ml), pour about 1 ml of (abuff-dtt) from the conical buffer beaker into the sample tube and wait till it runs out (1 min). Move the tube back to the buffer beaker.
- Make sure that the collector moves to the next tube automatically.
- Prepare 500 ml of (1× a-buffer, 0.5 mM DTT) to fill up column beaker: 50 ml 10× a-buffer, 250 µl 1M DTT, H_2O.
- Fill main beaker with more (abuff-dtt).
- Run overnight.

Day 3

- Close the column valve and turn off the fraction collector.
- Check the tubes with Bradford: 50 µl Bradford + 10 µl sample. Fractions 17-20 are actin, 20-28 scruin. There should be a dip around fraction 20 or 21.
- Pool 20-28 (depends on the column and the drop size) in a 100 ml beaker.

MonoQ ionic exchange column

- Prepare buffers
  - 500 ml of (1× a-buffer, 1 mM DTT): 50 ml 10× a-buffer, 500 µl 1M DTT, H_2O. Check pH. Check pH. Filter.
  - 200 ml of (1× b-buffer): 20 ml of 10× a-buffer, 200 µl 1M DTT, 45 ml of 4 M NaCl (for a total of 1 M NaCl, note 1× a-buffer already has 100 mM NaCl), H_2O. Check pH. Filter.
- Set aside 50 ml (abuff-dtt) for the superloop priming syringe.
- Put tube A in the a-buffer bottle, tube B in the b-buffer bottle.
- Pump wash
  - Manual – pump – pumpwash – pump A and B ON – execute
  - This will take about 3 min during which time the light will be red and say Pause, then will turn green once done). Once done, set both to OFF, execute, then press END.
- Connect the MonoQ column to (1: top/red) and (flow cell: bottom/black). Check detection wavelength is 280 nm.
- Column wash
  - Manual – pump – flow – 1 ml/min – execute.
  - Manual – pump – gradient – 100% B – execute.
  - Wait for at least 5 column volumes (5 ml, 5 min) to make sure that the conductivity has reached maximum.
  - Manual – pump – gradient – 0% B – execute (to equilibrate the column with a-buffer, 10 min, 15 ml total).
  - Press END to stop.

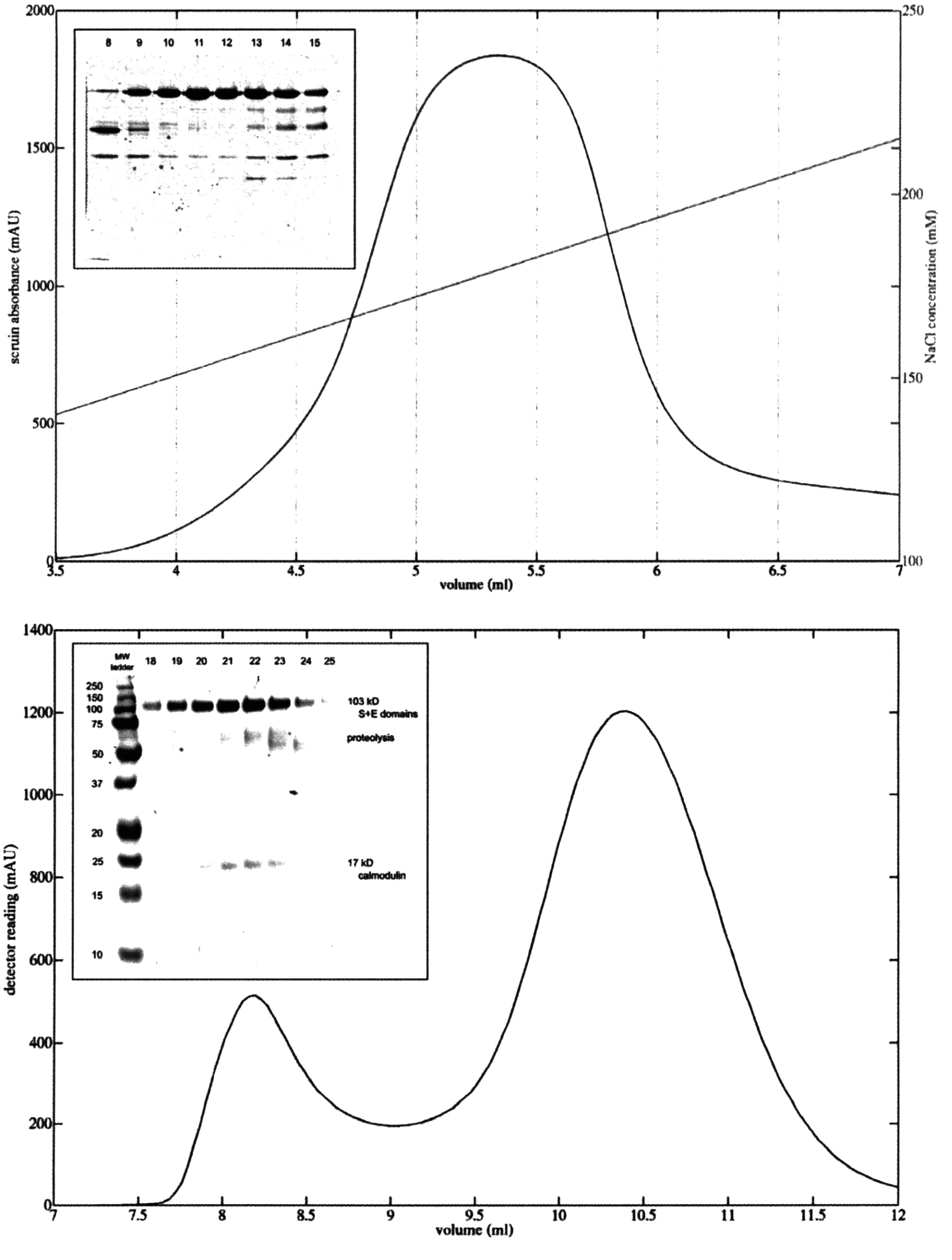

Figure B-1: MonoQ elution trace (top) with absorbance (left axis) and corresponding NaCl concentration (right axis). Fractions 9 – 12 (volume 4.5-6.5 ml) were generally chosen for further purification, corresponding to an NaCl elution concentration range of 160-200 mM. S12 size exclusion trace (bottom) with peak fractions at around 10 ml resulting in approximately 2 mg/ml of scruin. The purity of selected fractions was confirmed by protein gels (insets).

- Assemble the superloop.
    - Get the 50 ml glass tube superloop
    - Get the floater (white delrin cylinder with black o-ring at one end) and the end caps (delrin cylinder with flange and o-ring). Wet everything with DI water.
    - Put in the floater (50 ml mark is the top) with the o-ring down, then insert the top end cap. On the bottom, put the end cap with the groove aligned with the small notch in the bottom of the tube.
    - Screw on the black end caps.
    - Get 2 tubes (connectors) and put the longer on the bottom, shorter on the top.
    - Get the loop stand from next to the FPLC fridge and mount the superloop with the top upwards.
    - Get a 60 ml syringe, fill with 50 ml of (abuff-dtt), put the syringe adaptor on the end of the top tube and inject the 50 ml into the superloop from the top.
    - Fill the syringe with 50 ml scruin solution, connect the syringe to the bottom and inject 50 ml of scruin solution (if the volume of scruin exceeds 50 ml then will need to inject rest 10 minutes into the FPLC) so that the floater is pushed upwards.
    - Put the superloop in the left slot in the FPLC fridge and connect the top tube to #6.
    - Disconnect syringe and put the bottom tube to #2.
- Load MonoQ
    - Manual; Alarms Mon; Alarm Pressure; HighAlarm; 5; Execute.
    - Manual; Pump; Flow; Flow rate; 1 ml/min; Execute.
    - Manual; Flowpath; Injectionvalve; Inject; Execute.
    - After about 30 min inject the remaining scruin.
        - Press “Pause” and disconnect the top tube.
        - Fill the 60 ml syringe with the remaining scruin solution and connect to the bottom of the superloop.
        - Inject the remaining scruin solution. Press “Continue”.
    - This will take about 90 min for 90 ml and when loading is done the floater will be at the bottom.
    - Press End.
- Select “MonoQ scruin” program from Main window. File – run.
    - Accept the default settings, collect 0.5 ml fractions and specify output filename for data.
    - Collection should take about 30 min, a good sample should give a peak at tube #10 of around 1800 mAU.
- Wash the superloop. Fill the 60 ml syringe with H_2O and inject through the bottom tube. Dismantle and dry.

S12 size exclusion column

- Prepare 300 ml of (1× p-buffer, 1 mM DTT): 30 ml 10× p-buffer, H_2O, 300 µl 1 M DTT. Check pH. Filter.
- Setup column:
  - Place tube A in the (pbuff-dtt) beaker.
  - Connect the Superose S-12 column (top tube to #1, bottom to detector).
  - Connect the 500 µl loops between #2 and #6.
  - Prime the loop with 1 ml of (pbuff-dtt) using a fresh 1 ml syringe.
  - Pump wash: Manual – pump – pumpwash – A ON – execute (3 min for the green light will turn on).
  - Equilibrate the column: Manual – pump – flow – 0.5 ml/min. For 45 ml or 90 min.
- Check the fractions with bradford instead (50 µl bradford + 2 µl sample).
- Pool fractions 9-12 and concentrate
  - Use 6 ml 5000MW viva spin concentrator
  - Total spin time 30 min at 3500 rpm (3500g/RC-3B), in 7.5 minute increments.
  - Carefully rinse the filter every 7.5 minutes to avoid aggregate formation.
  - Concentrate to a final volume of 500 µl and fully rinse the filter with the sample.
  - Do not just pool the central 2 fractions as this results in a lower scruin yield. Pooling 9-12 gives a high concentration of aggregates, but also a higher peak concentration.
- Transfer sample to the FPLC syringe and inject into the FPLC.
- Select the program "Scruin S12" and run at 0.5 ml/min, empty loop volume of 500 µl. Should take around 1 hour.
- Pump wash with H_2O-NaN_3.
- Check the peak fraction (#20) concentration using a full bradford, should be 1300-1500 mAU for around 2 mg/ml. Scruin extinction coefficient 13.7.

B.1.5 Purification of True and False Discharge

True Discharge

- Collect 3 ml of sperm from horseshoe crabs; keep on ice (30 minutes).
- Wash for high purity/low yield
  - Prepare 30 ml of (1x ASW): 12 ml (2.5× ASW), 18 ml H_2O. Check pH.
  - Wash sperm 2×. Suspend in 15 ml (asw). Spin for 10 min at 1800 rpm (750g/6R). Discard supernatant, keep pellet.
- Prepare 30 ml of (0.5× ASW, 25 mM $CaCl_2$): 150 µl 5M $CaCl_2$, 6 ml 2.5× ASW, H_2O, Pepstatin-A powder, 15 µl Leupeptin, 30 µl Aprotinin, 30 µl PMSF. Check pH.

- Resuspend pellet in (asw-cacl) to trigger TD. GENTLY.
- Incubate 30 min at 4°C.
- Shear 4× with a 21G2 syringe. Aim syringe at side of beaker to prevent frothing.
- No DNase needed for TD but incubate an extra 30 min to keep up with FD prep.
- Spin 10 min at 3250 rpm (24e2g/BC-6R). Keep supernatant. Keep pellet.
    - Prepare 15 ml of (0.5× ASW, 25 mM $CaCl_2$): 75 µl 5 M $CaCl_2$, 3 ml 2.5× ASW, H_2O, Pepstatin-A powder, 7.5 µl Leupeptin, 15 µl Aprotinin, 15 µl PMSF. Check pH.
- Resuspend pellet in 15 ml of (asw-nacl). GENTLY!
- Spin 10 min at 3250 rpm. Keep supernatant, discard pellet.
- Spin all the supernatant for 10 min at 3250 rpm (24e2g/BC-6R). Keep supernatant, discard pellet.
- Spin all the supernatant for 20 min at 20,000 rpm (48e3g/SS34). Keep pellet, discard supernatant.
    - Prepare 20 ml of (1× a-buffer, 0.5 mM DTT): 2 ml 10× a-buffer, 10 µl of 1 M DTT, H_2O. Check pH.
    - Prepare 7.5 ml of (1× a-buffer, 0.5 mM DTT, 38 mM hecameg): 7.5 ml 1× a-buffer, 0.096 g hecameg. Filter.
- Resuspend pellet in (abuff-dtt-heca).
- Incubate 30 min at 4°C.
- Spin all the supernatant for 20 min at 20,000 rpm (48e3g/SS34). Keep pellet, discard supernatant.
- Resuspend in 1 ml of (abuff-dtt).
- Spin 4× 5 min at 11,000 rpm (1e4g/desktop) to remove all hecameg.
- Determine concentration with Bradford assay.

False Discharge

- Collect 3 ml of sperm from horseshoe crabs; keep on ice (30 minutes).
- Wash for high purity/low yield
    - Prepare 30 ml of (1x ASW): 12 ml (2.5× ASW), 18 ml H_2O. Check pH.
    - Wash sperm 2×. Suspend in 15 ml (asw). Spin for 10 min at 1800 rpm (750g/6R). Discard supernatant, keep pellet.
- Prepare 30 ml of (0.5× ASW, 0.6 M NaCl): 4.5 ml 4 M NaCl, 6 ml 2.5× ASW, H_2O, Pepstatin-A powder, 15 µl Leupeptin, 30 µl Aprotinin, 30 µl PMSF. Check pH.
- Resuspend pellet in (asw-nacl) to trigger FD. GENTLY!
- Incubate 30 min at 4°C.

- Shear 4× with a 21G2 syringe. Aim syringe at side of beaker to prevent frothing. Will become highly viscous.
- Add 1 mm^3 (0.1 mg/ml) of DNase powder (-20C/641)
- Incubate 30 min at 20°C.
- Spin 10 min at 3250 rpm (24e2g/BC-6R). Keep supernatant. Keep pellet.
    - Prepare 15 ml of (0.5× ASW, 0.6 M NaCl): 2.25 ml 4 M NaCl, 3 ml 2.5× ASW, H_2O, Pepstatin-A powder, 7.5 µl Leupeptin, 15 µl Aprotinin, 15 µl PMSF. Check pH.
- Resuspend pellet in 15 ml of (asw-nacl). GENTLY.
- Spin 10 min at 3250 rpm. Keep supernatant, discard pellet.
- Spin all the supernatant for 10 min at 3250 rpm (24e2g/BC-6R). Keep supernatant, discard pellet.
- Spin all the supernatant for 20 min at 20,000 rpm (48e3g/SS34). Keep pellet, discard supernatant.
    - Prepare 20 ml of (1× a-buffer, 0.5 mM DTT): 2 ml 10× a-buffer, 10 µl of 1 M DTT, H_2O. Check pH.
    - Prepare 7.5 ml of (1× a-buffer, 0.5 mM DTT, 38 mM hecameg): 7.5 ml 1× a-buffer, 0.096 g hecameg. Filter.
- Resuspend pellet in (abuff-dtt-heca).
- Incubate 30 min at 4°C.
- Spin all the supernatant for 20 min at 20,000 rpm (48e3g/SS34). Keep pellet, discard supernatant.
- Resuspend in 1 ml of (abuff-dtt).
- Spin 4x5 min at 11,000 rpm (1e4g/desktop) to remove all hecameg.
- Determine concentration with Bradford assay.

B.2 Experimental Protocols

B.2.1 Stocks and Buffers

- a-buffer
    - 1× a-buffer: 10 mM Tris pH 8, 1 mM $CaCl_2$, 100 mM NaCl, 3 mM NaN_3, 0.5 mM DTT.
    - 1 L of 10× a-buffer no DTT: 58.4 g NaCl (or 250 ml 4 M stock = 1 M NaCl), (12.7 g Tris-HCl, 2.36 g Trizma Base = 100 mM Tris), 10 ml 1 M $CaCl_2$, 10 ml 3M NaN_3.
    - Add 5 µl of 1 M DTT to 10 ml of 1× a-buffer for 0.5 mM DTT.
- g-buffer

  - 1× g-buffer: 5 mM Tris pH 8, 0.2 mM ATP, 0.2 mM $CaCl_2$, 0.5 mM DTT, 0.1 mM NaN_3.
  - 1 L of 10× g-buffer no ATP/DTT: (6.35 g Tris-HCl + 1.18g Trizma Base = 50 mM Tris), 2 ml of 1 M $CaCl_2$, 0.33 ml 3M NaN_3, H_2O.
  - Add 2 µl of 1 M ATP + 5 µl of 1 M DTT to 10 ml of 1× g-buffer for 0.2 mM ATP and 0.5 mM DTT.

- f-buffer
  - 10× f-buffer: 20 mM $MgCl_2$, 500 mM KCl, 0.2 mM ATP, 0.5 mM DTT.
  - 10 ml of 10× f-buffer: 200 µl 1 M $MgCl_2$, 5 ml 1 M KCl, 4.8 ml H_2O.
  - 10 ml of 10× f-buffer-egta: 10 ml 10× f-buffer, 50 µl 1 M DTT, 100 µl 1 M EGTA (for 10 mM), 20 µl 1 M ATP.
  - 10 ml of 10× f-buffer-ca: 10 ml 10× f-buffer, 50 µl 1 M DTT, 20 µl 1 M $CaCl_2$ (for 2 mM), 20 µl 1 M ATP.
  - Add 2 µl of 1 M ATP + 5 µl of 1 M DTT to 1 ml of 10× f-buffer for 2 mM ATP and 5 mM DTT.

- p-buffer
  - 1× p-buffer: 10 mM Pipes pH 7.8, 3 mM NaN_3, 0.1 mM EGTA, 100 mM NaCl
  - 1 L of 10× p-buffer: 10 ml 3 M NaN_3, 58.4 g NaCl (or 250 ml 4 M stock = 1 M NaCl), 30.2 g Pipes, 3.8 g EGTA; adjust to pH 7.8 at 4°C (takes a lot of NaOH, at least 1 small squeeze bottle, keep adding until solution becomes clear).

- ASW
  - 1× ASW: 10 mM Tris pH 8, 423 mM NaCl, 9 mM KCl, 9.27 mM $CaCl_2$, 22.94 mM $MgCl_2$, 25.5 mM $MgSO_4$, 2.15 mM $NaHCO_3$.
  - 1 L of 2× ASW: 49.4 g NaCl, 1.34 g KCl, 3.2 g $CaCl_2$, 9.3 g $MgCl_2$, 6.1 g $MgSO_4$, 0.36 g $NaHCO_3$ (sodium bicarbonate or sodium hydrogen carbonate), (2.5 g Tris-HCl, 0.47 g Trizma Base = 20 mM Tris).

- ATP
  - 10 ml of 1 M ATP: 5.51 g ATP (MW 551.14), 10 ml H_2O. Adjust to pH 8 at 4°C, store as 100 µl aliquots at -20°C.

- DTT
  - 10 ml of 1 M DTT: 1.54 g DTT (MW 154.25), 10 ml H_2O. Adjust to pH 8 at 4°C, store as 250 µl aliquots at -20°C.
  - Half life in solution is around 10 hours at pH 7.5 (so discard aliquots at end of day). It will reduce SH_2 bonds and prevent disulfide bond formation (and therefore aggregation) in monomers. It will also break any disulfide bonds that may have formed.

- Inhibitors
  - 1:1000 PMSF/Benzamidine stock (20C). Shelf.

    - $*$ 10 ml of 0.29 M PMSF, 0.63 M Benzamidine in EtOH: 0.5 g PMSF (Phenyl-MethylSulfonylFluoride MW 174.2), 0.75 g Benzamidine (Benzamidine HCl Monohydrate, MW 174.65), 10 ml 100% (200 proof) EtOH.
  - Pepstatin A powder
  - 1:2000 Leupeptin (-20°C): 10 mg/ml in MetOH. Freezer.
  - 1:1000 Aprotinin (4°C): 1000 KIU/ml. Fridge.
  - 1:1000 E-64 (-20°C): 10 mg/ml in water. Freezer.

- Additional Stocks
  - 10 mg/ml casein in 1× a-buffer (Fluka).
  - 66 μM (10×) Alexa-Fluor 488 phalloidin in MetOH (Invitrogen).
  - 10% (100 mg/ml) dextran in H_2O (MW = 410 kD or 670 kD, Fluka).
  - 10% (100 mg/ml) dextran sulfate in H_2O (MW 500 kD, Sigma).

B.2.2 Imaging Protocols

Actin Polymerization

Prepare 10 μl of 1 μM f-actin. (At 1 μM, actin will polymerize at a rate of 2 μm/min.)

- 1 μl of 10 μM g-actin (1 μM final) + 7.85 μl of 1× g-buffer + 1 μl of 10× f-buffer (1× final) + 0.15 μl of 66 μM phalloidin (1 μM, 1:1 final).

Flowcell Construction

- Use cleaned slides and coverslips (see below).
- Place 2 rows of double sided tape (nominally 100 μm thick) on slide to create a channel 2 mm wide. The volume will be 5-10 μl.
- Pipette solution into one end of flowcell, capillary action will draw the liquid through the channel.
- Use #1 filter paper to draw additional solution through the channel.
- Seal ends with nail polish to reduce drying.

Actin Persistence Length Imaging

- Dilute 1 μM phalloidin f-actin to 100 μl, 5 nM.
  - 0.5 μl of 1 μM f-actin (5 nM final) + 67.5 μl of 1× g-buffer + 10 μl of 10× f-buffer (1× final) + 20 μl of 10% dextran (2% final) + 5 μl of 400 mM DL-lactic acid (20 mM final) + 2 μl of OxyFluor (1 : 50 final).
- Construct flowcell as above.
- Block flowcell with 15 μl of 10 mg/ml casein (MW19-25kD, radius 2.1-2.4 nm) in 1× a-buffer. Incubate 5-30 minutes.
- Prepare 15 μl of 1× g-buffer/f-buffer: 13.5 μl of 1× g-buffer + 1.5 μl of 10× f-buffer.
- Flush flowcell with 1× g-buffer/f-buffer to remove excess casein.
- Pipette in actin solution and seal ends with nail polish.

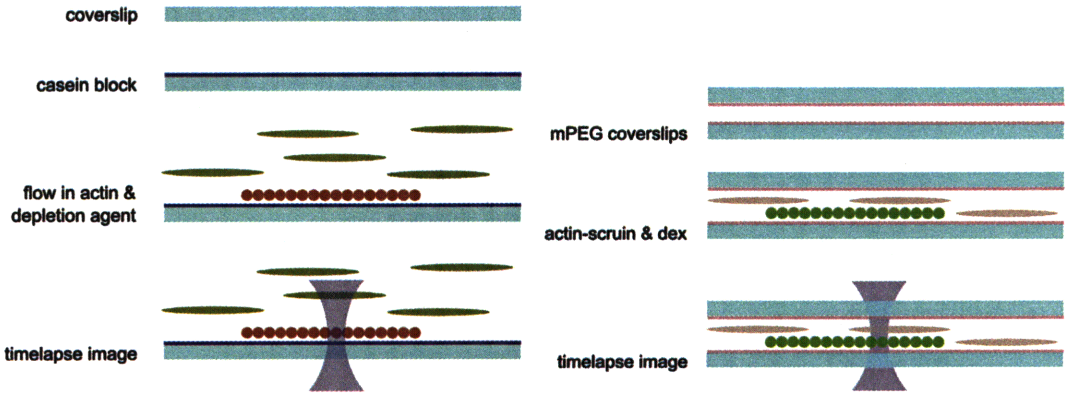

Figure B-2: Flowcells for persistence length imaging of actin (left) and scruin decorated actin filaments (right).

- Image directly.

Actin Scruin Persistence Length Imaging

- Dilute 1 µM phalloidin f-actin to 44 nM and incubate with 2 µM scruin for 30 minutes.
  - 1.5 µl of 1 µM f-actin (44 nM final) + 27.5 µl of 1× a-buffer + 5 µl of 14 µM scruin (2 µM final).
- Add dextran to slow filaments, OxyFluor to reduce bleaching and casein to reduce sticking.
  - 10 µl of 10% dextran (2% final) + 2.5 µl of 400 mM DL-lactic acid (20 mM final) + 1 µl of OxyFluor (1 : 50 final) + 2.5 µl of 10 mg/ml casein in 1× a-buffer (0.5 mg/ml final).
- Sandwich 2 µl f-actin scruin filaments between two 22x40 mm PEG coated coverslips and image immediately.

Seed Sonication

- Use seeds (TD or FD) within 2-3 weeks or they start to disintegrate.
- Take 200 µl of TD or FD + 1300 µl 1× a-buffer.
- Sonicate at setting #1 (3W) for 30-60 seconds (Misonix). This will produce seeds 750 nm long with average diameter of 108 nm.
- Remove solution and avoid the "fluffy" destroyed seed that typically occurs during heavier sonication.
- Spin for 5 minutes at 16e3g (14,000 rpm) in a desktop centrifuge to pellet the sonicated seeds.
- Resuspend in 1500 ml of 1× a-buffer.
- Measure concentration with a Bradford assay. Should be around 1-2 µM.

Kinetics Imaging

- Construct flowcell (Figure B-3). Use BioBond coverslip and cleaned slide.

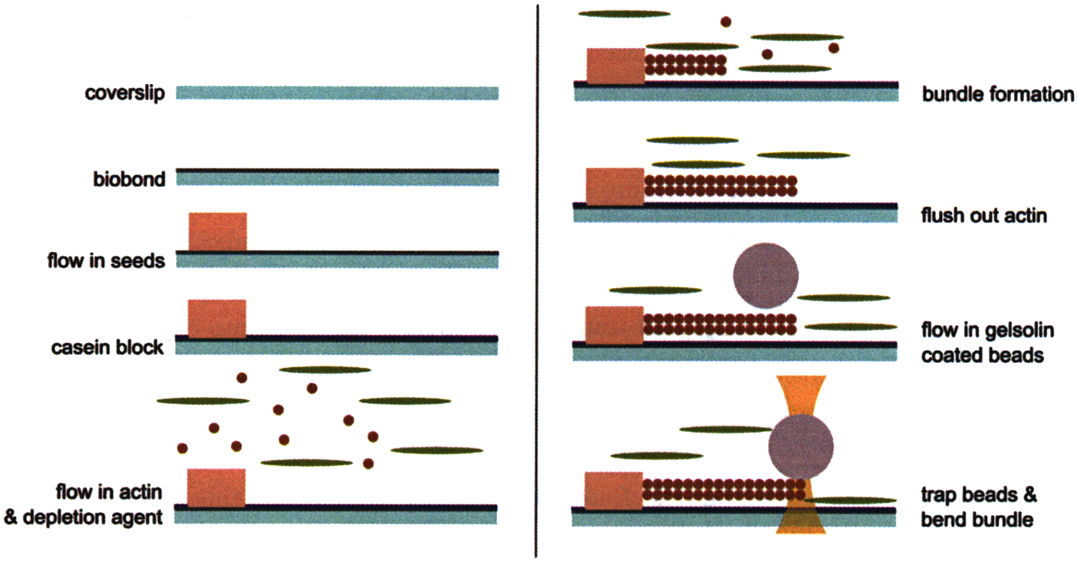

Figure B-3: Formation of seeded actin bundles with a depletion agent in a flowcell.

- Pipette in 30 nM sonicated seed (TD or FD) from above. Incubate 5min to stick seeds to coverslip.
- Focus on a suitable region of the coverslip and be careful not to bump the stage.
- Block flowcell with 15 µl of 10 mg/ml casein in 1× a-buffer. Incubate 5 minutes.
- Flush out excess seeds and casein with 15 µl of 1× a-buffer.
- Prepare 10 µl of 1 µM actin mixture:
  - 1 µl of 10 µM g-actin (1 µM final) + 5.85 µl of 1× g-buffer + 2 µl of 10% dextran (or dextran sulfate, 2% final) + 1 µl of 10× f-buffer = 1× + 0.15 µl of 66 µM phalloidin (1 µM, 1:1 final, optional)
- Start imaging, bundle formation should begin after a brief lag period.
- Stop polymerization by flushing with 15 µl of 1× g-buffer/f-buffer (or 15 µl of 1× a-buffer), each with 2% dextran sulfate to maintain bundle crosslinking.
- Note that reducing the concentration of g-actin in solution below the critical concentration (150 nM) in the absence of phalloidin will lead to depolymerization.
- For actin scruin bundles substitute 2 µM scruin for 2% dextran sulfate.

Gelsolin Bead Binding Assay

Polymerize actin in the presence of gelsolin beads.

- 1 µl 10 µM g-actin + 0.5 µl 1:1 gelsolin beads + 0.15 µl 66 µM phalloidin + 1 µl 10× f-buffer + 7.35 µl 1× g-buffer.
- Incubate overnight at 4°C.

Prepare flowcell

- 3 µl 1 µM actin gelsolin + 31 µl 1× a-buffer + 2.5 µl 400 mM DL-lactic acid + 1 µl OxyFluor + 2.5 µl 10 mg/ml casein in 1× a-buffer + 10 µl 410 kD dextran in H_2O.
- Sandwich 2 µl between two 22x40 mm coverslips and image directly.

Optical Trap Bending

- Follow kinetics imaging procedure above.
- Flow in 10 µl of 1:25 gelsolin beads in 1× a-buffer (scruin bundles) or 1× a-buffer with 2% dextran sulfate (dextran sulfate bundles) and seal the flowcell.
- Find a free bead in the optical trap and manipulate the bead into contact with the bundle end.
- Run tether-pull script to bend bundle and compute force-displacement curve. Image bundle during bending for shape analysis.
- Determine length from images. Determine bending rigidity by fitting the beam bending cubic to the bundle skeletons.

Coverslip/Slide Cleaning with Hellmanex

- Wash coverslips/slides in 2% Hellmanex detergent in MilliQ H_2O.
- Rinse with MilliQ H_2O. Wick off excess water on a KimWipe.
- Rinse with 95% EtOH and air dry.

BioBond Surface Treatment

- 0.5 ml BioBond in 25 ml acetone (2% final).
- Clean coverslips as above.
- Soak coverslip for 5 min in BioBond-acetone mix. Wick off excess liquid on a KimWipe.
- Soak coverslip for 5 min in MilliQ H_2O. Wick off excess liquid on a KimWipe.
- Air dry. Use within 1-2 days.

B.2.3 Coverslip Etching by KOH

This protocol cleans coverslips by etching them in KOH. Protocol from Polly Fordyce and Matt Lang (Lang Lab, MIT).

- Materials: 100 g KOH, Ethanol (Brown Bottle)
- Dissolve 100g of KOH in 300 ml of brown bottle ethanol in a beaker. Stir with a stir bar until KOH is completely dissolved.
- Put coverslips in Teflon racks.
- Fill one beaker with 300 ml of brown bottle ethanol, and two more beakers with 300ml of MilliQ. Degas all four beakers (the KOH in ethanol, the ethanol, and the two beakers with water) for 5 minutes in the bath sonicator on the degas setting.
- Submerge the rack of coverslips in the beaker with the KOH, and sonicate for 5 minutes.

- Dip the rack of coverslips up and down in a beaker of with ethanol until the water runs off the coverslips smoothly (no beading).
- Dip the rack of coverslips up and down in a beaker of water until the water runs off the coverslips smoothly (no beading).
- Submerge the rack of coverslips in the other beaker of water and sonicate for 5 minutes.
- Spritz with water until the water flows off the coverslips smoothly. Spritz each side twice, and use about half of a squirt bottle for each rack of coverslips.
- Spritz with ethanol until the ethanol flows off the coverslips smoothly.
- Dry the rack in the oven for at least 15 minutes.

B.2.4 Coverslip Functionalization by Polyethylene Glycol

Polyethylene Glycol (PEG) is typically regarded as the gold standard in preventing non-specific binding. This protocol describes a two-step procedure for covalently coating etched coverslips with PEG. The first step coats etched coverslips with aminosilane and the second step attaches the PEG molecules to the primary amines in the silane. Protocol from Ricardo Brau and Yongdae Shin (Lang Lab, MIT).

- Buffers/reagents:
  - 100 mM Sodium Bicarbonate pH 8.7, make fresh and filter. 10 ml of 100 mM $NaHCO_3$: 84 mg $NaHCO_3$, 10ml H_2O, 7 µl 5 M KOH for pH 8.7.
  - (3-aminopropyl)triethoxysilane (A3648, Sigma) on lab bench.
  - mPEG-SVA, MW 5000 Da (MPEG-SVA-5000-1g, Laysan Bio), in -20°C freezer.
  - Biotin-PEG-NHS, MW 3400 Da (0H4M0F02, Nektar), in -20°C freezer.
- Take the mPEG and biotin-PEG jars and place it on the bench top.
  - It is important to let them equilibrate to room temperature before use because they are very moisture sensitive.
- Use KOH etched coverslips (see below).
- Expose coverslips to plasma discharge
  - Use plasma etcher on the 3rd floor.
  - Place coverslips on colored holders and into the machine.
  - Close the door, close bleed valve, turn the pump on and pump down for 90 seconds.
  - Turn power on, toggle knob to low and wait 15 seconds. If there is no glow, toggle off then back to low until a faint glow appears in the back of the chamber.
  - Turn knob to high, bleed valve and adjust for maximum plasma intensity.
  - Etch for 3.5 minutes, adjust bleed valve to maintain maximum plasma intensity.
  - Turn knob to off, pump switch off, power switch off, open bleed valve quickly to bring the chamber to atmosphere.

  - Put each coverslip into the holder with the plasma etched sides facing the tape side of the holder.

- Transfer coverslips to aminosilane holders.
- Submerge coverslips in 300 ml pure acetone and incubate for 10 minutes.
  - While incubating, mix 300 ml of acetone with 6 ml of aminosilane to make a 2% solution. Mix the solution (with a glass rod, or just swirl) until the turbidity disappears.
- Transfer coverslips to 2% aminosilane solution and incubate for 20 minutes at room temperature to allow the (3-aminopropyl)triethoxysilane to functionalize the coverslip surface.
  - Mid way through, sonicate for 2 minutes in a bath sonicator.
- Submerge coverslips in MilliQ, and gently dip/swish for about 30 seconds to remove excess silanizer.
- Transfer to a second MilliQ beaker and rinse again to remove all traces of silanizer.
- Individually dry each coverslip in compressed air.
- For 15% mPEG:
  - Dissolve 96 mg of the mPEG in 640 µl of fresh sodium bicarbonate (15mg mPEG per 100 µl of sodium bicarbonate). This is enough for 8 pairs of coverslips (16 coverslips in total).
  - -or- 48 mg mPEG in 320 µl sodium bicarbonate for 4 pairs of coverslips.
- For 12.5% mPEG, 0.125% biotin-PEG:
  - Dissolve 80 mg of the mPEG in 640 µl of fresh sodium bicarbonate (12.5 mg mPEG per 100 µl of sodium bicarbonate).
  - Dissolve 5 mg of biotin-PEG in 40 µl of fresh sodium bicarbonate.
  - Add 6.4 µl of the biotin-PEG solution to 640 µl of mPEG solution (1 µl biotin-PEG per 100 µl mPEG) to make 0.125% biotin-PEG, 12.5% mPEG.
- Centrifuge at 7200 rpm for 1 minute to remove bubbles.
- Fill the PEG bottles with argon gas before closing to avoid moisture.
- Sandwich 80 µl of the PEG between two 22x40 coverslips and incubate 3 hours at 22°C. Make 8 pairs of coverslips (16 coverslips in total).
- Gently rinse away excess polymer with MilliQ. Dry with compressed air and store in a dark dessicator under vacuum.

Bibliography

[1] University of Delaware Sea Grant College Program, 2008.

[2] R. Adami, O. Cintio, G. Trombetta, D. Choquet, and E. Grazi. On the stiffness of the natural actin filament decorated with alexa fluor tropomyosin. *Biophys Chem*, 104(2):469–476, 2003.

[3] U. Aebi, P. R. Smith, G. Isenberg, and T. D. Pollard. Structure of crystalline actin sheets. *Nature*, 288(5788):296–298, Nov. 1980.

[4] U. Aebi, W. Fowler, G. Isenberg, T. Pollard, and P. Smith. Crystalline actin sheets: their structure and polymorphism. *J Cell Biol*, 91(2):340–351, 1981.

[5] J. Andre. A propos d'une lecon sur la limule. *Ann. Fac. Sci. Clermont*, 26:27–38, 1965.

[6] D. C. Appleyard, K. Y. Vandermeulen, H. Lee, and M. J. Lang. Optical trapping for undergraduates. *Am J Phys*, 75(1):5–14, 2007.

[7] S. Asakura and F. Oosawa. On interaction between two bodies immersed in a solution of macromolecules. *J Chem Phys*, 22(7):1255–1256, 1954.

[8] J. R. Bartles. Parallel actin bundles and their multiple actin-bundling proteins. *Curr Opin Cell Biol*, 12(1):72–78, Feb. 2000.

[9] M. Bathe, C. Heussinger, M. M. A. E. Claessens, A. R. Bausch, and E. Frey. Cytoskeletal bundle mechanics. *Biophys J*, 94(8):2955–2964, 2008.

[10] D. ben Avraham and M. Tirion. Dynamic and elastic properties of f-actin: a normal-modes analysis. *Biophys J*, 68(4):1231–1245, 1995.

[11] I. Borukhov, R. F. Bruinsma, W. M. Gelbart, and A. J. Liu. Structural polymorphism of the cytoskeleton: A model of linker-assisted filament aggregation. *Proc Natl Acad Sci*, 102(10):3673–3678, 2005.

[12] M. M. Bradford. A rapid and sensitive method for the quantitation of microgram quantities of protein utilizing the principle of protein-dye binding. *Anal Biochem*, 72 (1-2):248–254, May 1976.

[13] C. P. Brangwynne, G. H. Koenderink, E. Barry, Z. Dogic, F. C. MacKintosh, and D. A. Weitz. Bending dynamics of fluctuating biopolymers probed by automated high-resolution filament tracking. *Biophys J*, 93(1):346–359, 2007.

[14] A. Bremer, R. Millonig, R. Sutterlin, A. Engel, T. Pollard, and U. Aebi. The structural basis for the intrinsic disorder of the actin filament: the "lateral slipping" model. *J Cell Biol*, 115(3):689–703, Nov. 1991.

[15] G. Brown. Scanning electron-microscopical and other observations of sperm fertilization reactions in *Limulus Polyphemus* L. (Merostomata: Xiphosura). *J Cell Sci*, 22 (3):547–562, Dec. 1976.

[16] G. G. Brown and W. J. Humphreys. Sperm-egg interactions of *Limulus Polyphemus* with scanning electron microscopy. *J Cell Biol*, 51(3):904–907, Dec. 1971.

[17] E. Bullitt, D. DeRosier, L. Coluccio, and L. Tilney. Three-dimensional reconstruction of an actin bundle. *J Cell Biol*, 107(2):597–611, Aug. 1988.

[18] M. Capitanio, M. Canepari, P. Cacciafesta, V. Lombardi, R. Cicchi, M. Maffei, F. S. Pavone, and R. Bottinelli. Two independent mechanical events in the interaction cycle of skeletal muscle myosin with actin. *Proc Natl Acad Sci*, 103(1):87–92, Jan. 2006.

[19] M. Carlier. Actin: protein structure and filament dynamics. *J Biol Chem*, 266(1): 1–4, Jan. 1991.

[20] M. Carlier, D. Pantaloni, and E. Korn. The effects of Mg^{2+} at the high-affinity and low-affinity sites on the polymerization of actin and associated ATP hydrolysis. *J Biol Chem*, 261(23):10785–10792, Aug. 1986.

[21] M. Carlier, D. Pantaloni, and E. Korn. Fluorescence measurements of the binding of cations to high-affinity and low-affinity sites on ATP-G-actin. *J Biol Chem*, 261(23): 10778–10784, Aug. 1986.

[22] M. Carlier, D. Pantaloni, and E. Korn. The mechanisms of ATP hydrolysis accompanying the polymerization of Mg-actin and Ca-actin. *J Biol Chem*, 262(7):3052–3059, Mar. 1987.

[23] J.-W. Chu and G. A. Voth. Allostery of actin filaments: Molecular dynamics simulations and coarse-grained analysis. *Proc Natl Acad Sci*, 102(37):13111–13116, 2005.

[24] J.-W. Chu and G. A. Voth. Coarse-grained modeling of the actin filament derived from atomistic-scale simulations. *Biophys J*, 90(5):1572–1582, Mar. 2006.

[25] M. M. A. E. Claessens, M. Bathe, E. Frey, and A. R. Bausch. Actin-binding proteins sensitively mediate f-actin bundle stiffness. *Nat Mater*, 5(9):748–753, Sept. 2006. ISSN 1476-1122.

[26] M. M. A. E. Claessens, C. Semmrich, L. Ramos, and A. R. Bausch. Helical twist controls the thickness of f-actin bundles. *Proc Natl Acad Sci*, 105(26):8819–8822, July 2008.

[27] A. E. Cohen and L. Mahadevan. Kinks, rings, and rackets in filamentous structures. *Proc Natl Acad Sci*, 100(21):12141–12146, 2003.

[28] Y. Cong, M. Topf, A. Sali, P. Matsudaira, M. Dougherty, W. Chiu, and M. F. Schmid. Crystallographic conformers of actin in a biologically active bundle of filaments. *J Mol Biol*, 375(2):331–336, Jan. 2008.

[29] E. M. De La Cruz and T. D. Pollard. Transient kinetic analysis of rhodamine phalloidin binding to actin filaments. *Biochemistry*, 33(48):14387–14392, Dec. 1994. ISSN 0006-2960.

[30] E. M. De La Cruz, A. Mandinova, M. O. Steinmetz, D. Stoffler, U. Aebi, and T. D. Pollard. Polymerization and structure of nucleotide-free actin filaments. *J Mol Biol*, 295(3):517–526, 2000.

[31] D. DeRosier, L. Tilney, and P. Flicker. A change in the twist of the actin-containing filaments occurs during the extension of the acrosomal process in *Limulus* sperm. *J Mol Biol*, 137(4):375–389, Mar. 1980.

[32] D. J. DeRosier and L. G. Tilney. How to build a bend into an actin bundle. *J Mol Biol*, 175(1):57–73, May 1984.

[33] D. J. DeRosier, L. G. Tilney, E. M. Bonder, and P. Frankl. A Change in Twist of Actin Provides the Force for the Extension of the Acrosomal Process in *Limulus* Sperm: the False-discharge Reaction. *J Cell Biol*, 93(2):324–337, May 1982.

[34] Z. Dogic, J. Zhang, A. W. C. Lau, H. Aranda-Espinoza, P. Dalhaimer, D. E. Discher, P. A. Janmey, R. D. Kamien, T. C. Lubensky, and A. G. Yodh. Elongation and fluctuations of semiflexible polymers in a nematic solvent. *Phys Rev Lett*, 92(12): 125503–4, Mar. 2004.

[35] C. G. Dos Remedios and M. J. Dickens. Actin microcrystals and tubes formed in the presence of gadolinium ions. *Nature*, 276(5689):731–733, Dec. 1978.

[36] C. G. Dos Remedios, D. Chhabra, M. Kekic, I. V. Dedova, M. Tsubakihara, D. A. Berry, and N. J. Nosworthy. Actin binding proteins: Regulation of cytoskeletal microfilaments. *Physiol Rev*, 83(2):433–473, Apr. 2003.

[37] D. Drenckhahn and T. Pollard. Elongation of actin filaments is a diffusion-limited reaction at the barbed end and is accelerated by inert macromolecules. *J Biol Chem*, 261(27):12754–12758, 1986.

[38] D. E. Dupuis, W. H. Guilford, J. Wu, and D. M. Warshaw. Actin filament mechanics in the laser trap. *J Muscle Res Cell Motil*, 18(1):17–30, 1997.

[39] E. H. Egelman. Acrosomal actin: Twists and turns of a versatile filament. *Curr Biol*, 14(22):R959–R961, Nov. 2004.

[40] J. E. Estes, L. A. Selden, and L. C. Gershman. Mechanism of action of phalloidin on the polymerization of muscle actin. *Biochemistry*, 20(4):708–712, Feb. 1981.

[41] J. M. Ferrer, H. Lee, J. Chen, B. Pelz, F. Nakamura, R. D. Kamm, and M. J. Lang. Measuring molecular rupture forces between single actin filaments and actin-binding proteins. *Proc Natl Acad Sci*, 105(27):9221–9226, July 2008.

[42] W. Fowler and U. Aebi. Polymorphism of actin paracrystals induced by polylysine. *J Cell Biol*, 93(2):452–458, 1982.

[43] I. Fujiwara, S. Takahashi, H. Tadakuma, T. Funatsu, and S. Ishiwata. Microscopic analysis of polymerization dynamics with individual actin filaments. *Nat Cell Biol*, 4:666–673, 2002.

[44] I. Fujiwara, D. Vavylonis, and T. D. Pollard. Polymerization kinetics of ADP- and ADP-Pi-actin determined by fluorescence microscopy. *Proc Natl Acad Sci*, 104(21): 8827–8832, May 2007.

[45] N. Fuller and R. P. Rand. Water in actin polymerization. *Biophys J*, 76(6):3261–3266, June 1999.

[46] M. L. Gardel, J. H. Shin, F. C. MacKintosh, L. Mahadevan, P. Matsudaira, and D. A. Weitz. Elastic behavior of cross-linked and bundled actin networks. *Science*, 304(5675):1301–1305, 2004.

[47] F. Gittes, B. Mickey, J. Nettleton, and J. Howard. Flexural rigidity of microtubules and actin filaments measured from thermal fluctuations in shape. *J Cell Biol*, 120(4): 923–934, Feb. 1993.

[48] J. Goverman, L. Schick, and J. Newman. The bundling of actin with polyethylene glycol 8000 in the presence and absence of gelsolin. *Biophys J*, 71(3):1485–1492, 1996.

[49] L. Haviv, N. Gov, Y. Ideses, and A. Bernheim-Groswasser. Thickness distribution of actin bundles in vitro. *Eur Biophys J*, 37(4):447–454, Apr. 2008.

[50] K. C. Holmes, D. Popp, W. Gebhard, and W. Kabsch. Atomic model of the actin filament. *Nature*, 347(6288):44–49, Sept. 1990.

[51] M. Hosek and J. X. Tang. Polymer-induced bundling of f-actin and the depletion force. *Phys Rev E*, 69(5):051907, 2004.

[52] H. Huxley, A. Stewart, H. Sosa, and T. Irving. X-ray diffraction measurements of the extensibility of actin and myosin filaments in contracting muscle. *Biophys J*, 67(6): 2411–2421, 1994.

[53] H. Isambert, P. Venier, A. Maggs, A. Fattoum, R. Kassab, D. Pantaloni, and M. Carlier. Flexibility of actin filaments derived from thermal fluctuations. Effect of bound nucleotide, phalloidin, and muscle regulatory proteins. *J Biol Chem*, 270(19):11437–11444, May 1995.

[54] P. A. Janmey, J. X. Tang, and C. F. Schmidt. Actin Filaments, 2004.

[55] W. Kabsch, H. G. Mannherz, D. Suck, E. F. Pai, and K. C. Holmes. Atomic structure of the actin:DNase I complex. *Nature*, 347(6288):37–44, Sept.6, 1990.

[56] J. Kas, H. Strey, and E. Sackmann. Direct imaging of reptation for semiflexible actin filaments. *Nature*, 368(6468):226–229, Mar. 1994.

[57] J. Kas, H. Strey, J. X. Tang, D. Finger, R. Ezzell, E. Sackmann, and P. A. Janmey. F-actin, a model polymer for semiflexible chains in dilute, semidilute, and liquid crystalline solutions. *Biophys J*, 70(2):609–625, Feb. 1996.

[58] A. S. Khalil, J. M. Ferrer, R. R. Brau, S. T. Kottmann, C. J. Noren, M. J. Lang, and A. M. Belcher. Single m13 bacteriophage tethering and stretching. *Proc Natl Acad Sci*, 104(12):4892–4897, Mar. 2007.

[59] H. Kojima, A. Ishijima, and T. Yanagida. Direct measurement of stiffness of single actin filaments with and without tropomyosin by *in vitro* nanomanipulation. *Proc Natl Acad Sci*, 91(26):12962–12966, 1994.

[60] E. D. Korn. Actin polymerization and its regulation by proteins from nonmuscle cells. *Physiol Rev*, 62(2):672–737, Apr. 1982.

[61] E. D. Korn, M.-F. Carlier, and D. Pantaloni. Actin polymerization and ATP hydrolysis. *Science*, 238(4827):638–644, Oct.30, 1987.

[62] S. Koster, D. Steinhauser, and T. Pfohl. Brownian motion of actin filaments in confining microchannels. *J Phys: Condens Matter*, 17(49):S4091, 2005.

[63] D. S. Kudryashov, M. R. Sawaya, H. Adisetiyo, T. Norcross, G. Hegyi, E. Reisler, and T. O. Yeates. The crystal structure of a cross-linked actin dimer suggests a detailed molecular interface in f-actin. *Proc Natl Acad Sci*, 102(37):13105–13110, 2005.

[64] J. R. Kuhn and T. D. Pollard. Real-time measurements of actin filament polymerization by total internal reflection fluorescence microscopy. *Biophys J*, 88(2):1387–1402, 2005.

[65] M. J. Lang and S. M. Block. Laser-based optical tweezers. *Am J Phys*, 71(3):201–215, Mar. 2003.

[66] G. Langford, S. Kuznetsov, D. Johnson, D. Cohen, and D. Weiss. Movement of axoplasmic organelles on actin filaments assembled on acrosomal processes: evidence for a barbed-end-directed organelle motor. *J Cell Sci*, 107(8):2291–2298, 1994.

[67] R. A. Lindner and G. B. Ralston. Macromolecular crowding: effects on actin polymerisation. *Biophys Chem*, 66(1):57–66, May 1997.

[68] P. Matsudaira. Modular organization of actin crosslinking proteins. *Trends Biochem Sci*, 16:87–92, 1991.

[69] P. Matsudaira, E. Mandelkow, W. Renner, L. K. Hesterberg, and K. Weber. Role of fimbrin and villin in determining the interfilament distances of actin bundles. *Nature*, 301(5897):209–214, Jan. 1983.

[70] B. R. McCullough, L. Blanchoin, J.-L. Martiel, and E. M. De La Cruz. Cofilin increases the bending flexibility of actin filaments: Implications for severing and cell mechanics. *J Mol Biol*, 381(3):550–558, Sept. 2008.

[71] J. P. Mills, M. Diez-Silva, D. J. Quinn, M. Dao, M. J. Lang, K. S. W. Tan, C. T. Lim, G. Milon, P. H. David, O. Mercereau-Puijalon, S. Bonnefoy, and S. Suresh. Effect of plasmodial RESA protein on deformability of human red blood cells harboring *Plasmodium falciparum*. *Proc Natl Acad Sci*, 104(22):9213–9217, May 2007.

[72] K. C. Neuman and S. M. Block. Optical trapping. *Rev Sci Instrum*, 75(9):2787–2809, Sept. 2004.

[73] T. Nishizaka, R. Seo, H. Tadakuma, J. Kinosita, Kazuhiko, and S. Ishiwata. Characterization of single actomyosin rigor bonds: Load dependence of lifetime and mechanical properties. *Biophys J*, 79(2):962–974, 2000.

[74] E. Nordmeier. Static and dynamic light-scattering solution behavior of pullulan and dextran in comparison. *J Phys Chem*, 97:5770–5785, 1993.

[75] E. J. O'Brien, P. M. Bennett, and J. Hanson. Optical diffraction studies of myofibrillar structure. *Philos Trans R Soc London, B*, 261(837):201–208, May 27 1971. ISSN 00804622.

[76] T. Oda, K. Namba, and Y. Maeda. Position and orientation of phalloidin in f-actin determined by x-ray fiber diffraction analysis. *Biophys J*, 88(4):2727–2736, 2005.

[77] A. Orlova and E. H. Egelman. A conformational change in the actin subunit can change the flexibility of the actin filament. *J Mol Biol*, 232(2):334–341, July 1993.

[78] A. Orlova and E. H. Egelman. F-actin retains a memory of angular order. *Biophys J*, 78(4):2180–2185, Apr. 2000.

[79] A. Ott, M. Magnasco, A. Simon, and A. Libchaber. Measurement of the persistence length of polymerized actin using fluorescence microscopy. *Phys Rev E*, 48(3):R1643–R1645, 1993.

[80] C. Owen and D. DeRosier. A 13-Å map of the Actin-Scruin Filament from the Limulus Acrosomal Process. *J Cell Biol*, 123(2):337–344, 1993.

[81] O. Pelletier, E. Pokidysheva, L. S. Hirst, N. Bouxsein, Y. Li, and C. R. Safinya. Structure of actin cross-linked with α-actinin: A network of bundles. *Phys Rev Lett*, 91(14):148102–, Sept. 2003.

[82] T. Pollard. Polymerization of ADP-actin. *J Cell Biol*, 99(3):769–777, 1984.

[83] T. Pollard. Rate constants for the reactions of ATP- and ADP-actin with the ends of actin filaments. *J Cell Biol*, 103(6):2747–2754, 1986.

[84] T. Pollard and M. Mooseker. Direct measurement of actin polymerization rate constants by electron microscopy of actin filaments nucleated by isolated microvillus cores. *J Cell Biol*, 88(3):654–659, 1981.

[85] D. Riveline, C. H. Wiggins, R. E. Goldstein, and A. Ott. Elastohydrodynamic study of actin filaments using fluorescence microscopy. *Phys Rev E*, 56(2):R1330–, Aug. 1997.

[86] M. C. Sanders, M. Way, J. Sakai, and P. Matsudaira. Characterization of the Actin Cross-linking Properties of the Scruin-Calmodulin Complex from the Acrosomal Process of *Limulus* Sperm. *J Biol Chem*, 271(5):2651–2657, Feb. 1996.

[87] M. F. Schmid, P. Matsudaira, T. W. Jeng, J. Jakana, E. Towns-Andrews, J. Bordas, and W. Chiu. Crystallographic analysis of acrosomal bundle from *Limulus* sperm. *J Mol Biol*, 221(2):711–725, Sept.20, 1991.

[88] M. F. Schmid, J. Jakana, P. Matsudaira, and W. Chiu. Effects of radiation damage with 400 kV electrons on frozen, hydrated actin bundles. *J Struct Biol*, 108(1):62–68, Jan. 1992.

[89] M. F. Schmid, J. Jakana, P. Matsudaira, and W. Chiu. Imaging Frozen, Hydrated Acrosomal Bundle from *Limulus* Sperm at 7 Å Resolution with a 400 kV Electron Cryomicroscope. *J Mol Biol*, 230(2):384–386, Mar.20, 1993.

[90] M. F. Schmid, J. M. Agris, J. Jakana, P. Matsudaira, and W. Chiu. Three-dimensional structure of a single filament in the *Limulus* acrosomal bundle: scruin binds to homologous helix-loop-beta motifs in actin. *J Cell Biol*, 124(3):341–350, Feb. 1994.

[91] M. F. Schmid, J. Jakana, W. Chiu, and P. Matsudaira. A 7-Å Projection Map of Frozen, Hydrated Acrosomal Bundle from *Limulus* Sperm. *J Struct Biol*, 115(2): 209–213, Sept. 1995.

[92] M. F. Schmid, M. B. Sherman, P. Matsudaira, and W. Chiu. Structure of the acrosomal bundle. *Nature*, 431(7004):104–107, 2004.

[93] M. B. Sherman, J. Jakana, S. Sun, P. Matsudaira, W. Chiuf, and M. F. Schmid. The Three-dimensional Structure of the *Limulus* Acrosomal Process: A Dynamic Actin Bundle. *J Mol Biol*, 294(1):139–149, Nov.19, 1999.

[94] J. H. Shin. Dynamics of an actin spring: The acrosomal process in the *Limulus polyphemus* sperm. Master's thesis, Massachusetts Institute of Technology, September 2000.

[95] J. H. Shin. *Dynamics of an actin spring.* PhD thesis, Massachusetts Institute of Technology, September 2003.

[96] J. H. Shin, L. Mahadevan, G. S. Waller, K. Langsetmo, and P. Matsudaira. Stored elastic energy powers the 60-μm extension of the *Limulus polyphemus* sperm actin bundle. *J Cell Biol*, 162(7):1183–1188, 2003.

[97] J. H. Shin, L. Mahadevan, P. T. So, and P. Matsudaira. Bending stiffness of a crystalline actin bundle. *J Mol Biol*, 337(2):255–261, 2004.

[98] J. H. Shin, B. K. Tam, R. R. Brau, M. J. Lang, L. Mahadevan, and P. Matsudaira. Force of an actin spring. *Biophys J*, 92(10):3729–3733, May 2007.

[99] J. A. Spudich and S. Watt. The regulation of rabbit skeletal muscle contraction. I. Biochemical studies of the interaction of the tropomyosin-troponin complex with actin and the proteolytic fragments of myosin. *J Biol Chem*, 246(15):4866–4871, 1971.

[100] D. Stokes and D. DeRosier. Growth conditions control the size and order of actin bundles in vitro. *Biophys J*, 59(2):456–465, 1991.

[101] H. Strzelecka-Golaszewska, E. Prochniewicz, and W. Drabikowski. Interaction of actin with divalent cations. 1. The effect of various cations on the physical state of actin. *Eur J Biochem*, 88(1):219–227, July 1978.

[102] S. Sun, M. Footer, and P. Matsudaira. Modification of cys-837 identifies an actin-binding site in the β-propeller protein scruin. *Mol Biol Cell*, 8(3):421–430, Mar.1, 1997.

[103] A. Suzuki, M. Yamazaki, and T. Ito. Osmoelastic coupling in biological structures: formation of parallel bundles of actin filaments in a crystalline-like structure caused by osmotic stress. *Biochemistry*, 28(15):6513–6518, 1989. ISSN 0006-2960.

[104] N. Suzuki, H. Miyata, S. Ishiwata, and J. Kinosita, K. Preparation of bead-tailed actin filaments: estimation of the torque produced by the sliding force in an in vitro motility assay. *Biophys J*, 70(1):401–408, Jan. 1996.

[105] B. K. Tam. *An Investigation of the Mechanics of an Actin Spring*. PhD thesis, Massachusetts Institute of Technology, September 2007.

[106] J. X. Tang and P. A. Janmey. The polyelectrolyte nature of f-actin and the mechanism of actin bundle formation. *J Biol Chem*, 271(15):8556–8563, 1996.

[107] K. A. Taylor, D. W. Taylor, and F. Schachat. Isoforms of α-actinin from cardiac, smooth, and skeletal muscle form polar arrays of actin filaments. *J Cell Biol*, 149(3): 635–646, May 2000.

[108] R. L. Tellam, M. J. Sculley, L. W. Nichol, and P. R. Wills. The influence of poly(ethylene glycol) 6000 on the properties of skeletal-muscle actin. *Biochem J*, 213(3):651–659, 1983.

[109] N. Terada, T. Shimozawa, S. Ishiwata, and T. Funatsu. Size distribution of linear and helical polymers in actin solution analyzed by photon counting histogram. *Biophys J*, 92(6):2162–2171, Mar. 2007.

[110] L. G. Tilney. Actin filaments in the acrosomal reaction of *Limulus* sperm. Motion generated by alterations in the packing of the filaments. *J Cell Biol*, 64(2):289–310, Feb. 1975.

[111] L. G. Tilney, J. G. Clain, and M. S. Tilney. Membrane events in the acrosomal reaction of *Limulus* sperm. Membrane fusion, filament-membrane particle attachment, and the source and formation of new membrane surface. *J Cell Biol*, 81(2):229–253, Apr. 1979.

[112] L. G. Tilney, E. M. Bonder, and D. J. DeRosier. Actin filaments elongate from their membrane-associated ends. *J Cell Biol*, 90(2):485–494, Aug. 1981.

[113] L. Tobacman and E. Korn. The kinetics of actin nucleation and polymerization. *J Biol Chem*, 258(5):3207–3214, Mar. 1983.

[114] M. Topf. Scruin structure (unpublished). 2008.

[115] Y. Tsuda, H. Yasutake, A. Ishijima, and T. Yanagida. Torsional rigidity of single actin filaments and actin-actin bond breaking force under torsion measured directly by *in vitro* micromanipulation. *Proc Natl Acad Sci*, 93(23):12937–12942, 1996.

[116] H. Tsuruta. Scruin radius of gyration from x-ray scattering (unpublished). 2008.

[117] C. Valentin-Ranc and M. Carlier. Role of ATP-bound divalent metal ion in the conformation and function of actin. Comparison of Mg-ATP, Ca-ATP, and metal ion-free ATP-actin. *J Biol Chem*, 266(12):7668–7675, Apr. 1991.

[118] N. Volkmann, D. DeRosier, P. Matsudaira, and D. Hanein. An atomic model of actin filaments cross-linked by fimbrin and its implications for bundle assembly and function. *J Cell Biol*, 153(5):947–956, 2001.

[119] M. Way, M. Sanders, C. Garcia, J. Sakai, and P. Matsudaira. Sequence and domain organization of scruin, an actin-cross-linking protein in the acrosomal process of *Limulus* sperm. *J Cell Biol*, 128(1):51–60, Jan. 1995.

[120] M. Way, M. C. Sanders, M. Chafel, Y. Tu, A. Knight, and P. Matsudaira. β-scruin, a homologue of the actin crosslinking protein scruin, is localized to the acrosomal vesicle of *Limulus* sperm. *J Cell Sci*, 108(10):3155–3162, Jan. 1995.

[121] J. Wolenski, R. Cheney, M. Mooseker, and P. Forscher. In vitro motility of immunoadsorbed brain myosin-V using a *Limulus* acrosomal process and optical tweezer-based assay. *J Cell Sci*, 108(4):1489–1496, 1995.

[122] G. C. L. Wong, A. Lin, J. X. Tang, Y. Li, P. A. Janmey, and C. R. Safinya. Lamellar phase of stacked two-dimensional rafts of actin filaments. *Phys Rev Lett*, 91(1):018103–1–4, July 2003.

[123] Y. Wu and J. Ma. Refinement of f-actin model against fiber diffraction data by long-range normal modes. *Biophys J*, 86(1):116–124, 2004.

[124] R. Yasuda, H. Miyata, and K. Kinosita, Jr. Direct Measurement of the Torsional Rigidity of Single Actin Filaments. *J Mol Biol*, 263(2):227–236, 1996.